

NON-DESTRUCTIVE TESTING TO MONITOR THE STRENGTH INCREASE OF ELECTROKINETICALLY TREATED SOIL

By

Colin Hunter

This thesis is submitted in partial fulfillment of the requirements
for the degree of Master of Science in Civil Engineering

Faculty of Graduate Studies
Lakehead University
Thunder Bay, Ontario, Canada
October 2018

© Colin Hunter 2018

Abstract

Electrokinetics in geotechnical engineering is used to increase the shear strength of soft soils and the load carrying capacity of piles embedded in these soils. This is achieved by decreasing the water content of the soil by electrokinetics, and often by inducing cementation. Practical issues such as determining the treatment effectiveness along with determining the appropriate treatment duration have limited its use in the field.

In this study, a steel pile foundation model was inserted in clayey soil that was treated with electrokinetics with bender elements embedded in the soil to monitor the shear wave velocity in the soil during the treatment. Changes in the shear-wave velocity were used as an indicator of changes in the structure and shear strength of the soil throughout treatment.

After the shear wave velocity ceased to increase, the gain in the strength of the soil by the treatment was considered to plateau and the treatment was terminated. Two weeks after treatment, the pile models were loaded. Shear vane tests were carried out to accurately define the zones of soil stiffened and the extent of the changes. To better comprehend the mechanisms which contributed to soil stiffening, by x-ray diffraction, x-ray energy dispersive spectrometry, Atterberg limits and pH tests were performed.

It was found in this study that by using bender elements to monitor the changes in the shear-wave velocity, the treatment time and total power consumed were reduced by more than 40 percent and 34 percent, respectively while achieving a similar reduction in water content and increase in shear strength to a test with seven days of treatment. The load carrying capacity after the treatment increased by 300 percent compared to the control.

Acknowledgements

I have been helped tremendously by many people throughout the last two-years, yet nothing has renewed my resolve much like the land around this great Lake Superior. All the times I had been at wits end I was renewed, so I thank this land for that.

I sincerely thank my supervisor Dr. Eltayeb Mohamedelhassan. When others may have been impatient, doubtful, or indifferent, you had faith in the work and in me. Thank you for this.

Thanks to my co-supervisor, Dr. Ayan Sadhu, for showing me the world of signal analysis and vibrations. Thank you for allowing me access to the DAQ and amplifier, without them this research would not be possible. Your critical review of my thesis helped me immensely.

Much of the equipment and materials were loaned or donated. The following persons have my sincere thanks for helping me acquire the equipment and skills that were instrumental in the research, and for supporting me as a person apart from my research.

Thank you, Ron Moore, for allowing me access to the soil and Coastal Steel Construction for providing the steel pile at such a discount.

Thank you, Jason Servais, for pointing me in the right direction when I knew so little about electronics.

The skills and experience of Conrad Hagstrom were very much appreciated. Thank you.

My sincere thanks go to Dr. Guosheng Wu for taking the time to explain the workings of the electron-microscope and being so personable. I greatly enjoyed hearing of life in China.

Without the help of Tom Collins there would have been many (more) endless nights. I wish I knew half of what you do about electronics. Your help has been invaluable in understanding embedded systems.

To my parents, thank you so much for your support in all the decisions I have made coming to this point. I hold this above all things you have given me.

Buddy Chan – Your antics were all I needed to keep a smile.

Michelle Chung, you fed me more times than I deserve in a kitchen too small, in a house too full, with a heart so big. Thank you for your infinite support and your ability to turn all bad days good.

Table of Contents

Abstract.....	i
Acknowledgements.....	ii
List of Figures	vii
List of Tables	xii
Thesis Outline.....	xiii
Chapter 1.....	1
1.1. Background	1
1.2. Electrokinetics.....	2
1.2.1. Mechanisms and Models of Electrokinetic Pore Fluid Flow	2
1.2.2. Physical and Chemical Factors affecting EK Process.....	4
1.2.3. Increasing the Load Capacity of Foundations	12
1.3. Bender elements.....	13
1.3.1. Bender Element Wiring.....	14
1.3.2. Bender Dimensions	15
1.3.3. Ideal Frequency.....	16
1.3.4. Wave-Form	17
1.4. Signal Analysis Techniques.....	17
1.4.1. Time Domain	17
1.4.2. Frequency Domain Technique	20
1.5. Shear Wave Velocity	21

1.5.1. Empirical Correlations of Shear Wave Velocity	22
1.6. Research Gaps.....	25
1.7. Objectives.....	25
Chapter 2 – Materials, Experimental Apparatus and Methodology	27
2.1. Soil Properties	27
2.2. Bender Elements.....	29
2.2.1. Housing	30
2.2.2. Construction Procedure	34
2.2.3. Installation in Soil.....	37
2.3. Preliminary Test System.....	40
2.4. Electrokinetic Treatment System.....	41
2.4.1. Barrel, Pile and Electrodes	41
2.4.2. Power Supply	42
2.4.3. DAQ and Power Control System	42
2.4.4. Wiring and Power Monitoring	43
2.5. Data Acquisition System	43
2.6. Pile Load Test	50
2.6.1. Loading System	50
2.6.2. Loading Procedure	52
2.7. Shear Vane Tests.....	52

2.8. X-Ray Diffraction Spectrometry	54
2.9. Scanning Electron Microscope and X-Ray Energy Dispersive Spectrometry	55
Chapter 3 – Results and Discussion	56
3.1. Electric Field and Power Consumption	56
3.2. Shear Wave Velocity	61
3.2.1. Barrel 1 – Shear Wave Velocity vs Time	62
3.2.2. Barrel 2 – Shear Wave Velocity vs Time	65
3.2.3. Barrel 3 – Shear Wave Velocity vs Time	66
3.2.4. Barrel 4 – Shear Wave Velocity vs Time	67
3.3. Shear Strength	71
3.4. Axial Load Capacity	83
3.5. X-Ray Diffraction Spectroscopy.....	85
3.6. Scanning Electron Microscope and X-Ray Energy Dispersive Spectrometry.....	85
3.6.1. Control	87
3.6.2. Barrel 1.....	88
3.6.3. Barrel 2.....	89
3.6.4. Barrel 3.....	90
3.6.5. Barrel 4.....	91
3.7. pH Tests.....	92
3.8. Atterberg Limits	94

3.9. Sources of Error/ Variability.....	95
Chapter 4 – Summary and Conclusion.....	98
4.1. Future Avenues of Research and Improvements	98
Bibliography	100
4.2. Appendix	109
4.2.1. Arduino Code	109
4.2.2. MATLAB Code	110

List of Figures

Figure 1.1: Anode of system after testing shows high level of corrosion [14].....	4
Figure 1.2: Electrophoretic Mobility vs pH of Three Clays [18].....	6
Figure 1.3: Electrophoretic Mobility vs pH of Milwhite Kaolinite in various Pore-Water Solutions [18].....	6
Figure 1.4: Electroosmotic Flow Rate across Treatment Time with Variations of Anolyte and Catholyte [20].....	7
Figure 1.5: Current Intensity during EK of Various Acids as Anolyte with active pH adjustment during period II [23].....	9
Figure 1.6: Power Consumption during EK of Various Acids as Anolyte with active pH adjustment during period II [23].....	9
Figure 1.7: Electro-osmotic flow during EK of Various Acids as Anolyte with active pH adjustment during period II [23].....	9
Figure 1.8: Cumulative Volume Discharged during EK Treatment with Distilled Water. [12]	11
Figure 1.9: Cumulative Volume Discharged during EK Treatment with Seawater [12].....	11
Figure 1.10: Diagram of Shear Wave response of Benders [36].....	18
Figure 1.11: Shear wave velocity of Ebetsu Organic Clay vs frequency of transmitted wave [35].....	21
Figure 1.12: Shear Wave Velocity vs Frequency dispersion curve from [29].....	24
Figure 2.1: Sandy Lean Clay - Grain Size Distribution.....	28
Figure 2.2: Schematic of Series Wired Bender Elements.....	30
Figure 2.3: Schematic of Parallel Wired Bender Elements.....	30
Figure 2.4: Schematic of Bender Element Housing.....	31
Figure 2.5: Section A-A of Bender Element Housing.....	32

Figure 2.6: Section B-B of Bender Element Housing.....	32
Figure 2.7: Schematic of Bender Elements with Alignment Rods	33
Figure 2.8: Bender Housing with Moat Cut	34
Figure 2.9: Bender Elements, Full Size and two halves	35
Figure 2.10: Bender Element with Steel Shim Exposed.....	35
Figure 2.11: A strong solder bond is made with the leads and the element	35
Figure 2.12: The Bender is Coated with Conformal Coating and Cured.....	36
Figure 2.13: Inner Core and Shielding Tinned.....	37
Figure 2.14: Bender Element shown before being housed (moat not cut yet).....	37
Figure 2.15: Bender Element nested in Housing (Moat Not Cut yet).....	37
Figure 2.16: Completely Assembled Bender Element with Epoxy Coating	37
Figure 2.17: Orientation of Benders next to Pile with Alignment Rods Inserted	38
Figure 2.18: Foundation Element, Electrodes and Bender Elements.....	39
Figure 2.19: Section View of Barrel with DAQ and DC power Supply	40
Figure 2.20: Power Supply and DAQ connected to Foundation System	40
Figure 2.21: Raw Shear Wave Received by DAQ	45
Figure 2.22: Baseline of Signal	45
Figure 2.23: Baseline overlying Original Signal	46
Figure 2.24: Signal Post-Baseline Removal	46
Figure 2.25: Signal Post-Smoothing and Baselining.....	46
Figure 2.26: Signal Post-Filter, Smoothing and Baselining	46
Figure 2.27: Post-Processed Signal with Three Peaks Selected for Wave Velocity Determination.....	47
Figure 2.28: Peak to Peak Shear Wave Velocity Determination.....	48

Figure 2.29: Cross-Correlation and Peak for Wave Velocity Determination	49
Figure 2.30: Output Signal Overlaid atop Received wave at CCF Delay	49
Figure 2.31: Barrel 3 with Loading rig above pile with wiring and conduit still in place.....	50
Figure 2.32: Pile Ready for Loading with Displacement and Strain Gages in place.....	51
Figure 2.33: ARTECH 20210-2k Load Cell.....	51
Figure 2.34: TRS-100 Position Transducer	51
Figure 2.35: Barrels with Loading Frame Above and Control Centre in Front	52
Figure 2.36: Schematic of Sample and Shear Vane Locations	53
Figure 2.37: Edeco Pilcon Shear Vane Hand Tester	54
Figure 2.38: Sample in XRD Spectroscope	54
Figure 3.1: Voltage potential of barrel undergoing treatment.....	57
Figure 3.2: Electric field strength of barrel undergoing treatment	58
Figure 3.3: Current density of barrel undergoing treatment	58
Figure 3.4: Amperage over Time under constant Voltage for all piles.....	60
Figure 3.5: Cumulative Power Consumption for all Treatments	60
Figure 3.6: Barrel 1 Shear Wave Velocity, 400Hz output, treated 170 Hours.....	63
Figure 3.7: Barrel 1 Shear Wave Velocity, 600Hz output, treated 170 Hours.....	63
Figure 3.8: Barrel 1 Shear Wave Velocity, 900Hz output, treated 170 Hours.....	64
Figure 3.9: Barrel 1 Shear Wave Velocity, 1500Hz output, treated 170 Hours.....	64
Figure 3.10: Barrel 1 Shear Wave Velocity, 2000Hz output, treated 170 Hours.....	65
Figure 3.11: Barrel 1 Shear Wave Velocity, 2500Hz output, treated 170 Hours.....	65
Figure 3.12: Barrel 2 Shear Wave Velocity, 600Hz output, no treatment.....	66
Figure 3.13: Barrel 3 Shear Wave Velocity, 600Hz output, no treatment.....	67
Figure 3.14: Barrel 4 Shear Wave Velocity, 400Hz output, 100 Hours Treatment.....	68

Figure 3.15: Barrel 4 Shear Wave Velocity, 600Hz output, 100 Hours Treatment.....	68
Figure 3.16: Barrel 4 Shear Wave Velocity, 900Hz output, 100 Hours Treatment.....	69
Figure 3.17: Barrel 4 Shear Wave Velocity, 1500Hz output, 100 Hours Treatment.....	69
Figure 3.18: Barrel 4 Shear Wave Velocity, 2000Hz output, 100 Hours Treatment.....	70
Figure 3.19: Barrel 4 Shear Wave Velocity, 2500Hz output, 100 Hours Treatment.....	70
Figure 3.20: Large Pit in Pile.....	71
Figure 3.21: Sample Taken Adjacent to Treated Pile.....	71
Figure 3.22: All Shear Vane Results for Barrel 3 – Control	73
Figure 3.23: All Shear Vane Results for Barrel 1	75
Figure 3.24: All Shear Vane Results for Barrel 2	77
Figure 3.25: All Shear Vanes for Barrel 3 – Treated.....	79
Figure 3.26: All Shear Vane Results for Barrel 4	81
Figure 3.27: Pile Load Capacity of All Piles	84
Figure 3.28: X-Ray Diffraction Results	85
Figure 3.29: SEM Image of Muscovite Sheets (Control, A2, 20K Magnification)	87
Figure 3.30: SEM Image of Muscovite Sheets (Control, A3, 20K magnification).....	87
Figure 3.31: Iron Content in Barrel 3 (Control).....	87
Figure 3.32: SEM Image of Muscovite Sheets (Barrel 1, A2, 20K magnification)	88
Figure 3.33: SEM Image of Muscovite Sheets (Barrel 1, A3, 20K magnification)	88
Figure 3.34: Iron Content in Barrel 1	88
Figure 3.35: SEM Image of Muscovite Sheets (Barrel 2, A2, 20K magnification)	89
Figure 3.36: SEM Image of Muscovite Sheets (Barrel 2, A3, 20K magnification)	89
Figure 3.37: Iron Content in Barrel 5	89
Figure 3.38: SEM Image of Muscovite Sheets (Barrel 3, A2, 20K magnification)	90

Figure 3.39: SEM Image of Muscovite Sheets (Barrel 3, A3, 20K magnification)	90
Figure 3.40: Iron Content in Barrel 3	90
Figure 3.41: SEM Image of Muscovite Sheets (Barrel 4, A2, 20K magnification)	91
Figure 3.42: SEM Image of Muscovite Sheets (Barrel 4, A3, 20K magnification)	91
Figure 3.43: Iron Content in Barrel 4	91
Figure 3.44: All Barrels – Distilled Water pH Test.....	92
Figure 3.45: All Barrels – Calcium Chloride pH Test.....	92
Figure 3.46: Plastic and Liquid Limits Post-Treatment	94
Figure 3.47: Plasticity Index Post-Treatment.....	94

List of Tables

Table 1.1: Variation in Electrolytes and their Effect on Electro-Osmotic Flow [20]	7
Table 1.2: Electrical Conductivity of Pore Fluids [12]	10
Table 1.3: Zeta Potential of Pore Fluids [12]	10
Table 2.1: Particle Size Breakdown of Sandy Lean Clay	27
Table 3.1: Summary of Treatment Time, Power Consumed and Failure Load	60
Table 3.2: Shear Vane and Water Content for Barrel 3- Control	74
Table 3.3: Shear Vane and Water Content for Barrel 1	76
Table 3.4: Shear Vane and Water Content for Barrel 2	78
Table 3.5: Shear Vane and Water Content for Barrel 3-Treated	80
Table 3.6: Shear Vane and Water Content for Barrel 4	82
Table 3.7: Summary of Liquid and Plastic Limits	95

Thesis Outline

The first chapter gives a background of electrokinetics, a review of shear wave velocity and examines gaps in the current research that are to be filled by this thesis.

The second chapter describes and discusses the materials used in the experimental program, their properties and characteristics and where they were sourced and examines the methods used for the given apparatuses. It goes over every part of the system, including the MATLAB codes written for controlling the system.

Chapter three presents the total results of the study and explains their significance, including the load capacity of the piles, the power consumption of the treatments, shear vane tests, shear wave velocity graphs, scanning electron microscope results and x-ray diffraction results.

Chapter four concludes the study and gives light to future avenues of research.

Chapter five contains supplementary material as well as the bibliography.

Chapter 1

The implementation of both electrokinetics for the purposes of increasing the load carrying capacity of a soil and bender elements for the purposes of determining the shear modulus of soil pose their own limitations and possible complications. This chapter identifies the complexities of each system and uses this to better understand where and how these two systems may interact.

1.1. Background

Electrokinetic treatment is a soil improvement technique that aims to induce dewatering and cementation, to increase the shear strength and load capacity of soft soil. Electrokinetics has been used as a ground improvement technique in clayey soils since the 1960s [1, 2]. However, engineers and scientists may find that determining the degree of improvement to be closer to art than science as methods to determining treatment effectiveness are limited to destructive load tests. Not only are results indeterminate, results from one treatment are rarely ubiquitous across multiple treatments due to the heterogenous nature of soil. Further, results have suggested that a longer duration of treatment does not always translate to more improvement, and the results are not scaled with time (double the time does not equal twice the results) [3].

Conventional methods of load capacity estimates are limited to soil analysis by boring and calculations that may involve erroneous assumptions. When calculations may represent a true quantification of pile load capacity, destructive methods are still needed to determine with absolute certainty that the load capacity is correct and with very large piles the equipment required for testing becomes ever larger which drives costs of construction higher.

1.2. Electrokinetics

1.2.1. Mechanisms and Models of Electrokinetic Pore Fluid Flow

Electrokinetics in geotechnical engineering refers to the process of applying a direct current (DC) electric field to moist soil with the desired outcome being an increase shear strength and load carrying capacity of soft soils or the transport of compounds within the soil [4, 5, 6, 7, 8]. In compacted soil, the electric field incites two transport mechanisms, namely electroosmosis and electromigration along with electrolysis reactions of water at the electrodes [9]. Electroosmosis is the movement of porewater via the soil pores by the electric field. In negatively charged soils (i.e. clayey soil), water is transported from the positive electrode (anode) to the negative electrode (cathode). The flow rate of pore water can be quantified by the Helmholtz Smoluchowski Model.

$$k_e = -\frac{\epsilon_w \zeta}{\mu} \tau n \quad (1.1)$$

Where k_e ($m^2/s \cdot V$) is the coefficient of electroosmotic permeability, ϵ_w (F/m) is the permittivity of pore water, ζ (V) is the zeta potential, μ ($N \cdot \frac{s}{m^2}$) is the dynamic viscosity of water and n is the porosity of the soil. Toruosity factor τ is included to make the model valid for the non-linear flow paths in soil [10].

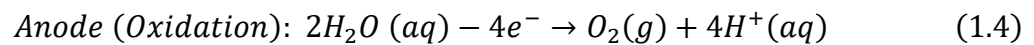
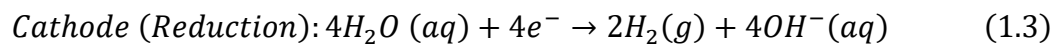
Electromigration, the movement of ions in the pore water toward the oppositely charged electrode, is best represented by the Nernst-Townsend-Einstein relation,

$$U_j^* = \frac{D_j z_j F}{RT} \tau n \quad (1.2)$$

Where U_j^* ($m^2/s \cdot V$) is the effective ion mobility of species j , D_j (m^2/s) and z_j are the diffusion coefficient in dilute solution, and valence of species j , F and R are Faraday's

constant (96 487 C/mol) and the universal gas constant (8314 J/(mol·K)), T is the absolute temperature in (K), τ is the tortuosity factor and n is the porosity of the soil [10].

Electrolysis reactions at the electrodes cause the formation of an acidic front at the anode and a basic front at the cathode. The electrolysis reactions at the electrodes are as follows:



Each front moves towards the oppositely charged electrode by electromigration while electroosmosis furthers the transport of the acid front towards the cathode [10]. Because the presence of an alkaline environment is associated with the precipitation of cementing agents, cementation is often limited to the cathode [11].

Due to the electrolysis reactions at the anode, as the treatment is administered, a metallic anode, in particular iron, is slowly oxidized and corroded making the use of electrokinetics problematic for long durations of treatment. For some forms of tests, sacrificing the anode to promote cementation and dewatering is acceptable, as is the case for the anode used in dewatering fluid fine tailings shown in Figure 1.1. In other forms of treatment, especially in cases where foundation elements are used as the anode, limiting the amount of current is essential to reduce the magnitude of corrosion [12, 13, 10, 11].



FIGURE 1.1: ANODE OF SYSTEM AFTER TESTING SHOWS HIGH LEVEL OF CORROSION [14]

1.2.2. Physical and Chemical Factors affecting EK Process

The use of electrokinetics for the strengthening of weak soils and sediments has been routinely reported in the literature for more than 50 years [1, 2]. The processes involved however are somewhat complicated as they include the movement of both positively and negatively charged ions in opposite directions in a heterogeneous soil matrix composed of various constituents including microorganisms, organic and inorganic compounds. Furthermore, the induction of redox reactions tend to induce various reactions and the creation of new compounds. The applicability of such a technique is limited to both its economic feasibility, its physical limitations to create a desired result, and the ability of those conducting the treatment to anticipate and resolve possible negative effects such as movement of metals and chemical compounds.

The physical limitations are mostly due to the changes that occur during treatment such as the development of pH fronts and gradients due to electrolysis at the electrodes, ion concentration gradients due to the movement of cations and anions in opposite directions induced by the electrical field and the creation of new chemical species, and the cascade of

effects these changes have on hydraulic conductivity, water content, electrical conductivity, all of which may have lasting negative consequences to nearby systems (groundwater sources etc). [15, 16, 17].

1.2.2.1. Effects of pH on EK Process

The pH of a soil and its ability to remain stable often governs the motion of ionic species, and in turn the water within the soil matrix [18, 19]. The flow of porewater under electroosmotic flow is governed by the presence of a difference of charge (electrical potential in volts) between the fixed and free parts of the electrical double layer, known as the zeta-potential. For materials with negative zeta-potential (i.e. clayey soils), water moves towards the cathode. The zeta-potential of a soil matrix is often highly dependent on the pH of the mixture [18].

In low pH environments (acidic), the zeta potential can be positive and subsequently the flow of pore fluid is from cathode to anode. This occurs when the low pH causes the soil to pass its point of zero charge (PZC), reversing the flow. Some soils are more sensitive than others are to changes in zeta-potential due to pH changes, such as Wyoming Bentonite (Figure 1.2). A negative electrophoretic mobility (the relationship between fluid velocity and electric field potential) represents pore-fluid flow towards the cathode. The addition of enhancement and chelating agents often has drastic effects on the pH vs flow characteristics of a given soil under an electrical current as seen in Figure 1.2. and Figure 1.3.

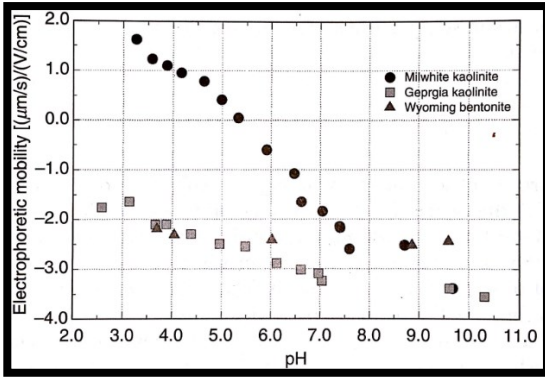


FIGURE 1.2: ELECTROPHORETIC MOBILITY VS PH OF THREE CLAYS [18]

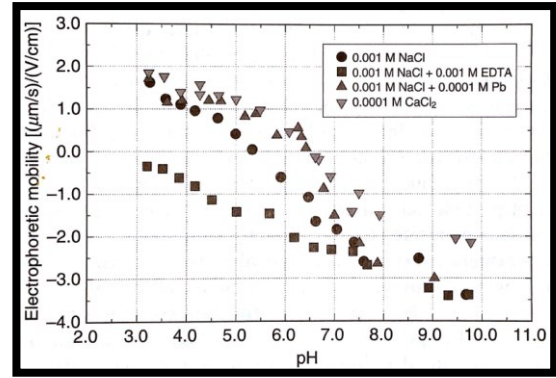


FIGURE 1.3: ELECTROPHORETIC MOBILITY VS PH OF MILWHITE KAOLINITE IN VARIOUS PORE-WATER SOLUTIONS [18]

1.2.2.2. Point of Zero Charge and Flow Reversal

An experimental study performed by Yeung [20] with Milwhite kaolinite was divided into eight stages to explore the effects of adding bases to both anode and cathode reservoirs. Initially the soil was at its PZC at which point a base solution was added at the anode to promote flow from anode the cathode. Adding deionized water to both reservoirs reversed the flow completely towards the anode. When electroosmotic flow was towards the anode, adding solutions at the anode was ineffective in correcting the flow direction, further emphasizing the relevance of pH on soil zeta-potential and in turn the electroosmotic flow (Figure 1.4 and Table 1.1).

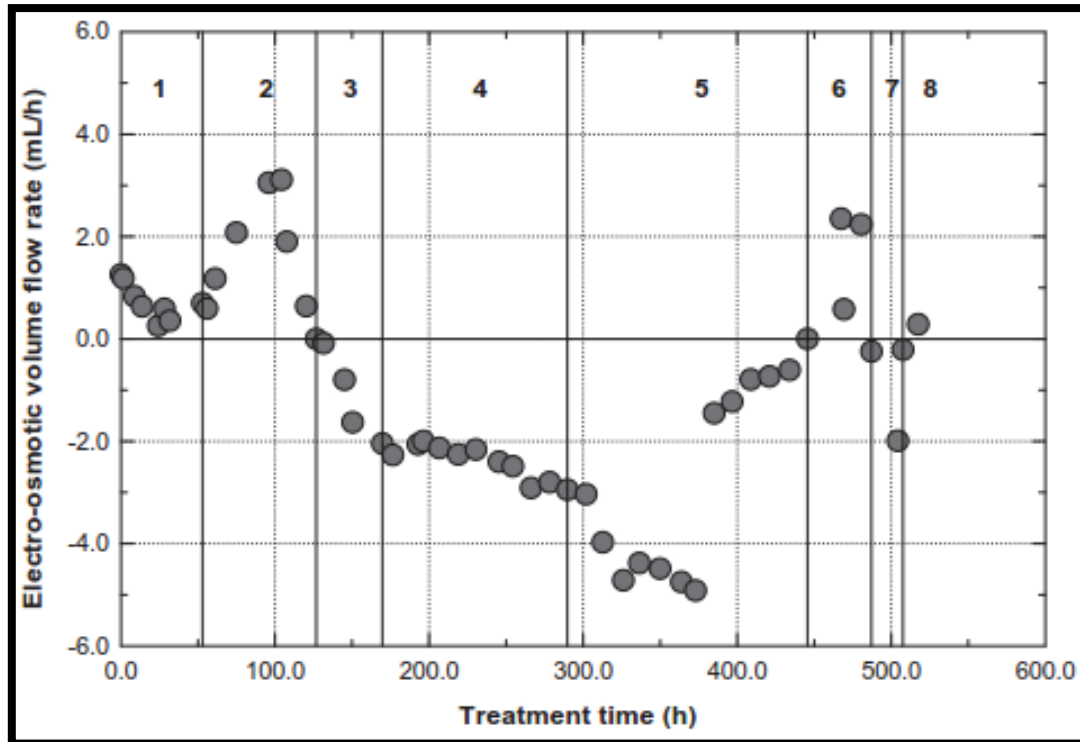


FIGURE 1.4: ELECTROSMOTIC FLOW RATE ACROSS TREATMENT TIME WITH VARIATIONS OF ANOLYTE AND CATHOLYTE [20]

TABLE 1.1: VARIATION IN ELECTROLYTES AND THEIR EFFECT ON ELECTRO-OSMOTIC FLOW [20]

Stage	Treatment time (h)	Treatment duration (h)	Reservoir solution ^a		D.C. electric field applied (V/m)	Electro-osmotic flow volume (ml) ^b	Average coefficient of electro-osmotic conductivity k_e ($m^2/V s$)
			Anode	Cathode			
1	0–52.93	52.93	NaHCO ₃	H ₂ O	157.41	33.49	2.45×10^{-10}
2	52.93–126.80	73.87	H ₂ O	H ₂ O	157.35	124.50	6.52×10^{-10}
3	126.80–169.75	42.95	H ₂ O	H ₂ O	157.21	-48.19	-4.3×10^{-10}
4	169.75–289.81	120.06	NaHCO ₃	H ₂ O	157.28	-290.87	-9.4×10^{-10}
5	289.81–445.65	155.84	NaHCO ₃	NaHCO ₃	129.92	-387.21	-1.2×10^{-9}
6	445.65–487.18	41.63	NaHCO ₃	NaHCO ₃	65.35	20.93	4.69×10^{-10}
7	487.18–507.61	20.43	CH ₃ COOH	NaHCO ₃	105.38	-8.37	-2.14×10^{-10}
8	507.61–517.46	9.85	NaHCO ₃	NaHCO ₃	262.47	4.19	9.87×10^{-11}

^aConcentration of NaHCO₃ is 0.25 M adjusted to pH 9 by 0.1 M NaOH; concentration of CH₃COOH is 0.01 M.
^bElectro-osmotic flow from the anode towards the cathode is defined as forward and vice versa.

As mentioned in a previous section, the direction of electroosmotic flow is often dependant on pH. However, this is only the case for variable-charge soils, and stems from where these soils develop their charged properties. All soils have intrinsic and extrinsic charge properties. These include their: (a) permanent structural charge due to isomorphous substitution, (b) net proton charge caused by differences in hydrogen and hydroxide concentrations complexed

to soil particle surface functional groups (SFG), (c) inner-sphere complex charge due to the balance of anion and cation concentrations other than H^+ and OH^- in SFG, and (d) outer-sphere complex charge due to ions bound to outer-sphere surface complexes. Lightly weathered soils often have mineral compositions of stable, less reactive groups, while more weathered soils often contain reactive hydroxide groups. The less weathered soils tend to exhibit stable surface charges under a variety of pH because the permanent structural charge is the dominant surface charge source [18]. The Wyoming Bentonite in Figure 1.2 is an example of a permanent-charge soil, while the Milwhite Kaolinite would be termed a variable-charge soil in that specific electrolyte solution.

The effects of pH are important for soil strength improvement due to its influence on the direction of porewater flow and heavy metal dissolution and precipitation. When cementation of soil solids via the addition of iron from the electrodes is desired, the precipitation and sorption of heavy metals is beneficial [21, 22].

1.2.2.3. Effects of Soil and Porewater Conductivity on Electrokinetics

Because the transport mechanisms that arise from electrokinetics rely on the flow of current, the capacity of the soil-porewater matrix to conduct electricity is very important. The loss of matrix-electrode contact can result in the halt of the electrokinetic process, and a higher water content is generally advantageous due to its tendency to promote higher conductivity (seen in soil conductivity tests) and fill gaps between the soil and electrodes due to the nature of liquids.

It has also been shown that the introduction of electrolytic solutions heavily promotes the flow of water through the system. This can be seen in many experiments, such as those performed by Cameselle [23] in which various acids were added as anolytes, showing various

effects to current intensity (Figure 1.5), power consumption (Figure 1.6), and electro-osmotic flow (Figure 1.7). In Cameselle [23] after 27 days of treatment, the pH at the anode and cathode were adjusted from low to high and high to low, respectively, for 13 days (i.e. day 40 of treatment). As the acids and bases migrate through the soil, they gradually increase the conductivity of the soil because in liquids, it is the presence of ions that increases the conductivity [18].

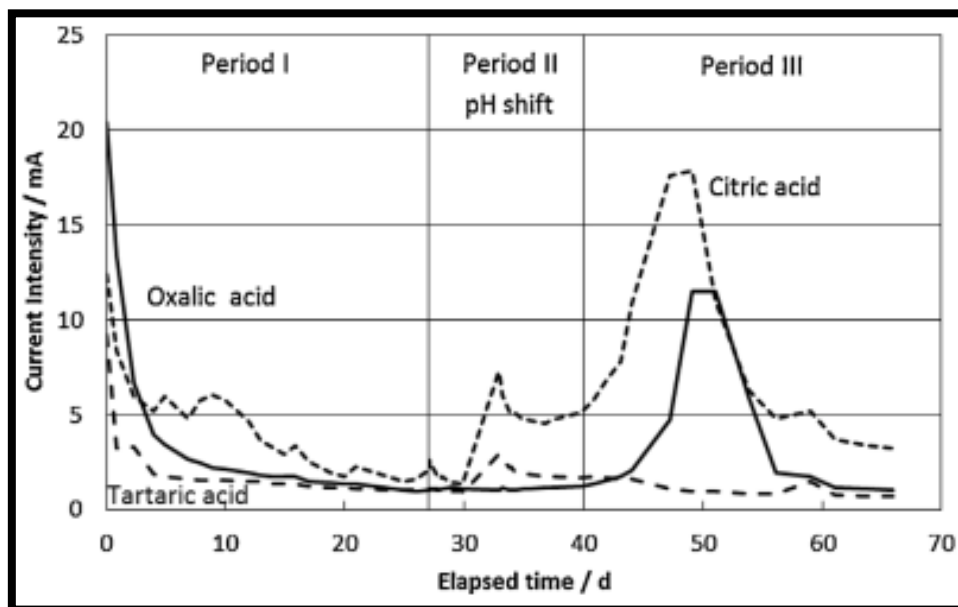


FIGURE 1.5: CURRENT INTENSITY DURING EK OF VARIOUS ACIDS AS ANOLYTE WITH ACTIVE pH ADJUSTMENT DURING PERIOD II [23]

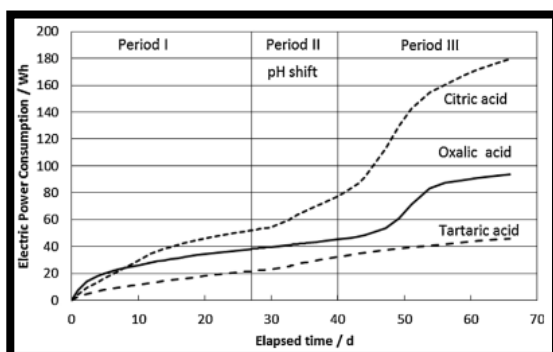


FIGURE 1.6: POWER CONSUMPTION DURING EK OF VARIOUS ACIDS AS ANOLYTE WITH ACTIVE pH ADJUSTMENT DURING PERIOD II [23]

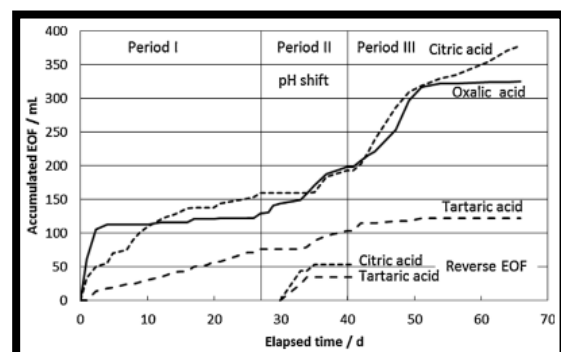


FIGURE 1.7: ELECTRO-OSMOTIC FLOW DURING EK OF VARIOUS ACIDS AS ANOLYTE WITH ACTIVE pH ADJUSTMENT DURING PERIOD II [23]

This suggests that as the ionic electrolyte permeates through the sample, the electro-osmotic flow increases for a relatively brief period until the system is again depleted of ions by this elevated level of electro-osmotic flow, which causes the flow to reduce and resistance to increase.

The efficiency of electro-osmotic flow is highly dependent on the zeta-potential of the soil-porewater solution, as quantified by the Helmholtz Smoluchowski Model in Eq. (1.1). A great deal of the soil charge that creates the diffuse double layers is often derived from soil hydrogen and hydroxide ions (pH), and many other ions. In other words, the efficiency of the electro-osmotic flow is highly dependent on the tendency for the soils physio-chemical properties to change across various pH and ion concentrations, and the tendency for a given soil to buffer the pH under treatment.

Laboratory experiments performed by Mohamedelhasan [12] examined the effectiveness of improving the strength of a saturated clay in a variety of pore fluids using EK. The conductivity and zeta potential of the four fluids are shown in Table 1.2 and Table 1.3. Only diluted zeta potentials of the seawater are available for technical reasons.

TABLE 1.2: ELECTRICAL CONDUCTIVITY OF PORE FLUIDS [12]

Distilled Water:		
	Electrical Conductivity, mS/cm	0.008
	pH	6.7
Lake Water:		
	Electrical Conductivity, mS/cm	0.1
	pH	7.2
Tap Water		
	Electrical Conductivity, mS/cm	0.11
	pH	7.7
A-Seawater		
	Electrical Conductivity, mS/cm	54.8

TABLE 1.3: ZETA POTENTIAL OF PORE FLUIDS [12]

Suspension Fluid	Zeta Potential (mV)
Distilled Water	25 ± 2.1
Lake Water	28 ± 2.3
Tap Water	32 ± 2
10% A-Seawater	15 ± 1.3
27% A-Seawater	11 ± 1
40% A-Seawater	9 ± 0.8

When comparing the power consumption with the electro-osmotic flow of all four fluids it can be seen that fluids with low conductivity and high zeta potentials perform the best (Figure 1.8) and the fluid with the highest conductivity and the lowest zeta potential performs the worst (Figure 1.9) during the EK treatment phase of the experiment.

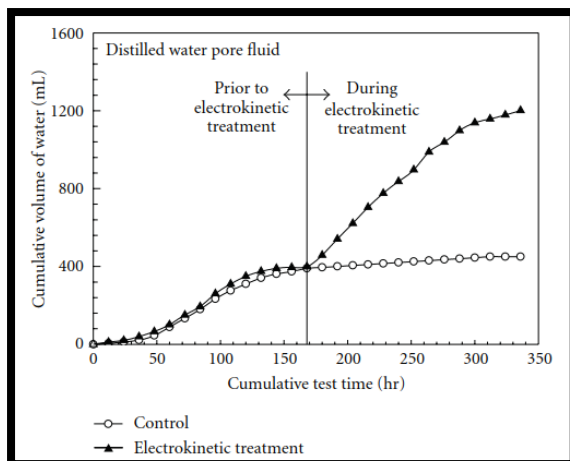


FIGURE 1.8: CUMULATIVE VOLUME DISCHARGED DURING EK TREATMENT WITH DISTILLED WATER. [12]

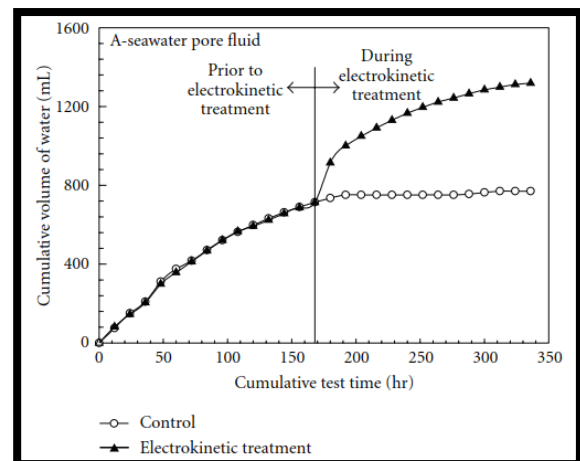


FIGURE 1.9: CUMULATIVE VOLUME DISCHARGED DURING EK TREATMENT WITH SEAWATER [12]

Also note that in the experiment using seawater the flow out of the sample before electrokinetic treatment is substantially higher, seen in Figure 1.9. This is due to the low zeta potential of the seawater which causes the diffuse double layers to shrink. This effect is reflected in the water content of the samples with distilled water before electrokinetic treatment which is less hydraulically conductive and retains a great deal of water due to dilated diffuse double layers shown by Table 1.3 and Figure 1.8.

Altogether, the physical and chemical properties of the soil matrix play an integral role in the effectiveness of EK as a soil improvement technique and as of yet there is little consistency in results, nor in treatment and testing procedures.

1.2.3. Increasing the Load Capacity of Foundations

Because of the chemical and physical effects direct electrical current has on soil-water systems, it creates stiffer and stronger soil structures. This occurs by two mechanisms: increases in effective stress due to dewatering, which leads to consolidation and a lower water content, and cementation [24, 25, 26, 27, 28]. Cementation is the creation of new bonds, which is usually spurred on by the presence of alkaline pore fluids in the presence of iron, calcium binding agents or other cementing ions [22, 24, 25, 26, 27].

Micic et al. [22] conducted tests on skirted foundation models and found that increases in load capacity of up to three times were observed. When shear vane tests were performed in the treated soil, comparisons in the treated and untreated soil showed vast differences in soil shear strength at the same water content. This led the authors to conclude that electro-cementation had occurred that created bonds that increased cohesion amongst the soil particles and adhesion between the soil and foundation elements.

Shang et al. [11] also observed similar results when performing experiments with calcareous soil treated with two separate stabilizing agents, calcium chloride and aluminium sulphate. The study determined the optimum solution to increase unconfined shear strength of the soil and was able to determine the mobility of the two under electrokinetic influence. It found that the calcium chloride permeated further and created the greatest increase in cementation compared to the control test, with soil effective cohesion increasing from 0 to 11 kPa at the cathode. Management of soil pH through current intermittence and polarity reversal helped mitigate corrosion of electrodes and enhance the development of cohesive bonds at the cathode.

Additional research performed by Asavadirbdeja and Glawe [7] examined the mechanisms that cause cementation in electrokinetics and implemented depolarization at the electrode by supplying a solution of calcium ions with a pH of 10 to the anode to offset the production of hydrogen. The results showed that an equivalent increase in soil strength was achieved. However, in the depolarized tests the improvement was seen in 70% of the soil profile (vs 20% in control) and the presence of pozzolanic reactions were greatly increased.

1.3. Bender elements

The use of bender elements to determine the shear wave velocity is a practical and inexpensive means of determining the stiffness of soils in low strain conditions [29, 30, 31, 32, 33]. Bender elements, also known as piezoelectric actuators, are made from polarized materials that exhibit mechanical deformation under applied electrical charge and vice-versa. Piezoelectric benders operate like a cantilever beam and, in general, vibrate along their weak axis. The piezoelectric elements used in this research are made of ceramic and are electrically polarized at high temperature and voltage [34]. This ceramic is affixed to a metal shim and the application of an alternating current causes it to vibrate at the current's frequency. Thus, it is possible to send and receive mechanical vibrations with ease with the only limitation being the sampling and bit rate of the data acquisition system.

Ogino et. al [35] conducted research to examine discrepancies amongst various techniques of determining shear wave velocity finding that soft soils rendered the least dispersive results. When the time-domain peak to peak technique was compared to cross-correlation technique, the shear wave velocity matched only when the highest correlation matched with the first of the signal, otherwise shear wave velocity was underestimated.

Kawaguchi et al [36] performed a suite of bender element tests on a variety of soils ranging in particle size and stiffness. They were able to create a series of conditions to aid other researchers in selecting suitable input frequencies based on soil stiffness to produce waves that would have matching output and input frequencies. This was done to create reproduceable results with less variability in shear-wave velocity.

Although many researchers have experimented with bender elements for determining shear wave velocity, no standard has been adopted to guide researchers with respect to test dimensions, equipment standards, or interpretation of test data [36, 37]. Although in the published research researches agree on many factors, contradictions exist.

1.3.1. Bender Element Wiring

The use of parallel wiring for bending actuators and series wiring for receivers is considered best practice [38]. Parallel wiring refers to when both ceramics are connected to one lead with the centre shim connected to the other lead. Series wiring refers to the case when one lead is connected to one face and the other is connected to the other face with the centre shim disconnected.

As the received signal produces equal and opposite voltage on each face of the element when connected in series, the signal is effectively doubled at the receiving element [39]. This is helpful when data acquisition equipment has a lower bit rate, as received signals have a very low amplitude, normally producing voltages in the mV range [36, 38]. Parallel wiring is ideal for sending signals for the opposite reason, only half the voltage is required to produce equal force and deflection of the element [38, 39]. The use of series wiring poses its own set of challenges when placed in soils with relatively high electrical conductivity. Electrical coupling, known as the cross-talk phenomena, occurs in series wired benders due to the presence of

electrical fields produced by the sending unit, corrupting the receiver's ability to pick up vibrations without interference [40]. This is essentially radio frequency noise and is corrected by shielding and grounding the element, however even these fixes can prove somewhat ineffective and difficult to implement [40, 41].

1.3.2. Bender Dimensions

Although there are no guidelines as to the size and dimensions of bender elements, long and narrow actuators for receiving and short and wide actuators for sending is mathematically the most ideal scenario [40]. This is because the voltage generated is proportional to the length of the element and inversely proportional to its width whereas the force generated increases with the element width and decreases with its length [39]. Equation 1.5 is the mathematical relationship between voltage and force for series-wired bender elements and equation 1.6 is for parallel-wired benders [39].

$$V = \frac{3FL^2g_{31}}{2WT} \quad (1.5)$$

$$V = \frac{3FL^2g_{31}}{4WT} \quad (1.6)$$

Where V (V) is the voltage produced by the excitation, F (N) is the force applied to the bender, L (m) is the active length of the bender, g_{31} is a coefficient relating applied stress to produced electric field (V/mN) which is dependent on temperature, and W (m) and T (m) are the width and thickness of the bender, respectively.

In practice, it is most simple to keep the bender elements of equal dimensions as this ensures they will have similar bandwidths and frequency response characteristics, which is important for frequency domain analysis. It is imperative that benders be properly aligned to achieve 100% shear wave transmission efficiency [38].

1.3.3. Ideal Frequency

Research has shown that to transmit crisp shear waves through soil, the ratio between the distance between benders and the wavelength of the wave (L/λ) must be at least 2, however many inconsistencies between researches has been observed [42]. Research performed by Biot [43, 44], examined the theoretical relationships between frequency, pore size and wave velocity, finding that various factors influence how wave velocity is affected by frequency, which explains the inconsistencies amongst research performed by geotechnical engineers using bender elements. A 'characteristic frequency' is coined as a frequency that all fluid-saturated porous media exhibits and is used to normalise results.

The appropriate selection of bender size is therefore dependent on distance between elements and the expected shear wave velocity of the soil. Bender size will dictate the benders useable bandwidth, therefore designing the bender to have a natural frequency above the expected frequency needed is best practice because benders must oscillate in the first mode of vibration to transmit maximum force. If the benders resonant frequency is below the desirable operating frequency, amplitude of traveling shear waves is greatly reduced and problems may occur due to lack of signal amplitude at the receiver.

A shorter elements natural vibrational frequency will depend more on the properties of the bender mounting plate apparatus than the surrounding soil stiffness while a longer element will result in more variation of bender response due to soil stiffness properties [38]. This is critical in the tests where the soil stiffness is expected to increase during the treatment, changing the response characteristics of the system and necessitating a short cantilever length. In short, the bandwidth of the bender element must match the 'bandwidth' of the soil.

1.3.4. Wave-Form

Among all the research performed, there is very good agreement that the use of sinusoidal waves yields best results in travel time determination compared to other forms such as square or triangular wave forms. This is mainly due to the tendency for shear waves to revert to the smoother sinusoid when passed through soil [35, 36, 40].

1.4. Signal Analysis Techniques

1.4.1. Time Domain

The simplest technique of calculating shear wave velocity is the Time Domain (TD) peak-to-peak (PP) and start to start (SS) methods. Single-cycle sine waves of varying frequency are individually input to the sending element and response is collected by the receiver. Travel time is best approximated when the transmitted and received waves have the same frequency, yielding SS and PP travel times with the least variability [36]. The time difference (Δt) between the sending and receiving of the shear wave is divided between the tip-to-tip distance (D) of the elements to determine shear wave velocity (V_s) as shown in equation 1.7 [35].

$$V_s = \frac{D}{\Delta t} \quad (1.7)$$

The SS arrival time is defined as the time coinciding with the point of first positive deflection of the received signal, while the PP time coincides the first peak of the received signal, as seen in Figure 1.10.

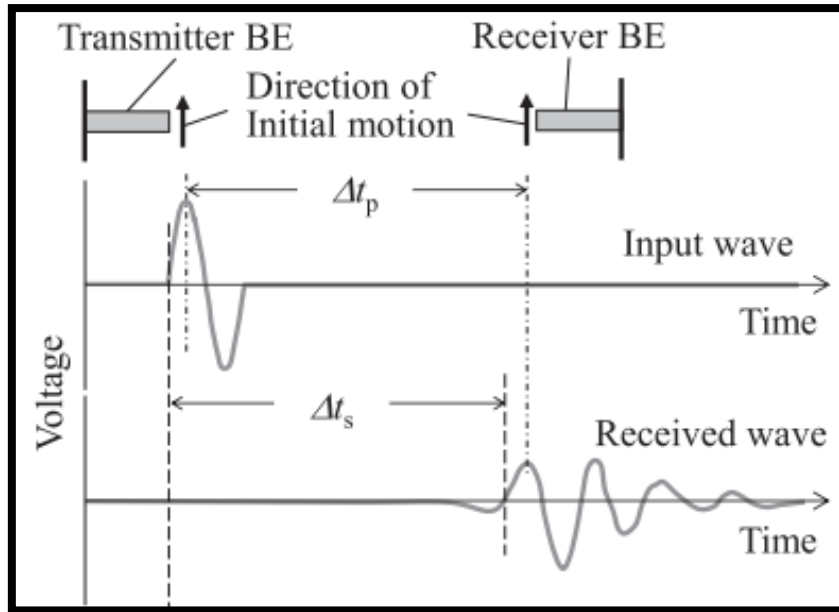


FIGURE 1.10: DIAGRAM OF SHEAR WAVE RESPONSE OF BENDERS [36]

Although this technique is very simple it is also fraught with flaws. It is highly dependent on human discretion for the selection of arrival time, and if the correct signal frequency is not chosen, near-field effects due to compression wave arrival make the choice of arrival time even more difficult [31, 45].

Many researchers have stated that the tip-to-tip distance to wavelength ratio (L/λ) must be above or below a certain value to mitigate the near-field effects. Results across many different sample types and confining pressure show that this ratio can range from less than 1 to 8 [42]. This has lead researchers to conclude that the presence of near field effects at a certain frequency are more-so dependent on specific soil type, stiffness of soil, and confining pressures than any set guideline of L/λ ratio. Therefore, the optimal frequency to mitigate near-field effects must be experimentally determined for a given soil under those specific conditions. This makes the use of the time-domain technique more arduous and ambiguous as the user must choose a range of frequencies to perform the bender element tests with and then must perform a manual analysis of the collected data. If the range of frequencies chosen

by the user is not broad enough and poor results are obtained, then the user must determine if a higher or lower frequency is needed and perform the full suite of tests again, all while hoping that the ideal set of frequencies does not fall outside of the useable bandwidth of the bender.

The cross-correlation (CC) function is used to compare the sent wave to the received wave. The advantage of the cross-correlation technique is that it is less dependent on the users sense of judgement of true arrival time and uses a mathematical formula instead [46]. Additionally, in the presence of near-field effects it is still able to determine arrival time with great accuracy, unlike the SS and PP methods. The CC function is given by

$$CC_{xy}(\tau) = \lim_{T \rightarrow \infty} \frac{1}{T} \int_0^T x(t) y(t + \tau) dt \quad (1.8)$$

where the transmitted and received signals are represented by $x(t)$ and $y(t)$ respectively as a function of time, T is the total recording time and τ is the incremental delay. The arrival time of the shear wave corresponds to the maximum point of the $CC_{xy}(\tau)$ function. The cross-correlation function can be more easily analysed in the frequency domain by the following equation [36]

$$CC_{xy}(f) = X(f) Y(f)^* \quad (1.9)$$

where $CC_{xy}(f)$, $X(f)$, and $Y(f)$ are the Fourier transforms of their respective conjugate, and the asterisk represents the complex conjugate. Once this operation is completed, the inverse Fourier Transform of $CC_{xy}(f)$ is calculated and the travel time is defined as the time of the peak in the correlation function. Like the TD method, multiple input functions of $x(t)$ are input in the form of specific frequency single-cycle sine waves and the data is processed for each individual frequency.

1.4.2. Frequency Domain Technique

Frequency domain techniques vary considerably from time domain techniques. They do not use a single-cycle sine wave but instead implement frequency sweeps to measure the response of the soil to a broad spectrum of frequencies. Travel time is derived from the phase difference of the cross-spectrum between received and transmitted waves [35, 30]. Both group and phase velocities can be calculated, corresponding to the tangent and secant of the spectrum, respectively, at frequency f .

$$\Delta t_{gr} = -\frac{1}{2\pi} \frac{\delta\phi}{\delta f} \quad (1.10)$$

$$\Delta t_{ph} = -\frac{1}{2\pi} \frac{\phi}{f} \quad (1.11)$$

Φ is the unwrapped phase of the spectrum, Δt_{gr} is the tangent and Δt_{ph} is the secant of the unwrapped spectrum frequency f

There are several sine sweep signals used that can be used. A few commonly used are: linear, logarithmic and Time Sweep Pulse (TSP). Much like the TD methods, frequency of the shear wave has great effect on shear wave velocity. Ogino et al. [35] found that when performing the frequency sweeps, an upper frequency limit (UFL) became apparent. Any frequency applied above this value the velocity of the wave became dispersive and erratic. This behaviour is similar to that presented by Biot.

The advantage of the frequency domain method is that no single frequency must be selected, and instead a broad sweep can be performed and shear wave velocity can be viewed against frequency, as shown in Figure 1.11 [35].

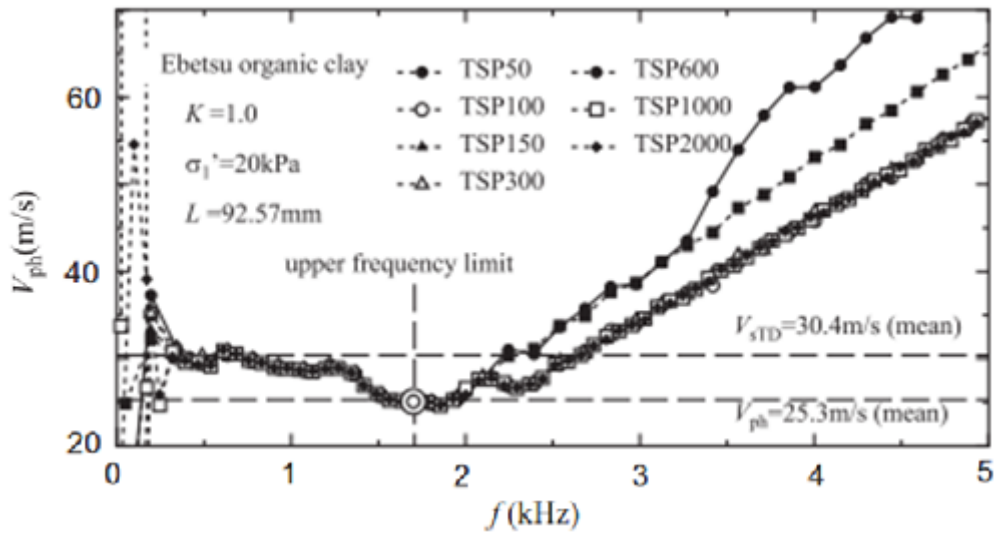


FIGURE 1.11: SHEAR WAVE VELOCITY OF EBETSU ORGANIC CLAY VS FREQUENCY OF TRANSMITTED WAVE [35]

They also found that choice of frequency sweep type has not shown to significantly affect the dependence of phase and group velocities on frequency. In fact, dispersion and scattering of travel time with frequency below the UFL was shown to be more dependent on soil stiffness and composition, when performing shear wave analysis on a variety of stiff sands and soft clays.

1.5. Shear Wave Velocity

Shear wave velocity, V_s (m/s) and density, ρ_t (g/cm^3) are related to low-strain shear modulus, G_{\max} (GPa) by the following equation

$$G_{\max} = \rho_t \cdot V_s^2 \quad (1.12)$$

Shear modulus is related to Young's compression modulus E by

$$G = \frac{E}{2(1 + \nu)} \quad (1.13)$$

Where ν is Poisson's ratio

1.5.1. Empirical Correlations of Shear Wave Velocity

Many studies have been examining the relationships between shear-wave velocity and other geotechnical parameters such as liquefaction resistance [47], damping ratios [48, 49], Studies that examined the relationship between shear wave velocity and shear strength did so by empirical means. A study by Oh et al. [50] correlated the undrained shear strength and void ratio to shear wave velocity with empirically derived parameters from marine clays. They found shear wave velocity to be highly dependent on the stress history and stress state of the soil, and that the inferred strength and measured strength were in good agreement.

Another study by Karray et al. [51] compared two granular, uncemented soils and found that a relationship between cone resistance and shear wave velocity existed for each soil depending on mean grain size.

Hussien and Karray [52] examined the practical applications of utilizing shear wave velocity to supplement or even replace traditional geotechnical parameters. They found that the particle characteristics were of great importance and that shear wave velocity varied in a relatively narrow range depending on if the soil was in a dense or loose state, and that the variation grew with increasing grain size. They cite that the prime effect of grain size and gradation was on the changing of possible void ratios which had the greatest impact on shear wave velocity. Correlations between shear wave velocity and standard penetration test N_{60} values dependant on void ratio, average particle size (D_{50}) and soil density index (I_D) were proposed for uncemented Holocene-age soils.

A paper written by Gadeikis et al. [53] found correlations between cone resistance and shear wave velocity for glacial clayey soils and other formerly glaciated areas. They compared their findings to that of other researchers and found that the results were highly dependent on

grain size, and lithology, with drastic differences in shear wave velocity between clayey and sandy soils for the same cone resistance.

A database of shear wave and cone-penetration data for Norwegian marine clays was assembled by Long and Donohue [54] to determine if relationships between the two could be used to better classify various soils. They found that G_{\max} could be estimated using correlations with water content, void ratio and plasticity index, however the influence of over consolidation is not considered through these methods. They proposed a new soil classification chart using normalized cone resistance and normalized shear wave velocity, making it possible to give more reliable estimates of stress history and OCR of soft clays in-situ by comparison with other data.

A research journal by Cai et al. [29] compared shear wave velocities of three sands in a variety of void ratio and confining pressure states using bender elements, resonant columns and torsional shear tests. They found that excitation frequency had a large impact on the determination of travel time and that higher frequencies yielded less near-field effects up to a certain threshold, and that with these sands a frequency in the range of 10-20kHz yielded good results. Variability in shear-wave velocity to confining pressure relationships were found when the fine contents of the respective sand was increased beyond a certain threshold. This agrees with other research that found that grain size distribution and void sizes played a critical role in shear wave velocity's relationship to other geotechnical parameters [52, 55]. A simplified version of Biots theory for wave-propagation in porous media is used to draw conclusions regarding the determination of mass density in soils based on their hydraulic conductivity. The simplified version of Biots theory from Santamarina et al. [56] was with characteristic frequency calculated as a function of porosity and hydraulic conductivity. The

characteristic frequency represents the border between low and high frequency soil response, as shown in Figure 1.12.

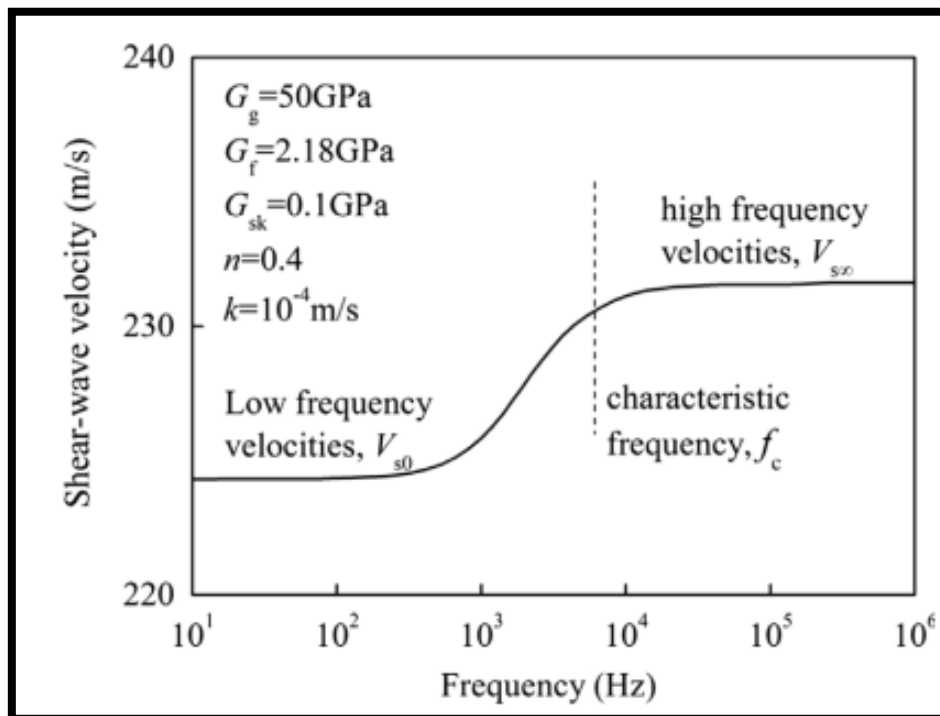


FIGURE 1.12: SHEAR WAVE VELOCITY VS FREQUENCY DISPERSION CURVE FROM [29]

Database analysis performed by Vardanega and Bolton [32] examined shear strain to shear modulus relationships of a variety of clays and silts. They examined design curves published by Vucetic and Dobry [57] and found that the data needed to be adjusted based on strain rate of the respective data, be it a static or dynamic case, and that reduced stiffness at intermediate strain levels can be estimated with knowledge of the plasticity index of the soil. They also found that neither undrained shear strength nor confining stress were able to successfully normalize shear modulus to shear strain. They concluded that it is possible to predict shear modulus behaviour when plasticity index is known when referencing the maximum shear modulus and strain state. However cone penetration resistance is not possible to predict as the shear velocity in soil is a dynamic problem that depends on the viscosity of fluids and their ability to disperse under a given strain rate.

1.6. Research Gaps

The obvious and simplest means of increasing the load capacity of deep foundation elements in current engineering practice involves increasing the element size and driving depth. Incorporating electrokinetic treatment into metal pile foundations can be quite simple and has shown positive results in increasing the load capacity. Despite the effectiveness of electrokinetics in increasing the load capacity of a pile in soft soil substrate, using electrokinetics poses two uncertainties. Namely, how much extra load will the treated pile be capable of carrying, and how long must we treat the pile to attain the maximum result (i.e. when the treatment should be completed?)

It could be possible to use shear waves to detect structural changes that electrokinetic treatment causes. Bender elements are used already in industry to generate and receive shear waves. The shear wave velocity of the soil is directly proportional to the shear modulus of the soil and is determined using a well-known formula.

Combining these two technologies could allow electrokinetically treated soil to be tested for treatment completion and effectiveness for the first time by tracking changes in shear wave velocity.

1.7. Objectives

The main aim of this thesis is to contribute in removing the uncertainties in improving the load capacity of pile foundations by electrokinetics. The specific objectives of the research are to:

- Create a non-destructive testing method to determine the soil stiffness during electrokinetic treatment. This objective was achieved by using bender elements, built and assembled in-house, which was used to monitor the shear wave velocity of the

soil during the treatment, which is directly proportional to the stiffness and shear strength.

- Develop an automated system for controlling the treatment and collecting data. This was accomplished using MATLAB software, a DT9857 Data Acquisition unit, and an amplifier.
- Process the signals afterward for shear wave velocity detection and continuous monitoring. This was done by writing MATLAB code that autonomously detects shear wave velocity and records it every hour for days at a time.

Chapter 2 – Materials, Experimental Apparatus and Methodology

The materials, equipment and methods used in the research performed are outlined in the following chapter. Because both bender element and electrokinetic treatment systems are being integrated they have a possibility of interacting. Due to this, these systems vary in some respects than if they were used separately. The design of some components vary from those of other researchers as a result.

2.1. Soil Properties

The soil used in the experimental program was sourced from a highway patrol yard on Highway 61, south of Thunder Bay, ON, with the permission of the Ministry of Transportation of Ontario (MTO). It was considered waste fill and was cited as being unsuitable for construction purposes. The soil was brown, and contained remnants of asphalt paving, indicating it was likely below a road surface before it was discarded. ASTM D422 [58] was followed for the determination of particle size distribution of the soil shown in Table 2.1 and Figure 2.1.

TABLE 2.1: PARTICLE SIZE BREAKDOWN OF SANDY LEAN CLAY

Particle Size	Fraction Present
Gravel (>4.75mm)	8 %
Sand (0.075 to 4.75mm)	38 %
Silt (0.002mm to 0.075mm)	39 %
Clay (<0.002mm)	15 %

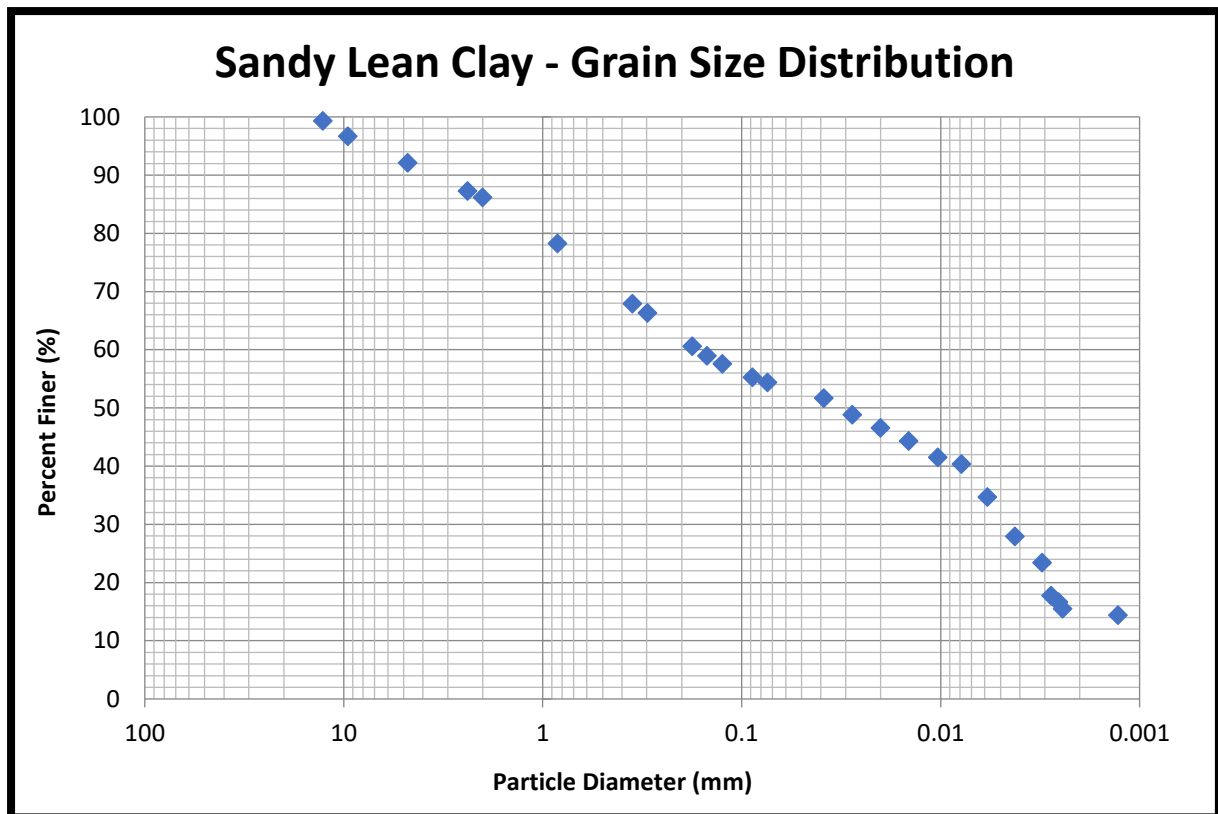


FIGURE 2.1: SANDY LEAN CLAY - GRAIN SIZE DISTRIBUTION

Atterberg Limits tests were conducted according to ASTM D4318 [59]. The liquid and plastic limits were found to be 27 and 10, respectively, giving a plasticity index of 17. The specific gravity of the soil was shown to be 2.65 by using ASTM D 854 [60]. According to the Unified Soil Classification System, the group symbol of the soil is CL and the group name is sandy lean clay [61]. The electrical resistivity of the soil was evaluated using ASTM G57 [62] and found to have a mean of 2100 ohm-centimetres. The value of the electrical resistivity is proportional to electric current according to Ohm's law (the current through a conductor is directly proportional to the voltage across the conductor and inversely proportional to the electrical resistance) and the power consumption as Power (Watts) is equal to voltage multiplied by amperage.

In the experiments of this study, voltage was kept constant. Therefore any change in current throughout the experiment can be generalized as reflecting a range in soil resistivity.

2.2. Bender Elements

At the onset of the research, it was decided that the research be as economical as possible.

Not only this, it was imperative that the presence of the non-destructive system not interfere with the process of treatment and that it be as least invasive as possible. This removed resonant column tests from the list of options and left bender elements as an ideal match as the elements are quite small. For the bender element system, much of the equipment needed for the experiment was very expensive if bought outright, namely the bender elements and DAQ associated with it, ranging from around \$2000 USD per bender element. By taking an unconventional approach, much was learned with regards to processing the signals acquired by bender elements, and how to solve the problems that arose. Not only was the research remarkably less expensive, the knowledge, skills and experience obtained were so much greater.

The piezoelectric bender elements were purchased from Piezo Systems, Woburn Massachusetts. The high strength units were purchased as the more robust nature was more appealing considering they would be buried. Both x and y poled bender elements were purchased, the model numbers were T220-A4SS-303X and T220-A4SS-303Y, respectively. The bender elements measured $\frac{1}{2}$ inch wide by $1\frac{1}{4}$ inch long and were cut in half to measure $\frac{5}{8}$ inch long. Primary differences in the bender elements are wiring configuration, seen in Figure 2.2 and Figure 2.3.

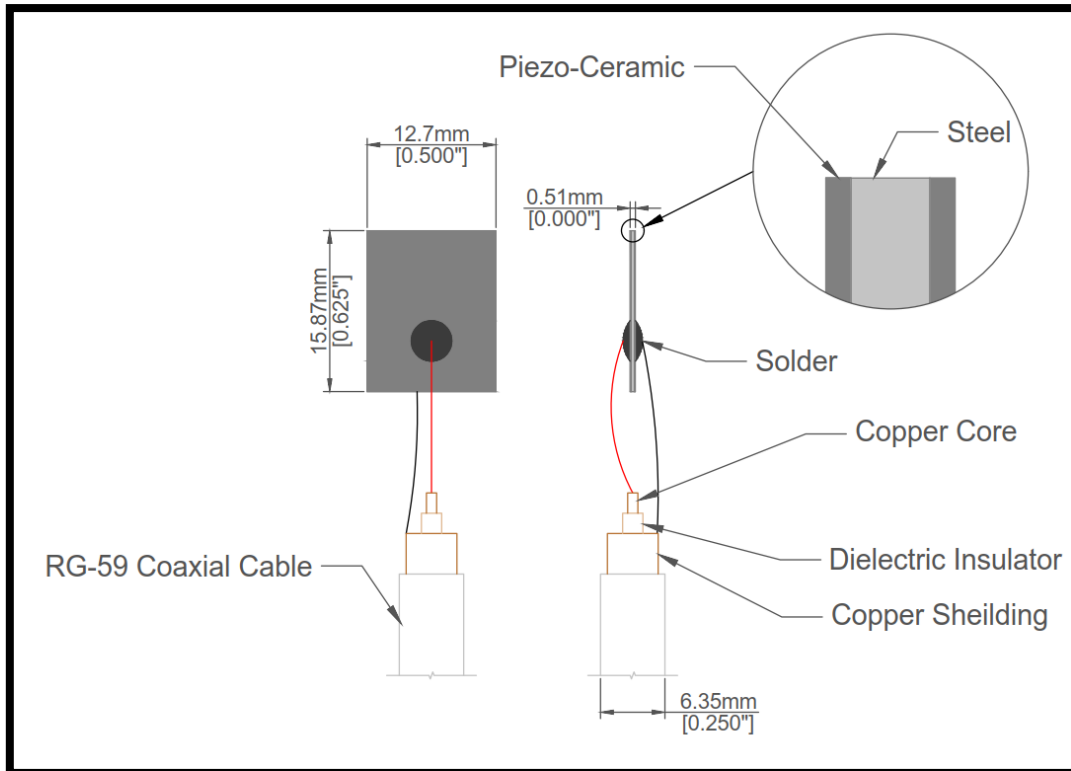


FIGURE 2.2: SCHEMATIC OF SERIES WIRED BENDER ELEMENTS

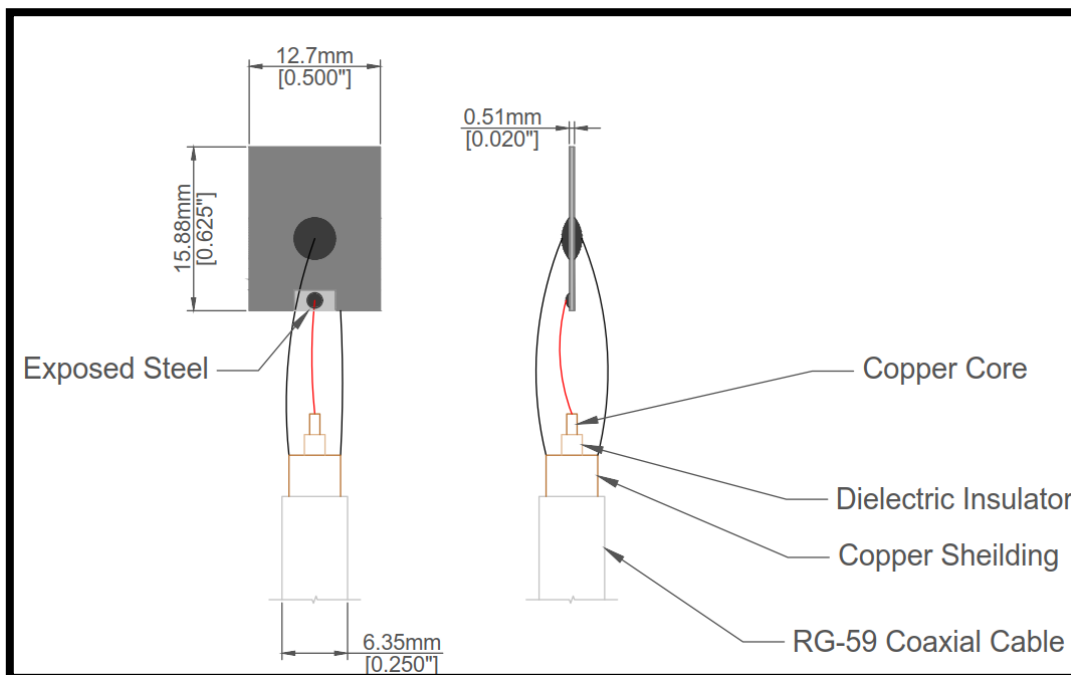


FIGURE 2.3: SCHEMATIC OF PARALLEL WIRED BENDER ELEMENTS

2.2.1. Housing

The housing for the bender elements was fashioned from a 2- ½ inch diameter stock of HDPE plastic purchased from Surecraft Plastics in Thunder Bay, ON.

As the system being developed is a two-part system (sender and receiver) that is transmitting shear waves, the two benders must be relatively well aligned and be oriented correctly to be in-phase. To accommodate this the cylinder of HDPE was cut into 1 ½ inch segments and slots were milled into the faces to house the bender element, seen in Figure 2.5 and Figure 2.6. Two ¼ inch holes were drilled through the face to allow two ¼ inch steel posts to be inserted, shown in the schematic of Figure 2.7. The bender elements and the alignment rods can be seen in place beside the pile in Figure 2.17.

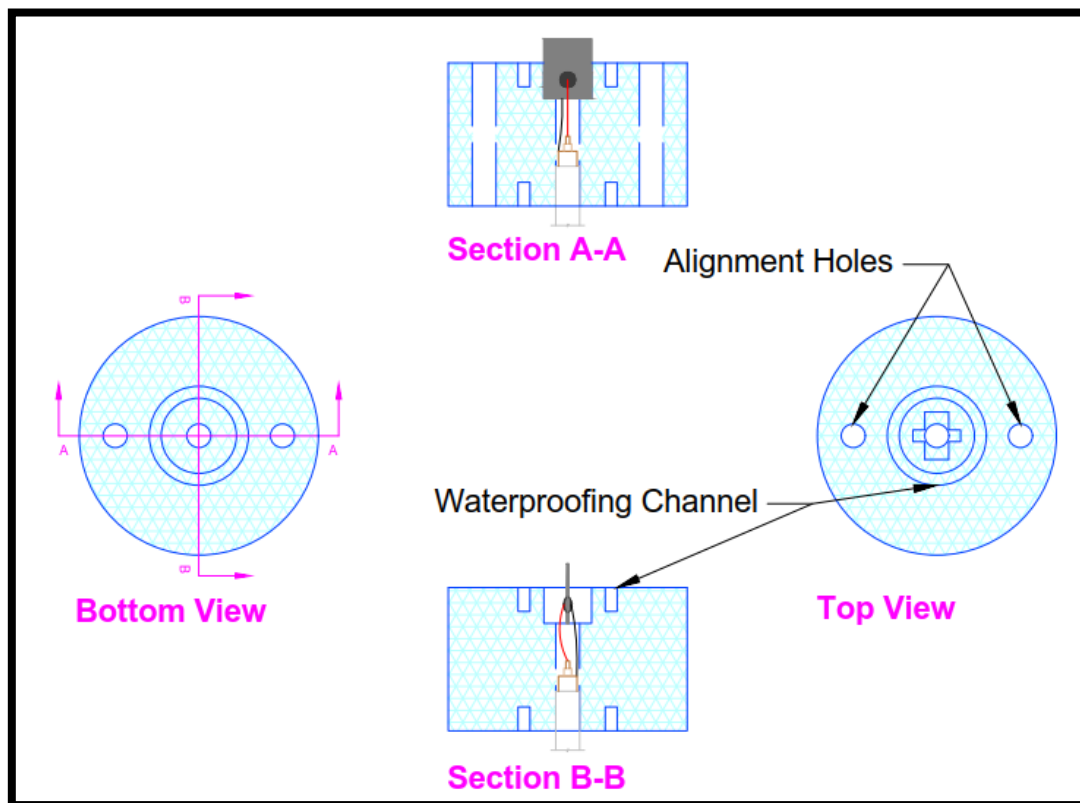


FIGURE 2.4: SCHEMATIC OF BENDER ELEMENT HOUSING

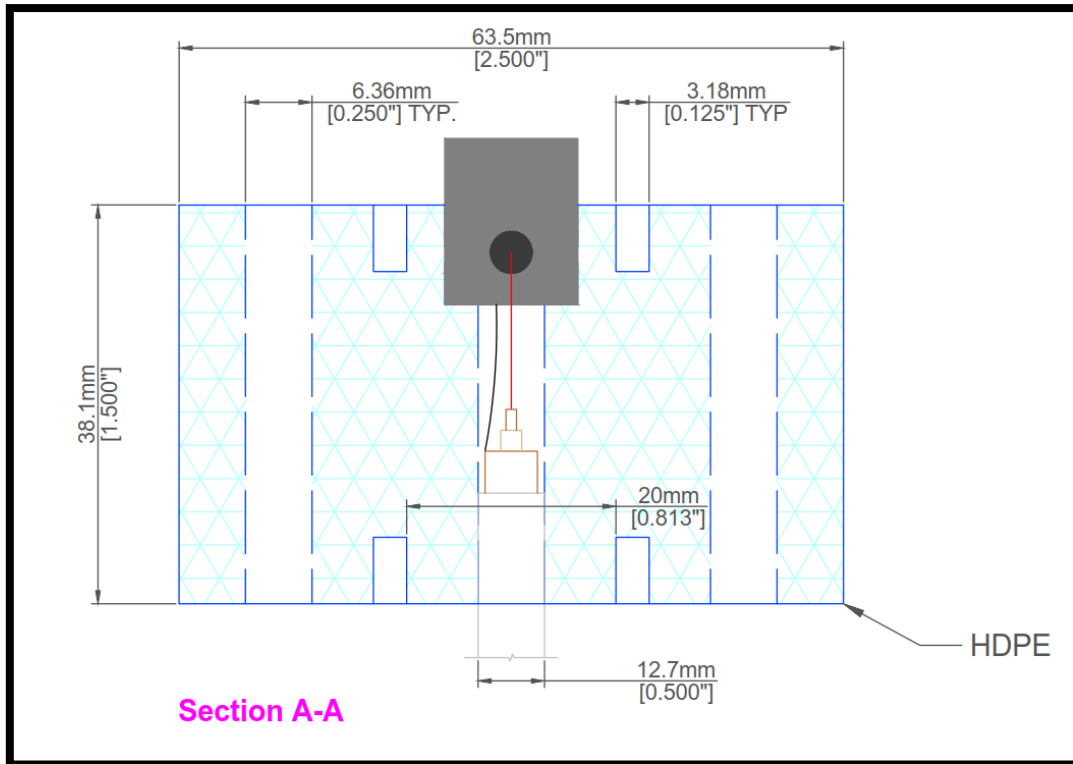


FIGURE 2.5: SECTION A-A OF BENDER ELEMENT HOUSING

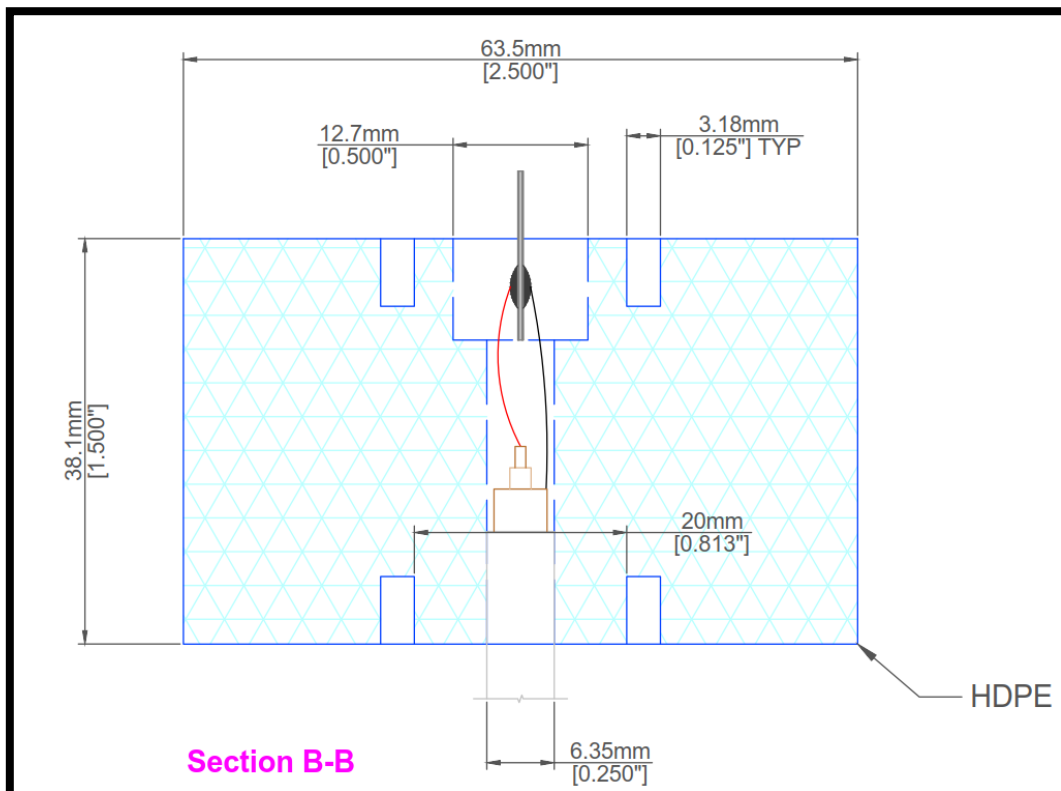


FIGURE 2.6: SECTION B-B OF BENDER ELEMENT HOUSING

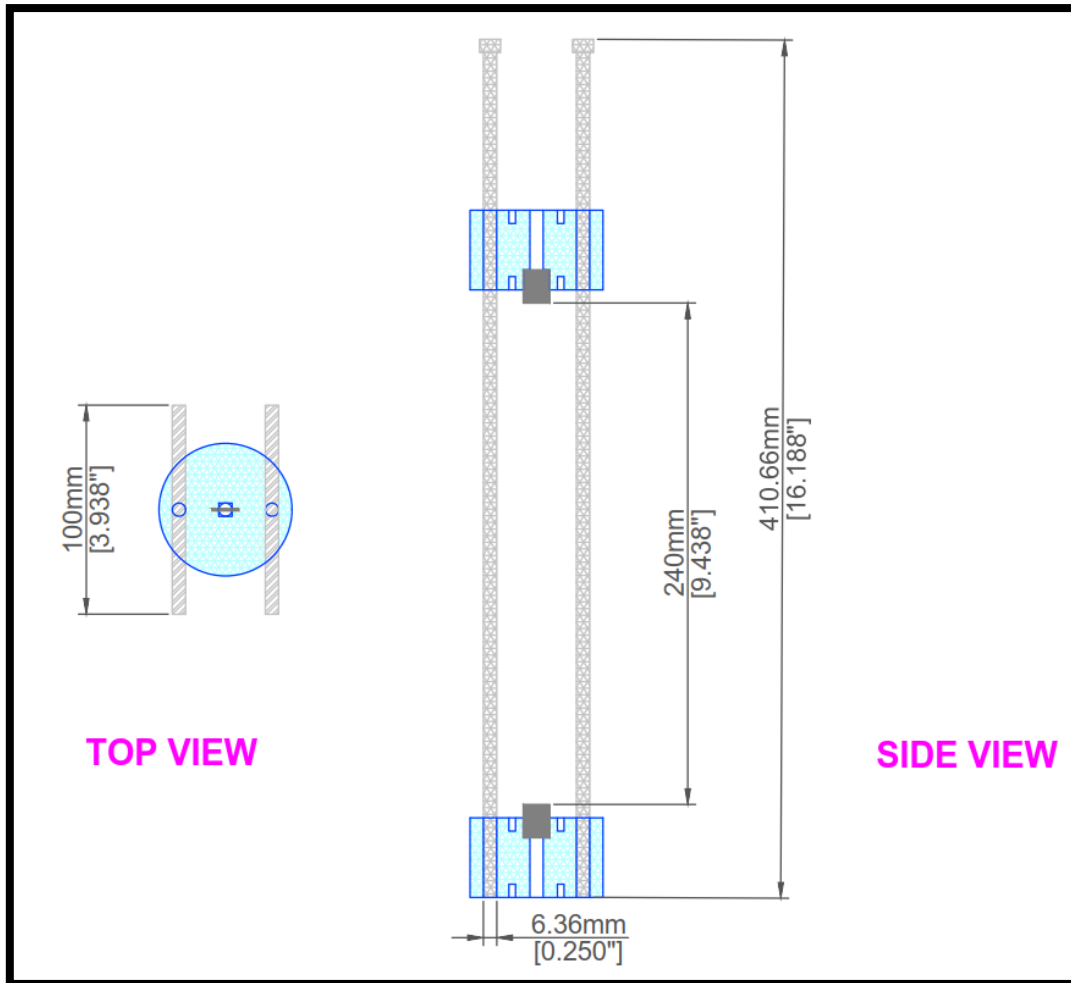


FIGURE 2.7: SCHEMATIC OF BENDER ELEMENTS WITH ALIGNMENT RODS

The coax-cable used in the experiment was RG-59. It had an impedance of 75 ohm and was chosen because it was readily available. Most coaxial cable manufactured as of recently is made with aluminium foil shielding, which is undesirable for soldering purposes. This made the purchase of older, less expensive cable ideal. Eight-foot lengths of cable were used for each bender element.

Generic lead-free solder was used, and a high quality, aggressive, organic acid flux was needed to properly prepare the surface for soldering. This was accomplished by using #67 flux, made by SuperiorFlux, which is highly diluted Dimethylamine Hydrochloride. The elements were

later covered in conformal coating and epoxy to render them waterproof and fix them firmly in their housing.

2.2.2. Construction Procedure

The bender element housing was designed to hold the benders firmly, provide a robust frame to protect the electrical connections from water and soil intrusion, and allow the paired elements to be easily aligned and accurately spaced apart. The stock of HDPE was cut into 1 ½ inch thick disks and placed on a lathe to flatten the faces and drill the centre hole for the coaxial cable to pass through.

The disk was then transferred to the mill where the holes for the two index posts were drilled, and the slot to house the benders was also milled. After this the housing was brought back to the lathe and a circular slot, like a moat, was cut on both faces to better enable the epoxy, used later, to keep water from entering the housing. This can be seen in Figure 2.8.



FIGURE 2.8: BENDER HOUSING WITH MOAT CUT

The bender elements were cut in half from their original 1 ½ inch length (Figure 2.9). The shortened segments were placed in a third hand and the 32-gauge wires were soldered on to

their respective faces. For parallel type benders, a portion of the piezo-ceramic coating was etched off, seen in Figure 2.10, with a hand-held rotary grinder and the positive lead was soldered to the inner steel shim, and two negative leads were soldered to the two piezo electric surfaces, as shown in Figure 2.11. An electrical multi-meter was used to ensure that the surfaces were electrically bonded to the coax-cable, and that the center shim did not have continuity to the piezo-ceramic coating.

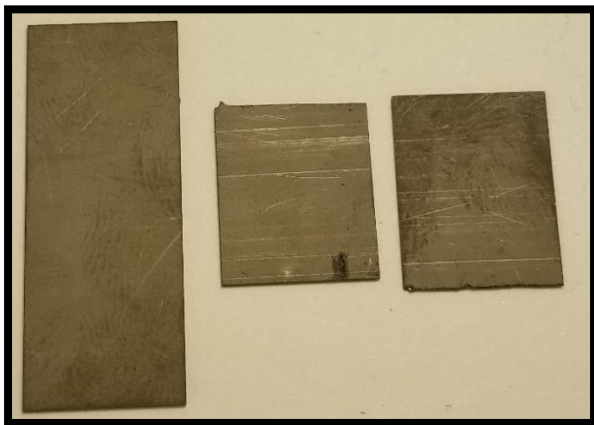


FIGURE 2.9: BENDER ELEMENTS, FULL SIZE AND TWO HALVES



FIGURE 2.10: BENDER ELEMENT WITH STEEL SHIM EXPOSED



FIGURE 2.11: A STRONG SOLDER BOND IS MADE WITH THE LEADS AND THE ELEMENT

Waterproof and chemical resistant polyurethane conformal coating was sprayed onto the surface and baked at 190 °F for 6 hours. After curing was complete, silver conductive paint was applied to the surface. The multi-meter was used to ensure that the conductive paint did

not cause shorting of the leads. Figure 2.12 shows the elements after conformal coating was applied.

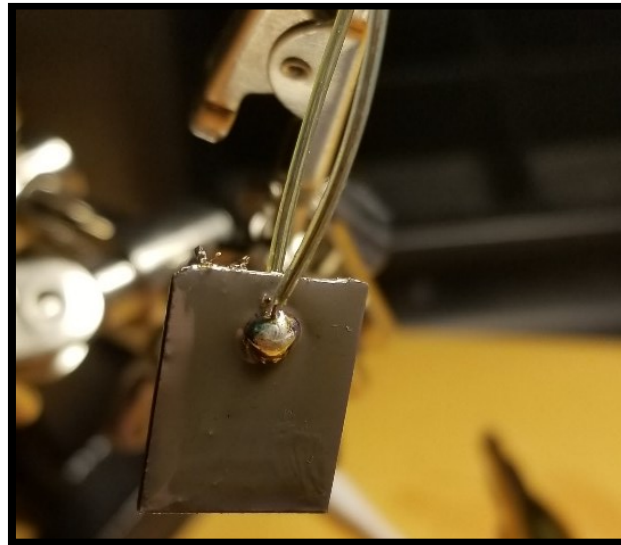


FIGURE 2.12: THE BENDER IS COATED WITH CONFORMAL COATING AND CURED

The coaxial cable was stripped accordingly, and the copper core and shielding were tinned, shown in Figure 2.13. With the bender element appropriately protected and shielded, the coaxial cable was pushed through the housing and the respective leads were soldered together, seen in Figure 2.14. The bender element is pushed into the slot in the housing (Figure 2.15), but before epoxy can be applied the housing is flame treated with a brazing torch to oxidize the surface of the HDPE to promote bonding. Epoxy is applied to bond the bender and cable to the housing, shown in Figure 2.16, and BNC connectors are used to terminate the other end of the coaxial cable.

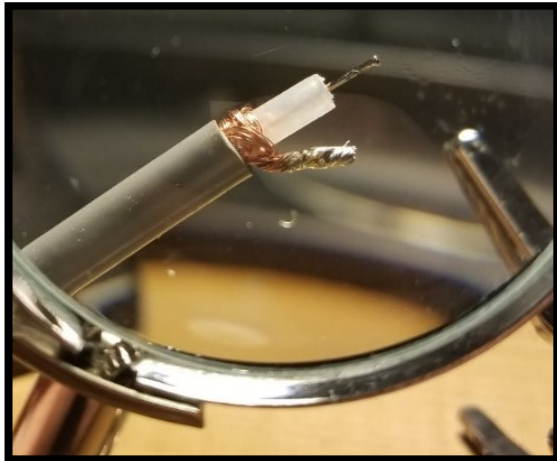


FIGURE 2.13: INNER CORE AND SHIELDING TINNED



FIGURE 2.14: BENDER ELEMENT SHOWN BEFORE BEING HOUSED (MOAT NOT CUT YET)



FIGURE 2.15: BENDER ELEMENT NESTED IN HOUSING (MOAT NOT CUT YET)



FIGURE 2.16: COMPLETELY ASSEMBLED BENDER ELEMENT WITH EPOXY COATING

2.2.3. Installation in Soil

After the benders were fully assembled and found to function properly, they were first checked for direction of polarization. This was done by connecting both sender and receiver to an oscilloscope and pushing the bender elements back and forth while watching the oscilloscope. They should be oriented so that when both are pushed in the same direction, they produce either a positive or negative voltage, and not opposites. This orientation is

marked on the housing and the steel rods are threaded through the holes in the housing, with the tips of the benders spaced at 24 cm. The seven-inch sand layer was placed first. Water is added with each lift of clay to produce a water content of approximately 25%. This was done using the following technique: knowing the average weight of air-dried soil in each 5-gallon pale and knowing the flow rate of water out of the water hose used, a specific amount of time of water flow is provided to produce a water content in the range of 24% to 26%. A water content over the liquid limit would have been undesirable as the control test would likely produce a pile with little to no load capacity. After enough soil lifts were added to produce a six-inch lift, the pile was placed into the barrel with the bender element assembly, shown in Figure 2.17.



FIGURE 2.17: ORIENTATION OF BENDERS NEXT TO PILE WITH ALIGNMENT RODS INSERTED

Lifts of clay were added continually and pushed down using gentle pressure from the end of a 4x4 lumber post to remove air-pockets. When the pile and top bender element were buried

sufficiently, the two metal rods were gently removed. The steel electrodes were hammered into place afterward and remained void of soil as the ends were pressed shut. The co-axial cable for the bender elements was threaded through a hole in the side of the barrel and connected to the DAQ. The negative lead for the power supply was connected to the negative electrodes of the system via bolts through holes in the electrodes and the positive lead was connected to the pile via a bolt through a hole which was drilled in the pile. Full schematics of the system can be seen in Figure 2.18, Figure 2.19 and Figure 2.20. Tap water was added into the negative electrodes to promote electrical contact.

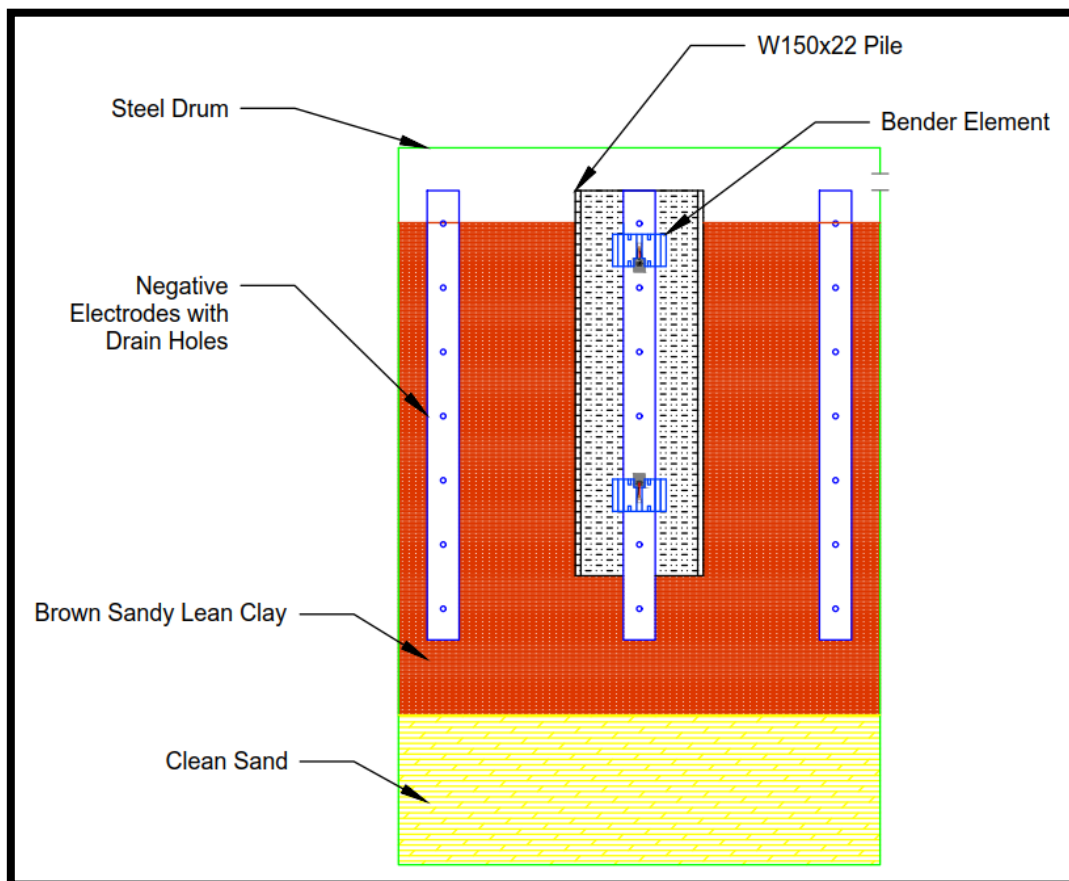


FIGURE 2.18: FOUNDATION ELEMENT, ELECTRODES AND BENDER ELEMENTS

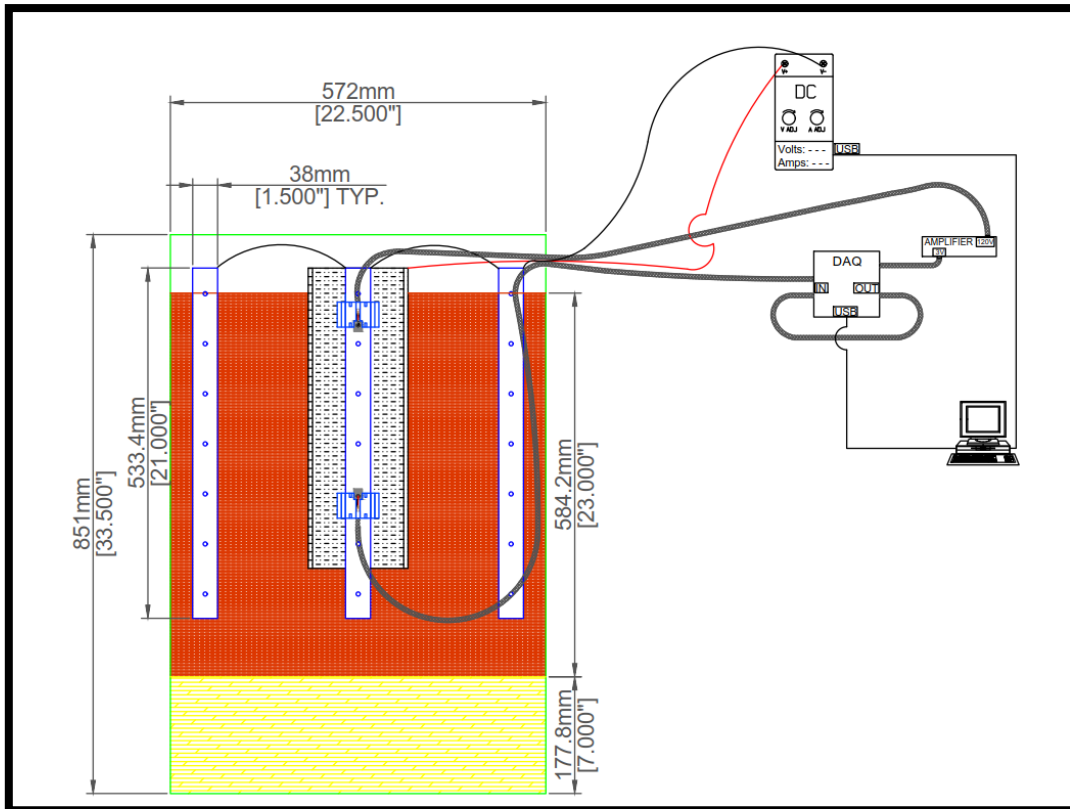


FIGURE 2.19: SECTION VIEW OF BARREL WITH DAQ AND DC POWER SUPPLY

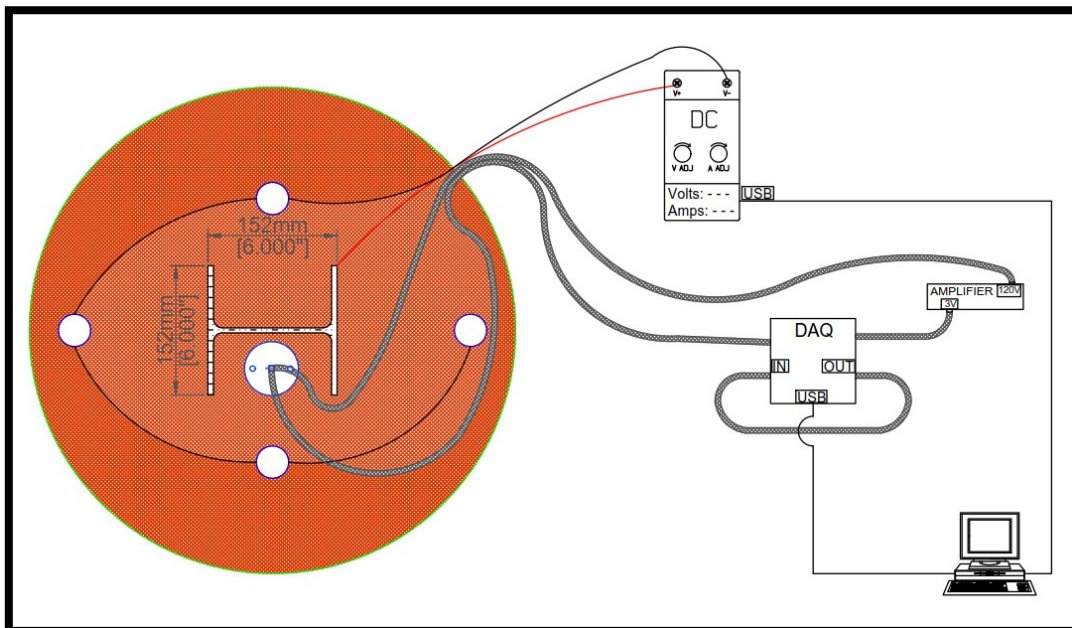


FIGURE 2.20: POWER SUPPLY AND DAQ CONNECTED TO FOUNDATION SYSTEM

2.3. Preliminary Test System

To first assess the sensitivity of the sensors they were wired to a preliminary system consisting of an oscilloscope and a waveform generator. The sensors were placed in a 5-gallon bucket,

spaced 24 centimetres apart using two $\frac{1}{4}$ inch rods, and buried in sand. An HP 33120A Arbitrary Waveform Generator was used as a signal generator for preliminary testing of the bender element system. The HP33120A can produce sine waves from 0.0001Hz to 15MHz with 12-bit resolution at 40 MHz. Internal and external triggers can be used to initialize a logarithmic or linear sweep through a select range of frequencies over a select time or output a single sine pulse. For preliminary testing and troubleshooting an HP 5464D Mixed Signal Oscilloscope was used to capture the output and received waveforms. The oscilloscope has 8-bit vertical resolution and 200M samples/ second. An analog trigger was used to detect the output from the Waveform Generator to capture the signal from both the signal generator and receiver element using the two analog inputs on the front of the unit. Cursors can be manipulated to determine the time difference between the two signals to determine shear wave velocity.

2.4. Electrokinetic Treatment System

2.4.1. Barrel, Pile and Electrodes

The barrels were donated by Mastrangelo Fuels in Thunder Bay, ON. The lids were cut off with an air-chisel and wiped clean of excess oil. The drums were 33.5 inches tall and 22.5 inches in diameter, giving them a total volume of 55 US Gallons.

The steel piles were purchased from Coastal Steel Construction. The beam came in an 8-foot section and was cut into four 18-inch segments with a bandsaw.

The electrodes were sourced from extra pipe stock in the structures laboratory at Lakehead University. The pipe stock was $1\frac{1}{4}$ inch in diameter and cut into 21-inch-long segments. It was drilled with half inch holes, spaced every $1\frac{1}{2}$ inch, alternated perpendicularly along the axis to allow excess water to drain into the electrode. The ends were pinched closed with a

hydraulic press for ease of installation and to prevent soil from filling the cavity within when they were driven into the soil.

2.4.2. Power Supply

The DC power supply used in this experimental study was an Agilent 6573A, with a rated maximum output of 2000 Watts, capable of delivering up to 60 Amps and 35 Volts. The supply supports both constant voltage and constant current modes, programmable through the front control knobs and keypad or through analog control ports at the rear using low voltage DC from an independent controller. It also has over-voltage and over-current protection, making it very easy to halt short circuits and prevent fires while the system is operating with limited supervision which is a serious risk with the systems high current potential.

To add the ability to vary the voltage or halt the voltage output completely from anywhere via internet connection, the voltage programming terminals at the rear of the unit were utilised. The voltage is controlled by varying the signal voltage from 0 to -4.24 volts to produce 0 to 35 volts.

2.4.3. DAQ and Power Control System

An Arduino was used to control the voltage output of the system using an MCP4131 Digital Potentiometer. This created the ability to create discrete steps in output voltage to produce approximately 2.91 volts out of the Arduino which when plugged into the analog programming ports in the Agilent 6573A produced 24 volts. Because the power supply requires a negative voltage, the positive and negative leads are simply exchanged.

Two sets of program code were written to control the Arduino. One sets the voltage to 2.91 Volts, the other sets the voltage to zero. When the system is to be left on, the first code is uploaded to the Arduino, and when the system is to be turned off, the second code is uploaded. The two codes can be found on page 109.

Remote Desktop Control was achieved using TeamViewer software, which enabled both Arduino and DAQ devices to be controlled from a mobile device from anywhere with internet connection. This allowed the continuous monitoring of the shear wave velocity and the ability to cease treatment at any time and from nearly anywhere.

2.4.4. Wiring and Power Monitoring

To connect the power supply to the electrodes and pile, two 8-gauge wires were connected in parallel, affixed to the electrodes and fed through PVC conduit. The choice was made such that if a short circuit took place, the wires would be capable of handling the current produced without the risk of fire, and the PVC conduit provided a protective sheath from puncture or cutting and to eliminate a tripping hazard. This can be seen in the background of Figure 2.31.

Two HP 34405A voltmeters were used to monitor both voltage and amperage throughout treatment. The voltmeter terminals were connected directly to the terminals of the DC power supply, and the ammeter was connected in series with the electrodes. They were connected to the computer via USB and programmed to take readings every 5 minutes using MATLAB. The data was stored in a CSV file with time and date stamps for each measurement.

2.5. Data Acquisition System

For full scale testing, the DT9857 made by Data Translation was programmed to act as both signal generator and receiver. Although the DT9857 can deliver 20 volts peak to peak, the input sensitivity of the amplifier required this to be limited to under 1.5 Volts peak-to-peak. The DT9857 Data Translation unit can acquire signals with 24-bit resolution and 105kHz sampling on up to 16 channels without multiplexing. The output signal was spliced back to the input before entering the amplifier to calculate the signal travel time.

A QSC model ISA 750 audio amplifier was implemented to deliver a higher voltage signal to the bender elements. The amplifier has a 35 dB gain (56.2 times the voltage), and the output voltage from the DT9857 was set to 1.5 volts to produce about 85 volts. The amplifier has both a 20kHz low-pass and 20Hz high pass filter that limited the range of frequencies that could pass through the amplifier.

MATLAB was used to create the series of commands to both control the data acquisition system and process and store the collected data. Because shear wave velocity is dependent on a relationship between the distance between sender and receiver and signal wavelength, a series of frequencies are selected. Not only this, the benders themselves have a specific bandwidth for which they are effective. The distance between the elements was considered to be constant. Although it is possible that some settlement may occur, having such a large distance between the elements reduces the possibility for changes to affect the outcome of shear wave velocity.

Other researchers have used both sine pulse and sine sweep for purposes of shear wave velocity analysis, therefore the two signal types were used [29, 30, 35, 36]. To mitigate issues related to data size, the stored signals are trimmed in length until only the bulk of the received signal is stored, with no excess data being kept. The original, unfiltered signals are stored as tab delimited .txt files to allow for changes to filtering to be made later without compromising signal fidelity. In this study, only the sine pulses were analysed to determine shear wave velocity, however the swept signal data was kept for future studies.

Due to the presence of a DC electric field and the presence of the conductive steel drum and steel pile near the sensors, an elevated level of noise was present. The Agilent 6473A DC power supply has a small amount of AC ripple noise that presented itself as a 60Hz, 80Hz and

120Hz noise to the bender elements. This noise necessitated the need for detrending and filtering. To allow for better peak detection the signal was also smoothed.

A sample of signal coming from the receiving element is shown in Figure 2.21. Detrending was accomplished by fitting an 8th order polyline to the DC baseline found in the original signal (Figure 2.22), and then subtracting this baseline from the original signal, shown in Figure 2.23.

The Post-Baselined signal is shown in Figure 2.24. Next the signal was smoothed using a 3rd order, 61 frame Savitsky-Golay Filter, rendering the signal in Figure 2.25.

After detrending and smoothing the signal was filtered using a 2nd order Butterworth band stop filter designed using MATLABs Filter Design and Analysis toolbox with half-stops at 105Hz and 135Hz as most of the noise was at 120Hz, with the final post-processed result being shown in Figure 2.26.

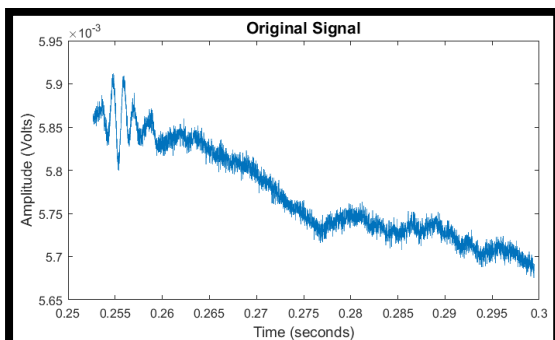


FIGURE 2.21: RAW SHEAR WAVE RECEIVED BY DAQ

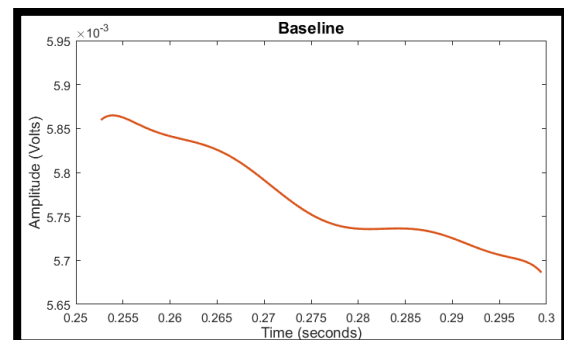


FIGURE 2.22: BASELINE OF SIGNAL

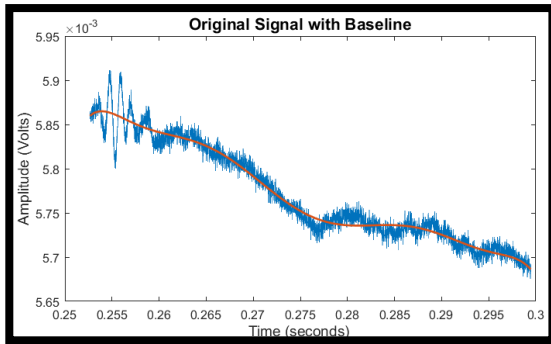


FIGURE 2.23: BASELINE OVERLYING ORIGINAL SIGNAL

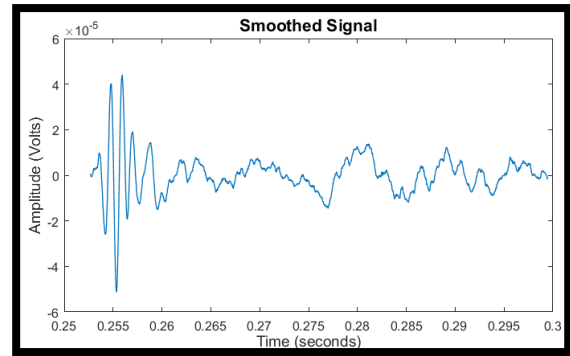


FIGURE 2.25: SIGNAL POST-SMOOTHING AND BASELINING

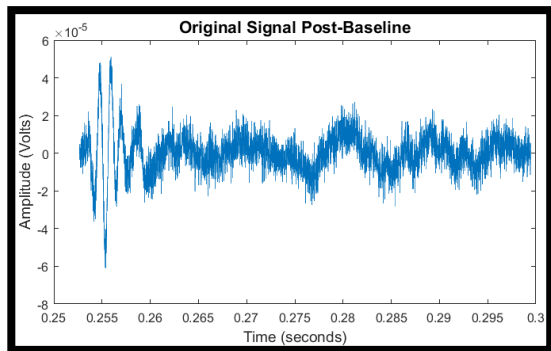


FIGURE 2.24: SIGNAL POST-BASELINE REMOVAL

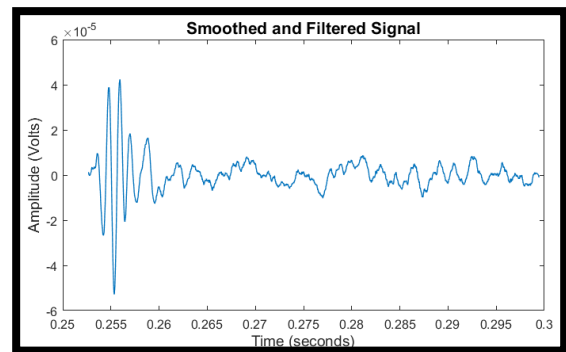


FIGURE 2.26: SIGNAL POST-FILTER, SMOOTHING AND BASELINING

Once the signal had been processed sufficiently, MATLAB peak detection was used to find the three tallest peaks and log their time. The three peaks (labelled in further figures as Tallest Signal Peak, 2nd Signal Peak and 3rd Signal Peak) are shown in Figure 2.27.

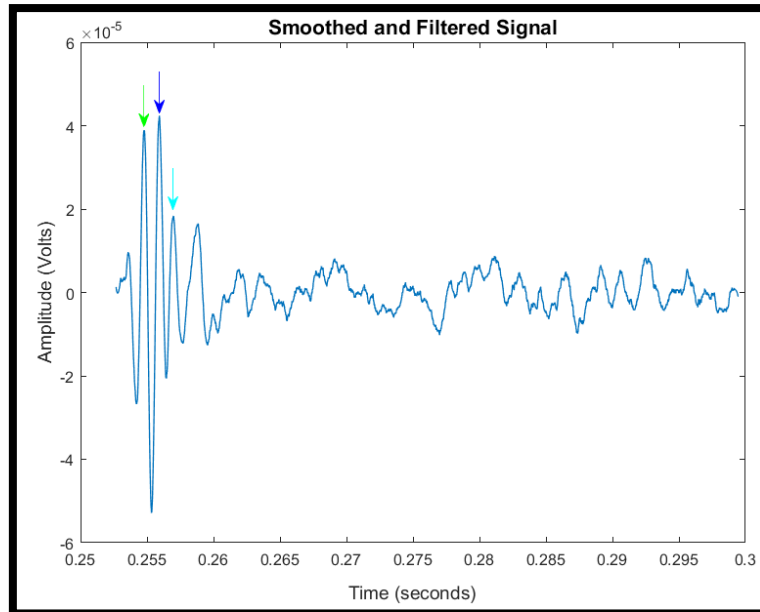


FIGURE 2.27: POST-PROCESSED SIGNAL WITH THREE PEAKS SELECTED FOR WAVE VELOCITY DETERMINATION

The peak to peak time difference, dt in Figure 2.28, is calculated by subtracting the time to peak of the sent wave from that of the peaks in the received wave. Shear wave velocity is calculated by taking the distance between elements (0.24m) and dividing it by the difference in time between peaks, dt . In the example shown, MATLAB is observing that the second tallest peak is giving the fastest velocity. Multiple peaks are used to better identify the shear wave velocity even when faced with changes in shear wave response. In this example the shear wave velocity would be 129.2 m/s

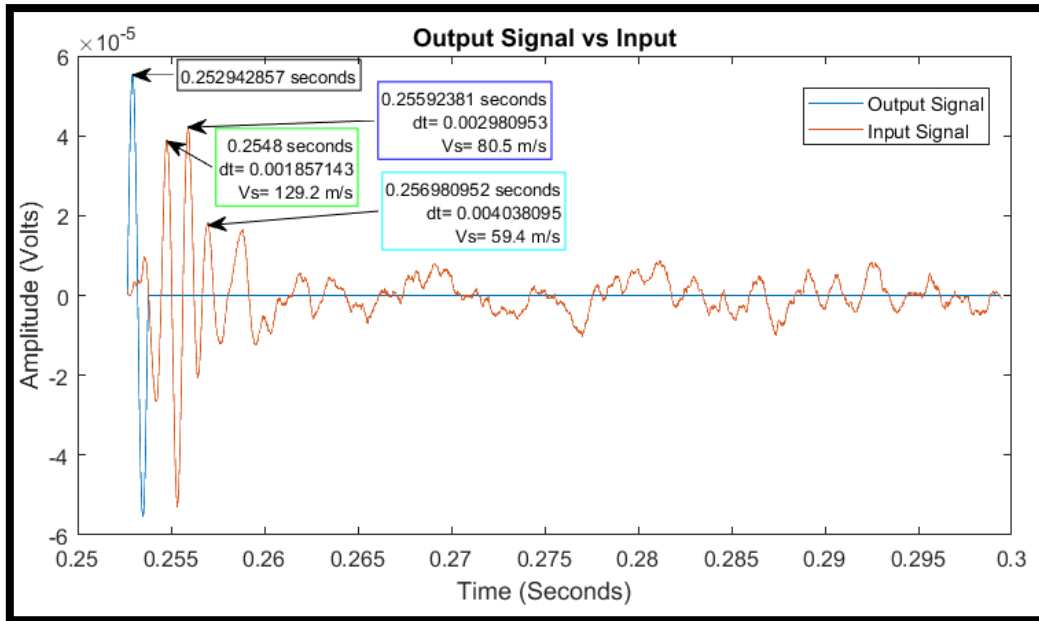


FIGURE 2.28: PEAK TO PEAK SHEAR WAVE VELOCITY DETERMINATION

Shear wave velocity is also calculated using the cross-correlation function. The signals (functions) are multiplied together stepwise. The two functions are first normalized to each other as their amplitudes are drastically different. One signal is delayed relative to the other. The delay which produces the highest correlation appears as a peak in the cross-correlation function, shown in Figure 2.29. If the sent signal is delayed by a value equal to that of the time of the peak in the cross-correlation function, the two signals will overlay each other near-seamlessly, shown in Figure 2.30. To determine the shear wave velocity using the cross-correlation function, the distance between bender elements is divided by the time of the tallest peak in the cross-correlation function. Comparing the value of 130.5 m/s for CCF to that of the peak-to-peak technique of 129.2 m/s, the values are within a 1% difference of each other, which is in high agreement. It was found that the cross-correlation technique performed best when the sent signal and received signal had the same principle frequency so that the CCF was able to determine a high level of correlation to one specific oscillation in the

received wave. Shown below is an example of how shear wave velocity was determined using the CCF results.

$$\frac{0.24m}{0.001838095238095 \text{ seconds}} = 130.5 \text{ m/s}$$

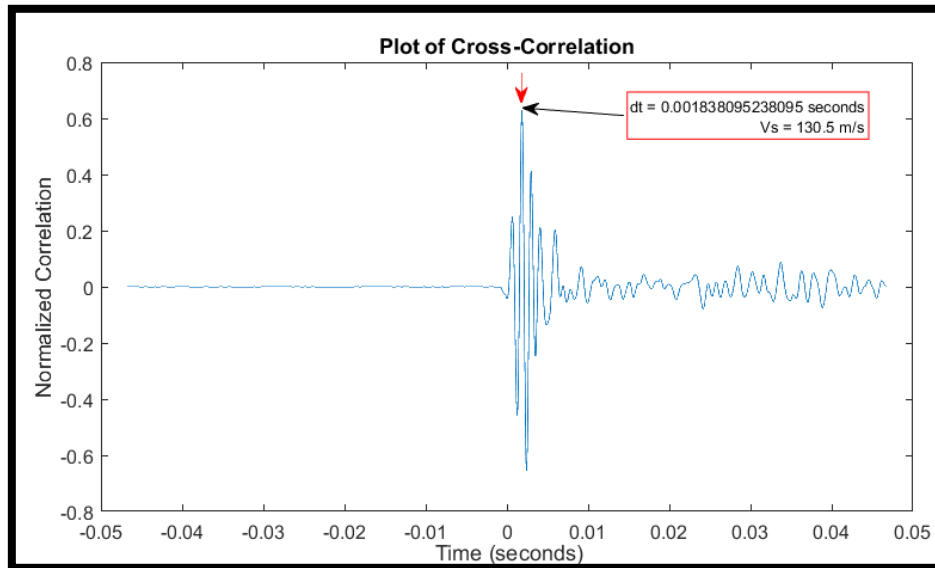


FIGURE 2.29: CROSS-CORRELATION AND PEAK FOR WAVE VELOCITY DETERMINATION

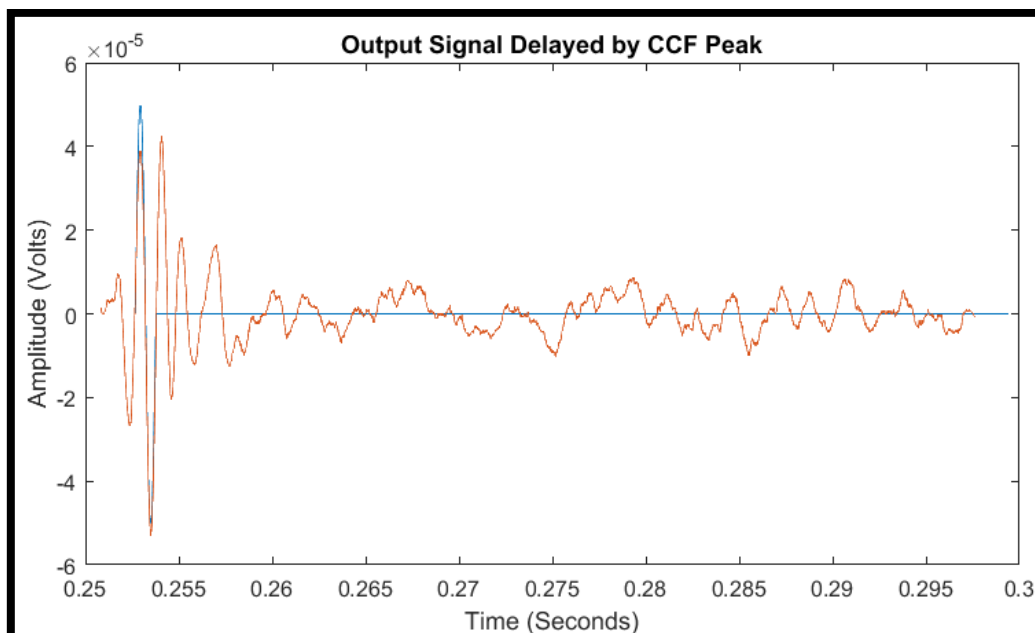


FIGURE 2.30: OUTPUT SIGNAL OVERLAID ATOP RECEIVED WAVE AT CCF DELAY

2.6. Pile Load Test

2.6.1. Loading System

An ENERPAC RR5013 hydraulic cylinder with a 13-inch stroke was secured to the loading rig above the barrel with a ratchet strap. The cylinder was powered by a hand-operated, double-action hydraulic pump made by SPX-PowerTeam. An ARTECH Industries 20210-2k (Figure 2.33) load cell was used to monitor total load placed on the pile during loading. It was placed atop a steel plate which rested on the pile, and under the hydraulic cylinder. Two TRS-100 position transducers (Figure 2.34) were used to monitor pile settlement during loading and were held to the hydraulic cylinder during loading using magnetic gage holders. The tips of the transducers were placed on two opposite corners of the pile. Using StrainSmart software, a model 5100A scanner made by Vishay Instruments was used to power and collect data from the load cells and displacement gauges. Data was exported into Excel files.



FIGURE 2.31: BARREL 3 WITH LOADING RIG ABOVE PILE WITH WIRING AND CONDUIT STILL IN PLACE



FIGURE 2.32: PILE READY FOR LOADING WITH DISPLACEMENT AND STRAIN GAGES IN PLACE



FIGURE 2.33: ARTECH 20210-2K LOAD CELL



FIGURE 2.34: TRS-100 POSITION TRANSDUCER

2.6.2. Loading Procedure

The pile was loaded 14 days after treatment ceased and were loaded in 50lb increments which was held for a minimum of 4 minutes until settlement had ceased for a maximum of 15 minutes, in accordance with ASTM D1143-07 [63]. Due to the nature of the hand pumped loading system, as the pile failed, and strain rates increased dramatically, keeping the load steady became increasingly difficult. When this occurred, loading was halted, and the pile was considered to have failed completely.



FIGURE 2.35: BARRELS WITH LOADING FRAME ABOVE AND CONTROL CENTRE IN FRONT

2.7. Shear Vane Tests

The purpose of these tests was to monitor the extent of soil stiffening, give opportunity to observe the relationship between shear strength and water content after treatment, and observe the extent of soil drying caused by electrokinetics.



FIGURE 2.37: EDECO PILCON SHEAR VANE HAND TESTER

2.8. X-Ray Diffraction Spectrometry

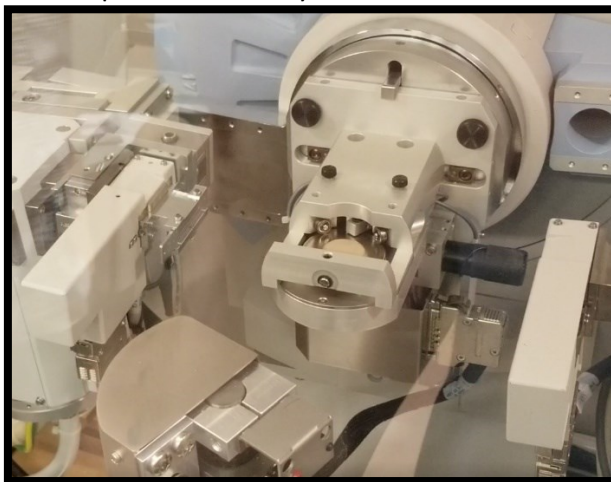


FIGURE 2.38: SAMPLE IN XRD SPECTROSCOPE

X-Ray diffraction (XRD) was used initially to help determine what, if any, new compounds were formed due to the electrokinetic treatment. As the electrode and pile were made from steel, new compounds consisting of iron were expected to have formed after the treatment. The process begins with drying samples and lightly grinding them. The samples are then

loaded into plates to be loaded into the XRD spectroscope. The entire process of scanning the samples takes about 15 minutes per sample. Figure 2.38 shows the XRD spectroscope and plate that was loaded with sample and inserted into the spectroscope. Once the samples are scanned, the information is recorded in x-ray counts against 2-theta. All minerals and compounds have a specific crystal structure that will refract the x-rays at a specific angle of attack. The spectrographs of known compounds are recorded in a database and the spectrograph from a scanned sample is compared against the known spectrographs in the database to determine what minerals and compounds are present.

2.9. Scanning Electron Microscope and X-Ray Energy Dispersive Spectrometry

A Hitachi SU-70 scanning electron microscope was used to perform elemental analysis of clay particles to hopefully discover if any new compounds had been formed. Samples were dried and sieved through a No.200 sieve. A small pedestal is covered in fresh carbon paste and the samples are dusted on top. The samples are then coated in carbon using an Edwards Auto 306 Vacuum Coater to render them conductive. With the samples ready, they are placed inside the scanning electron microscope and analysed using x-ray energy dispersive spectrometry to determine what changes had occurred to the muscovite clay.

Chapter 3 – Results and Discussion

The results shown below were collected over the course of a year. The most difficult part of this research would be the bender elements as this portion was by far the most under-researched and standards and protocols do not exist as they do for all the other tests. Implementing the bender elements into the treatment process also proved incredibly troublesome. The initial design of the bender housing lacked the moat portion that created a longer path for water intrusion and did not include the step of oxidizing the HDPE to facilitate bonding of the epoxy. Because of this, some of the first bender elements developed a short circuit soon after treatment commenced. Even when a short did not develop due to water intrusion, there was a 50% chance (half the sensors failed) that the sensors would become defective at the onset or termination of treatment due to the creation and destruction of the electric field. An example of this is seen in Figure 3.15 at about 160 hours when the signal becomes unrecognizable by the software. Knowing that piezo-ceramic coatings are made using high strength DC electric fields under high temperature, it is possible that when the DC electric field in the soil is created it has the potential to permanently alter the polarization of the plates. In some instances, the sensitivity of the sensors was affected for several hours and only later recovered, as can be seen in the first few hours of treatment in Figure 3.15.

3.1. Electric Field and Power Consumption

Figure 3.1, Figure 3.2, Figure 3.3 show a static simulation of voltage potential, electric field strength and current density, of a barrel undergoing treatment using QuickField, an electric field simulation software which operates using finite element analysis [65]. A preliminary modelling with Quickfield was carried out to determine the appropriate applied voltage, electrode distribution and bender element location. The model showed the voltage potential

to be symmetrical around the pile. Examination of current density and electric field strength reveals that there was a large disparity between the current flowing from the web versus that flowing from the faces and edges of the flanges. This is mainly due to the distance between the electrode faces as electricity always favours the path of least resistance. This indicated that the web would be the section of the pile receiving the slowest treatment, therefore the bender elements were placed in this area.

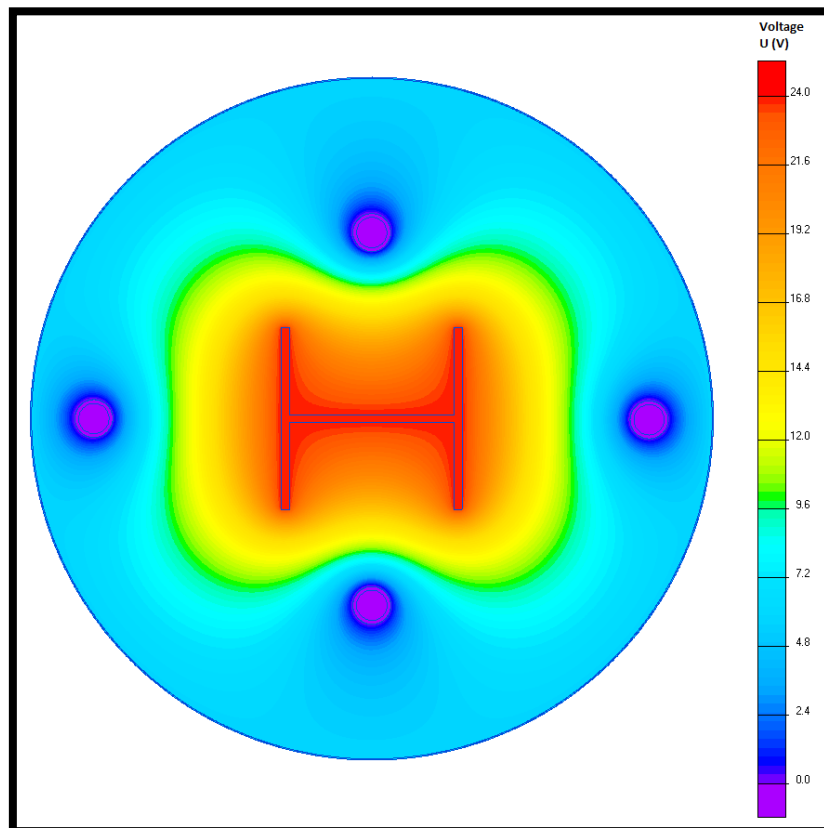


FIGURE 3.1: VOLTAGE POTENTIAL OF BARREL UNDERGOING TREATMENT

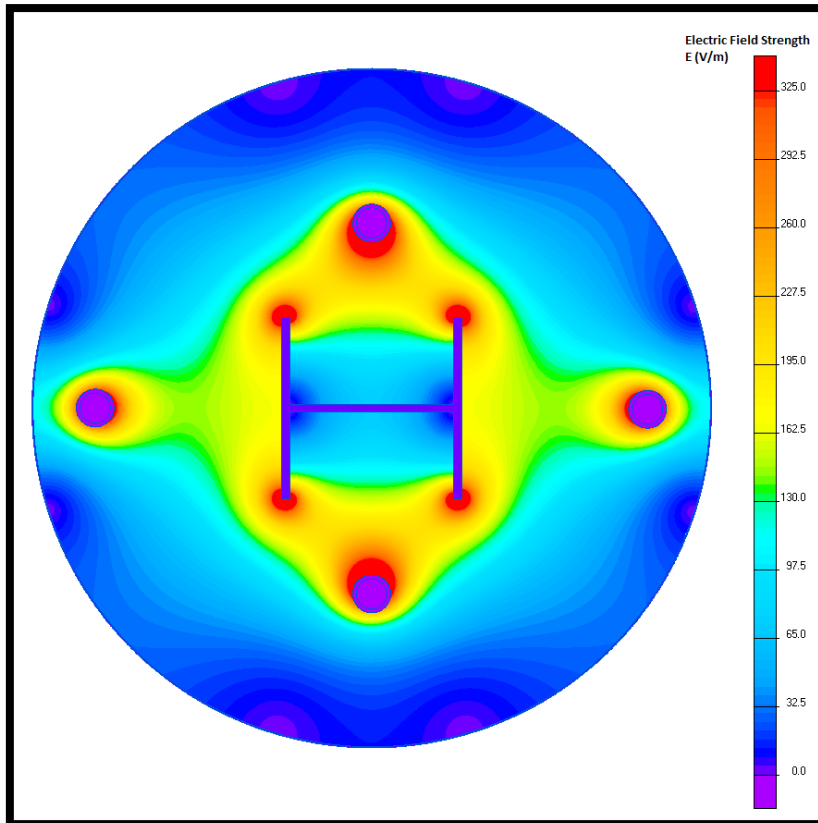


FIGURE 3.2: ELECTRIC FIELD STRENGTH OF BARREL UNDERGOING TREATMENT

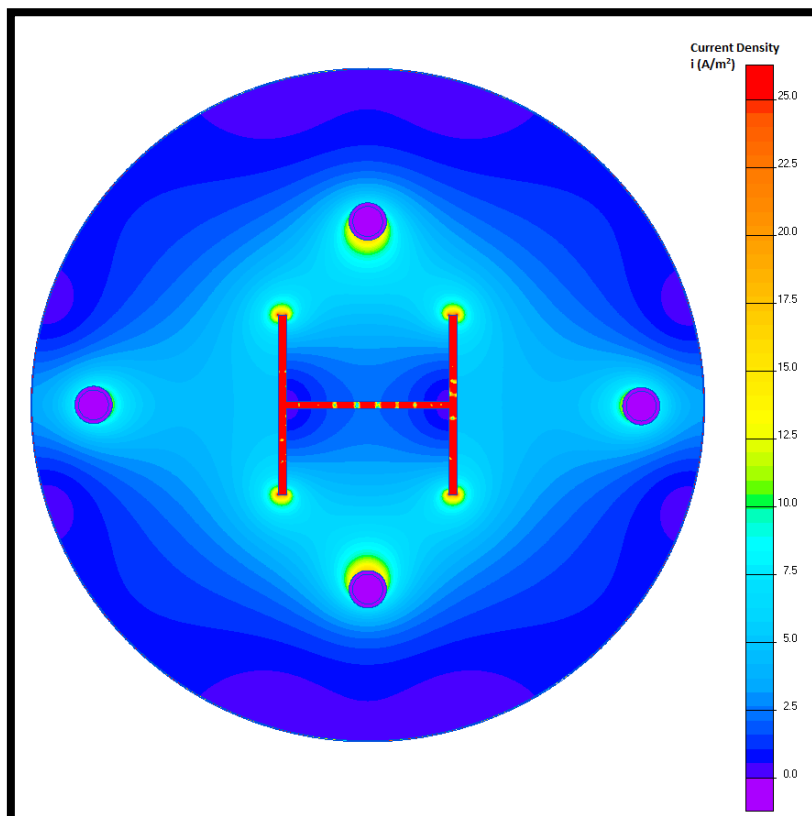


FIGURE 3.3: CURRENT DENSITY OF BARREL UNDERGOING TREATMENT

Figure 3.4 and Figure 3.5 show the current draw and power consumption against time. By multiplying the amperage by time and voltage, the total energy used in watt-hours (Wh) is found. The csv file output by MATLAB takes measurements every 5 minutes, therefore the voltage is multiplied by the current, then multiplied by 5/60 hours, and then each of these 5-minute segments is added together to determine the total energy used during treatment. For example:

$$Energy = V * A * t$$

$$Voltage = 24 V$$

$$Amperage = 2.4 Amps$$

$$Energy = 24V * 2.4 A * \frac{5}{60} Hours$$

$$E = 4.8 Wh \text{ was consumed in a 5 minute period}$$

The power consumption curves are an important piece of data as they display the actual amount of electricity that was required to treat the soil. The direct relationship dictating the current that can pass through the soil is given by Ohms law. As the soil is dried through electrokinetics, either by the heat generated from the process or by the actual electrokinetic flow from anode to cathode, the electrical conductivity and areas of soil-pile contact are quickly reduced. Observing Figure 3.4 and Figure 3.5, it can be seen that Piles 1 and 4 had very similar power consumption curves, while piles 2 and 3 exhibited a steep drop off in current draw relatively quickly. Major differences between the power curves is mainly attributed to the availability of free pore fluid.

TABLE 3.1: SUMMARY OF TREATMENT TIME, POWER CONSUMED AND FAILURE LOAD

Treatment Time (Hours)	Power Consumed (kWh)	Failure Load (lb)
170	5.69	550
55	1.17	350
115	0.8	250
100	3.76	600
0	0	200

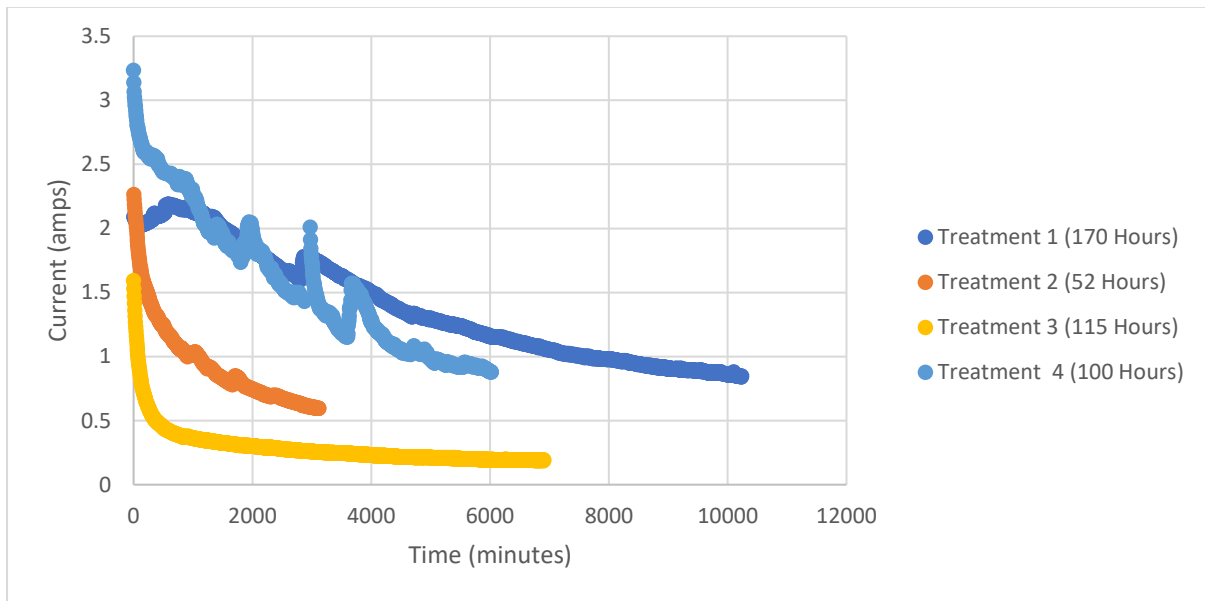


FIGURE 3.4: AMPERAGE OVER TIME UNDER CONSTANT VOLTAGE FOR ALL PILES

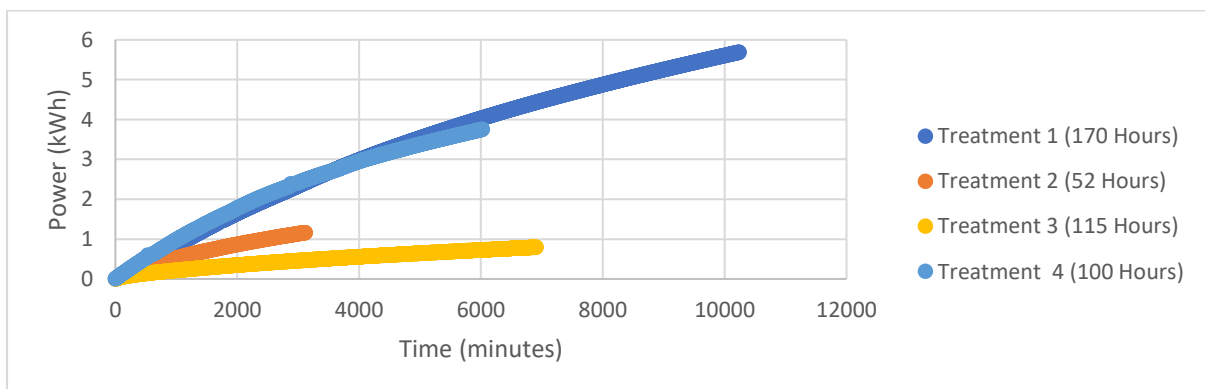


FIGURE 3.5: CUMULATIVE POWER CONSUMPTION FOR ALL TREATMENTS

3.2. Shear Wave Velocity

The plots of shear wave velocity in Figure 3.6 to Figure 3.19 have been annotated to indicate the point of treatment commencement and termination and the shear wave velocities at the time of power termination, as well as the final values recorded due to shear wave velocity rebound. As treatment commences shear wave velocity increases rapidly under the influence of electrokinetics. In addition, the overall response of the shear wave travelling through the soil changes which is shown by the change in peak amplitude throughout treatment, seen in Figure 3.7 and Figure 3.15. When examining the shear wave velocity curves, note that order of amplitude (tallest peak, 2nd tallest, 3rd) changes over time. In previous research, the shear wave arrival was determined by visual or case by case analysis. Because there were twenty shear waves sent through the soil every hour for upwards of two-hundred hours, it would have been unfeasible to analyse over four-thousand individual shear wave plots per barrel by hand, not to mention fraught with bias. To lessen the time of analysis and increase accuracy, MATLAB code was tailored to analyse the time of the three tallest peaks. Three peaks were chosen because most shear waves in these tests have 3 major peaks. Under the condition that the first arriving peak was not the tallest, the MATLAB code would still record it amongst the plot and prevent discontinuities that would be present otherwise. In addition to this, the peak in the cross-correlation between the sent and received signal was included.

Although the plots of shear wave velocity against treatment time remain quite stable, when comparing these plots across various frequencies it becomes clear that there is no definitive answer as to what the shear wave velocity is.

It can also be seen in these plots that higher frequencies yield crisper results as the soil stiffens over the course of treatment, however early on the shear waves are impeded greatly at those higher frequencies, seen in Figure 3.19.

3.2.1. Barrel 1 – Shear Wave Velocity vs Time

The six plots below (Figure 3.6 to Figure 3.11) show the changes in shear wave velocity that occurred due to treatment. The first figure shows the data obtained when a 400 Hz pulse was supplied to the bender elements, which was the lowest frequency that rendered useable results. The last figure in the series shows the shear wave velocity against time for a frequency of 2500 Hz. More plots were saved for higher frequencies (up to 5000 Hz), yet the highest frequency to render useable results was 2500 Hz for this round of treatment. A glitch in programming (csv file was open, therefore program could not save data to file) caused a lapse in monitoring to occur about 20 hours into the treatment, this is denoted as “Power Failure” in the figures below. Shear wave velocity peaked at about 55 hours, which was the treatment time that was used in the second barrel, and reached plateau at 100 hours, becoming stable at 115 hours which was selected as the treatment time for the third barrel. After treatment was terminated, the shear wave velocity dropped slowly over the course of 50 hours by about 5%-10% depending on the frequency used. It is possible that the presence of the electric field was actively reducing the pore water pressure near the anode by the induction of fluid flow away from the anode and that this gradual decrease in shear wave velocity was due to the pore fluid pressure returning to equilibrium. The trend of different shear wave velocity’s with different frequency waves agrees well with research published concerned with shear wave velocity determination and wave propagation in porous mediums [30, 55, 45, 36, 35] .

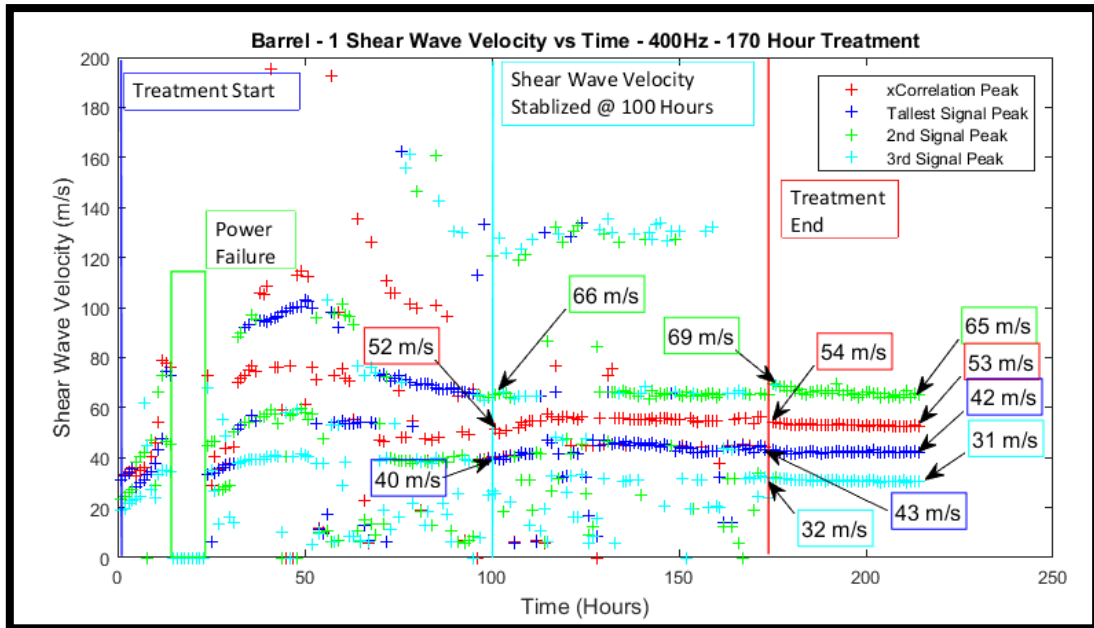


FIGURE 3.6: BARREL 1 SHEAR WAVE VELOCITY, 400HZ OUTPUT, TREATED 170 HOURS

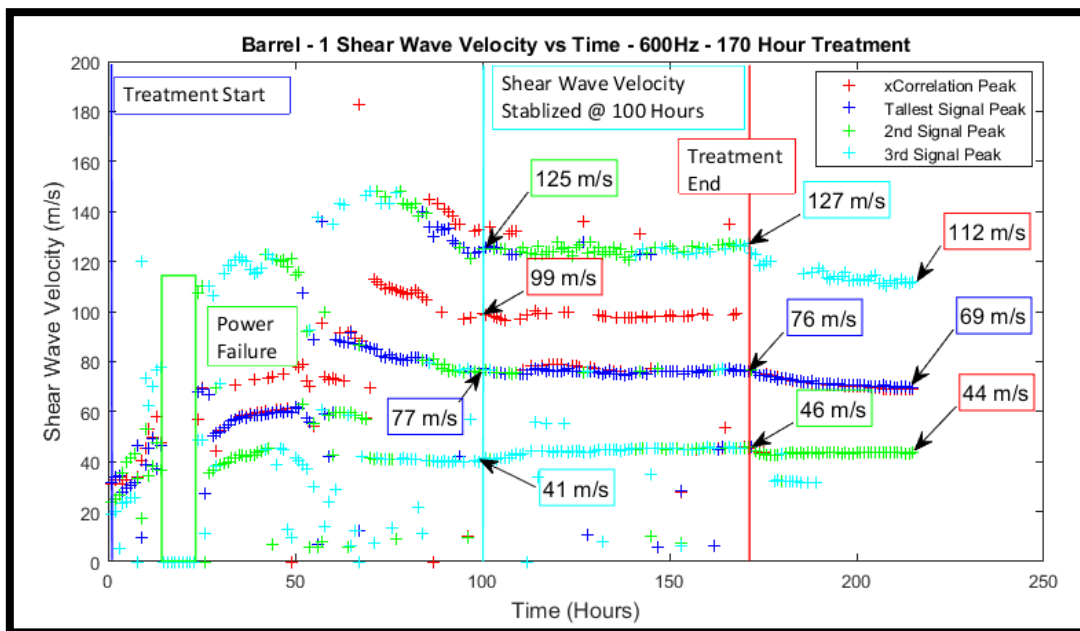


FIGURE 3.7: BARREL 1 SHEAR WAVE VELOCITY, 600HZ OUTPUT, TREATED 170 HOURS

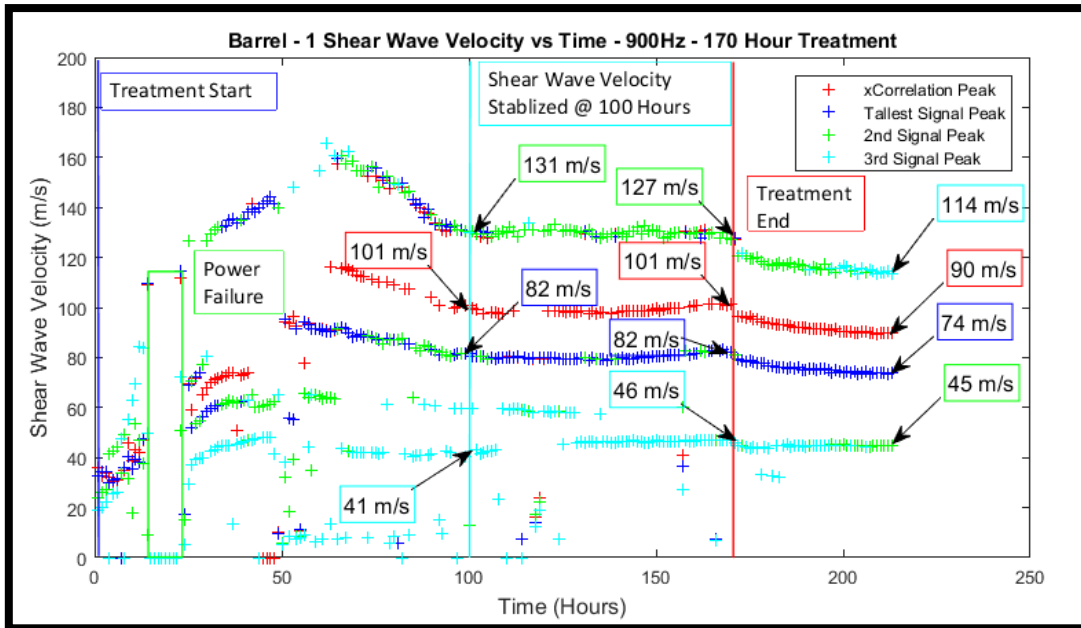


FIGURE 3.8: BARREL 1 SHEAR WAVE VELOCITY, 900HZ OUTPUT, TREATED 170 HOURS

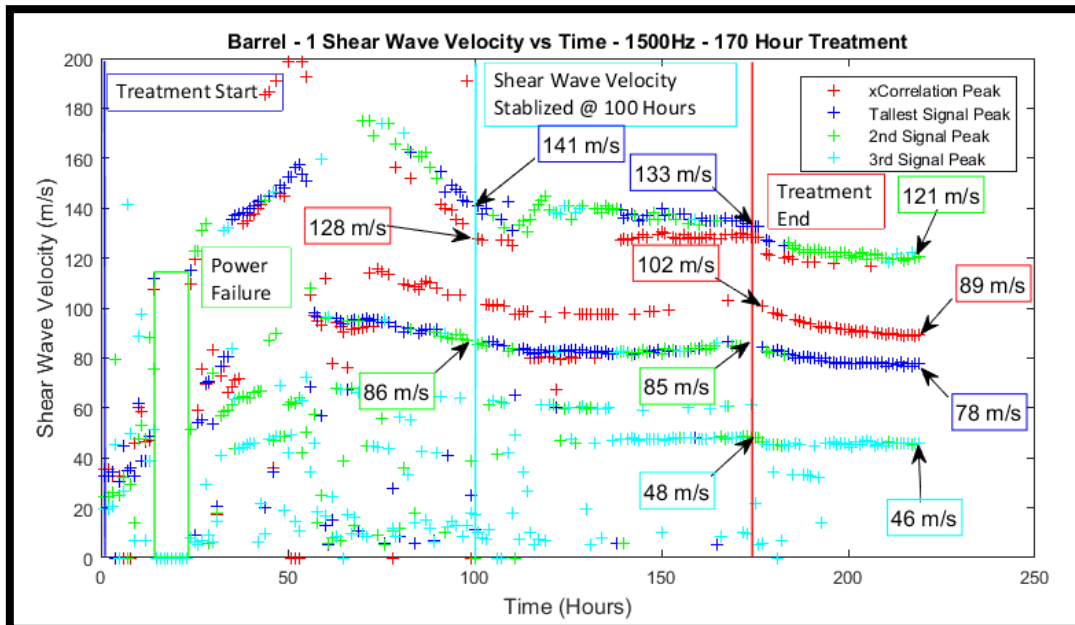


FIGURE 3.9: BARREL 1 SHEAR WAVE VELOCITY, 1500HZ OUTPUT, TREATED 170 HOURS

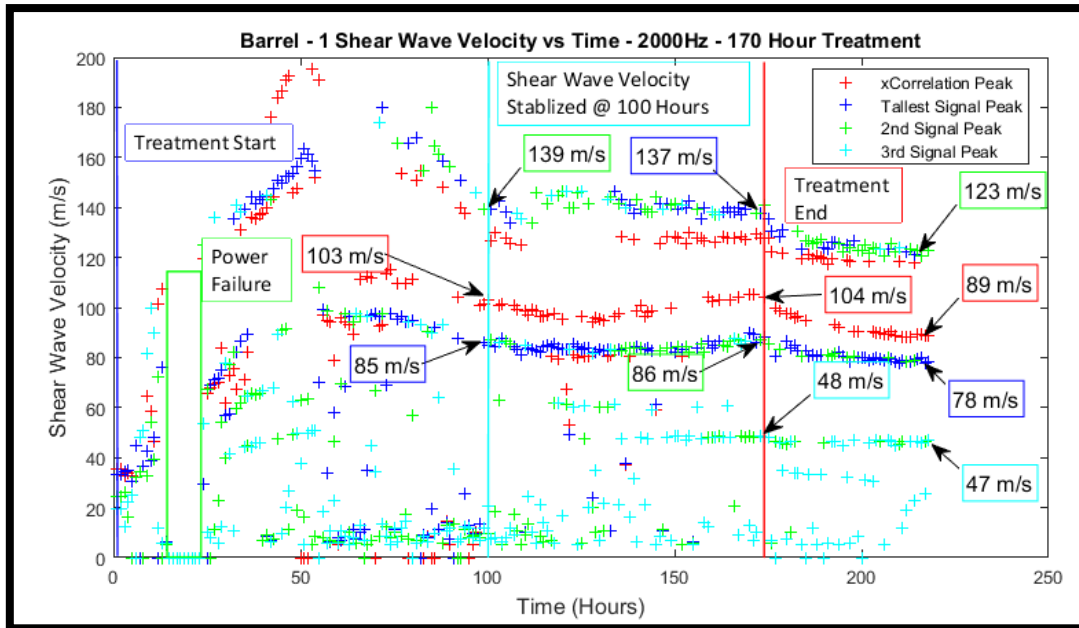


FIGURE 3.10: BARREL 1 SHEAR WAVE VELOCITY, 2000HZ OUTPUT, TREATED 170 HOURS

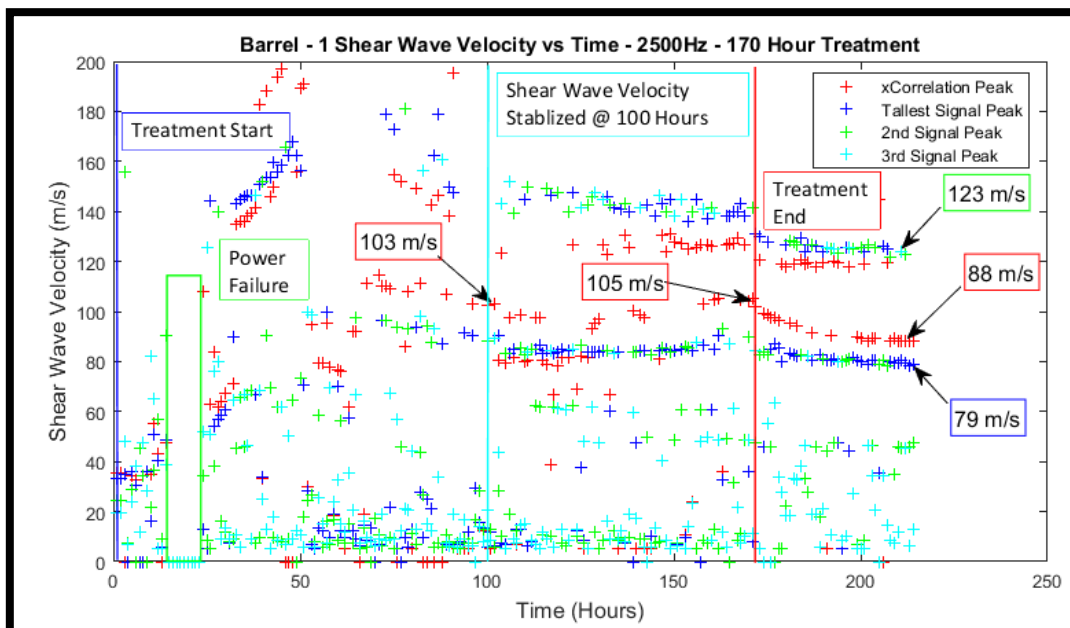


FIGURE 3.11: BARREL 1 SHEAR WAVE VELOCITY, 2500HZ OUTPUT, TREATED 170 HOURS

3.2.2. Barrel 2 – Shear Wave Velocity vs Time

Figure 3.12 shows the evolution of shear wave velocity over time for barrel 2 undergoing no treatment. As the soil settles from being remoulded, shear wave velocity slowly increases. No shear wave velocity vs time plot is available for barrel 2 during treatment as the bender elements failed at the onset of treatment. Because of the way MATLAB chooses peaks for the

cross correlation (reads absolute maximum, not maximum positive value), it appears as though shear wave velocity starts very high. This is not the case and is MATLAB taking the lowest correlation which is essentially the peak if the received signal were inverted.

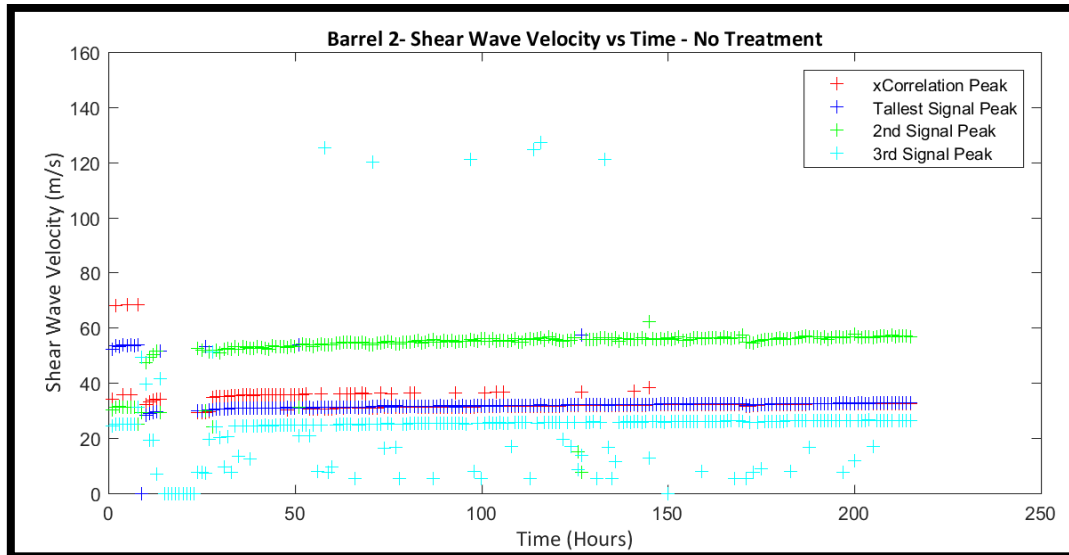


FIGURE 3.12: BARREL 2 SHEAR WAVE VELOCITY, 600HZ OUTPUT, NO TREATMENT

3.2.3. Barrel 3 – Shear Wave Velocity vs Time

Figure 3.13 shows shear wave velocity over time for barrel 3. Like Figure 3.12, miniscule increases in shear wave velocity occur slowly over time. Also like barrel 2, the bender elements were rendered inoperable at the onset of the DC electric field.

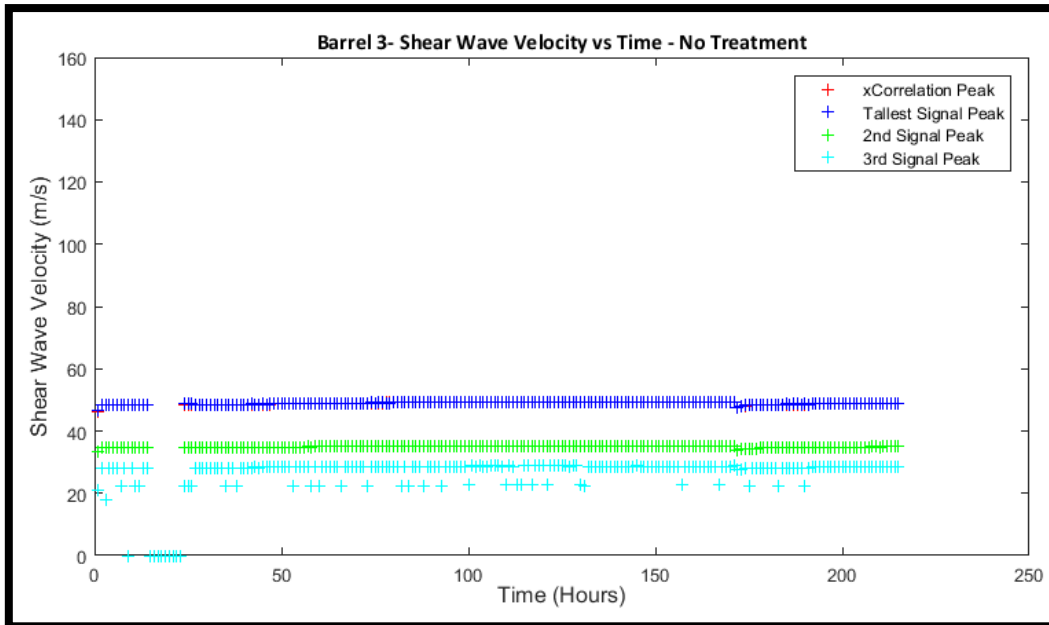


FIGURE 3.13: BARREL 3 SHEAR WAVE VELOCITY, 600HZ OUTPUT, NO TREATMENT

3.2.4. Barrel 4 – Shear Wave Velocity vs Time

Figure 3.14 to Figure 3.19 show shear wave velocity plotted against time. The shapes of the plots vary with frequency, with 600 and 900 Hz plots yielding crisp results which were, in real time, used to determine the completion time of the treatment when the plots began to plateau. Unlike the plots associated with barrel 1 the shear wave velocity fell greatly, upwards of 15% in 15 hours. Although the bender elements failed at the termination of treatment (as can be seen by the disarray of the plot after 160 hours), it can only be assumed that the dropping of shear wave velocity would have reached plateau at some point after the treatment much like it did in barrel 1. The higher frequencies did not render crisp curves until approximately half way through the treatment, meaning that the upper frequency limit of the soil and its frequency response changed due to the electrokinetic treatment.

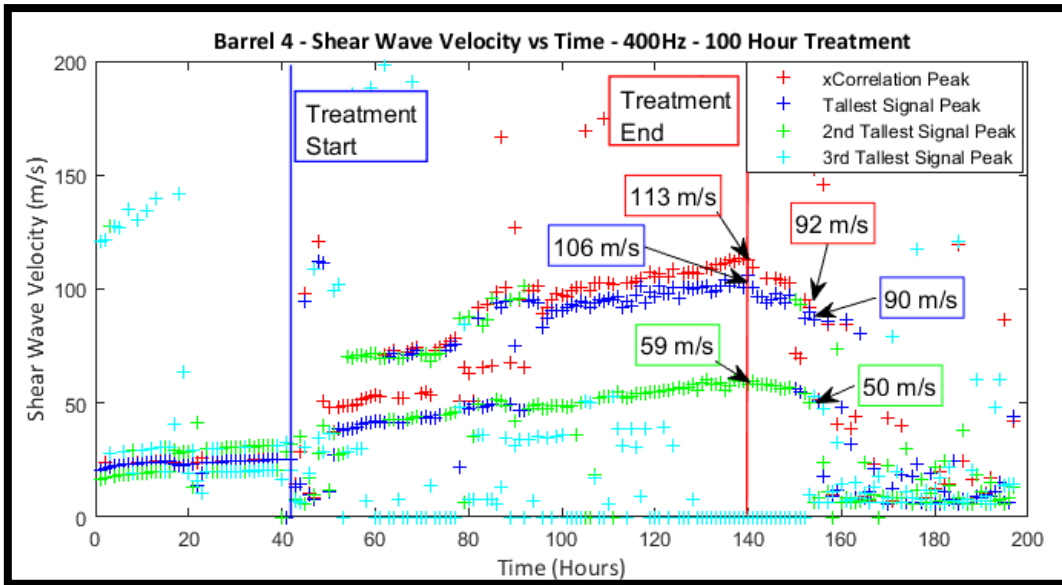


FIGURE 3.14: BARREL 4 SHEAR WAVE VELOCITY, 400Hz OUTPUT, 100 HOURS TREATMENT

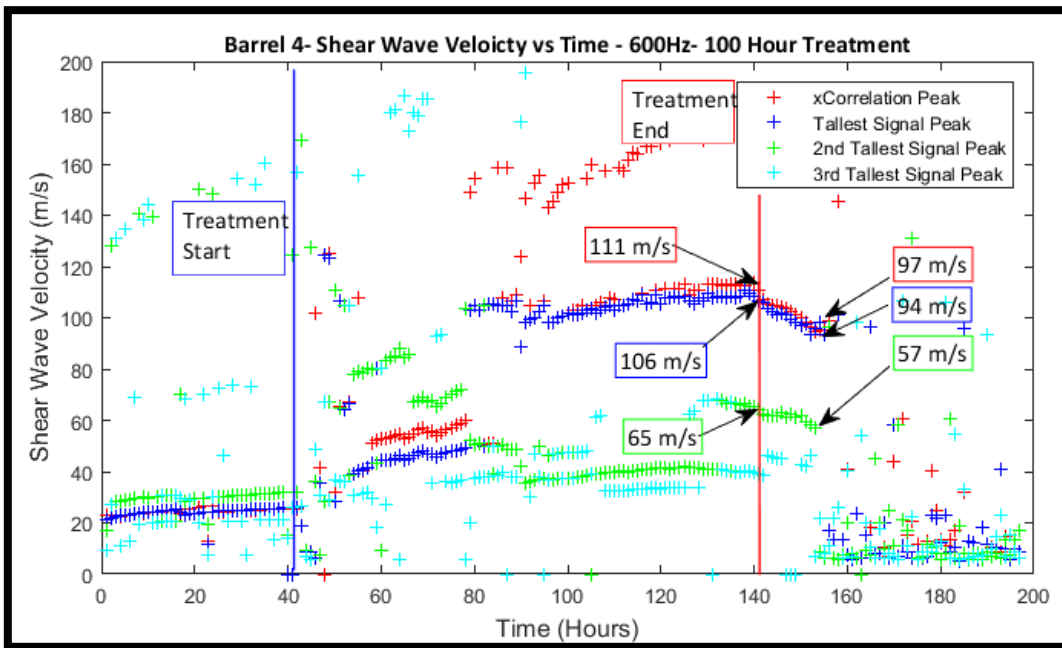


FIGURE 3.15: BARREL 4 SHEAR WAVE VELOCITY, 600Hz OUTPUT, 100 HOURS TREATMENT

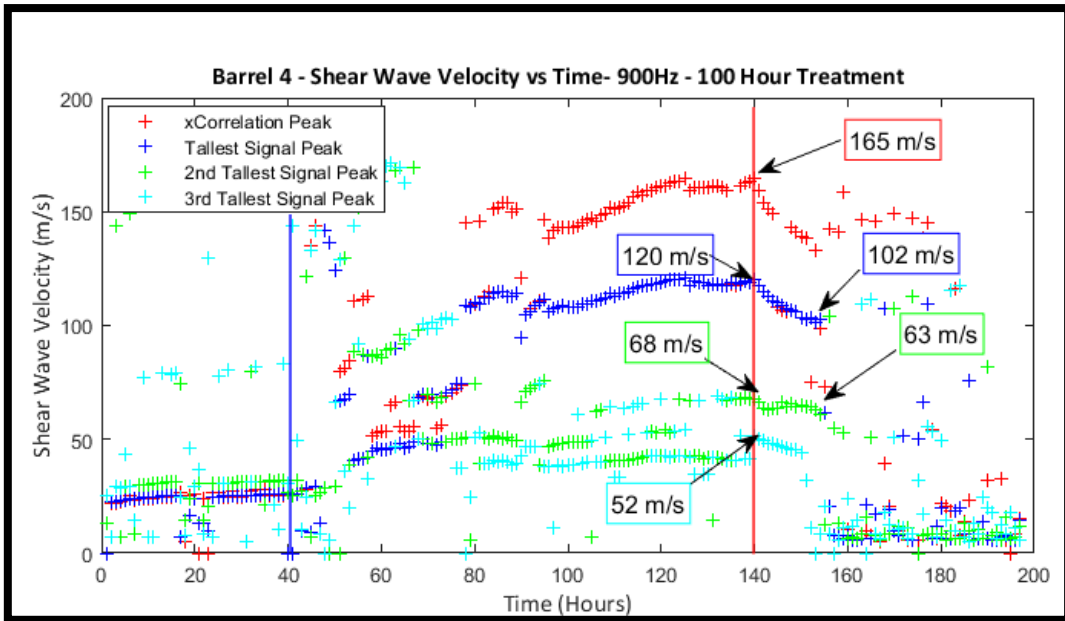


FIGURE 3.16: BARREL 4 SHEAR WAVE VELOCITY, 900HZ OUTPUT, 100 HOURS TREATMENT

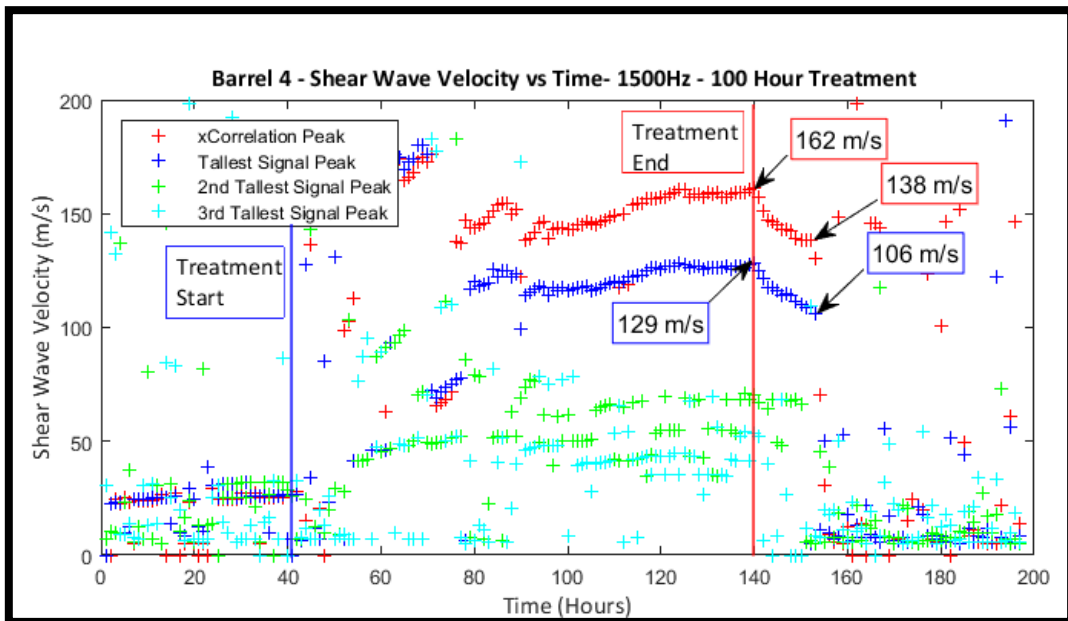


FIGURE 3.17: BARREL 4 SHEAR WAVE VELOCITY, 1500HZ OUTPUT, 100 HOURS TREATMENT

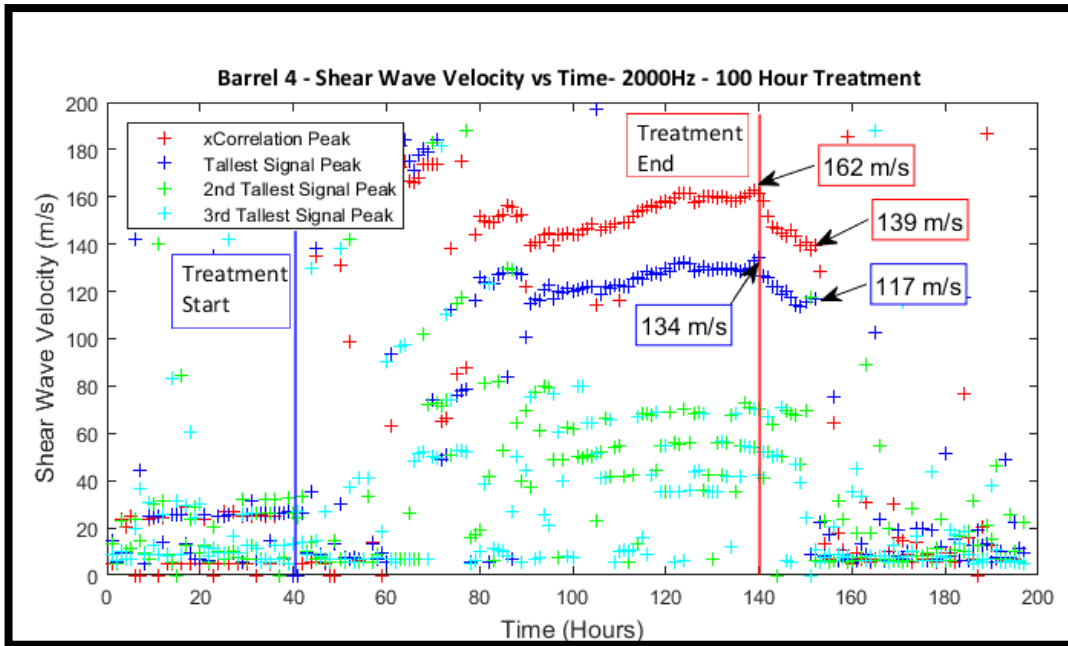


FIGURE 3.18: BARREL 4 SHEAR WAVE VELOCITY, 2000HZ OUTPUT, 100 HOURS TREATMENT

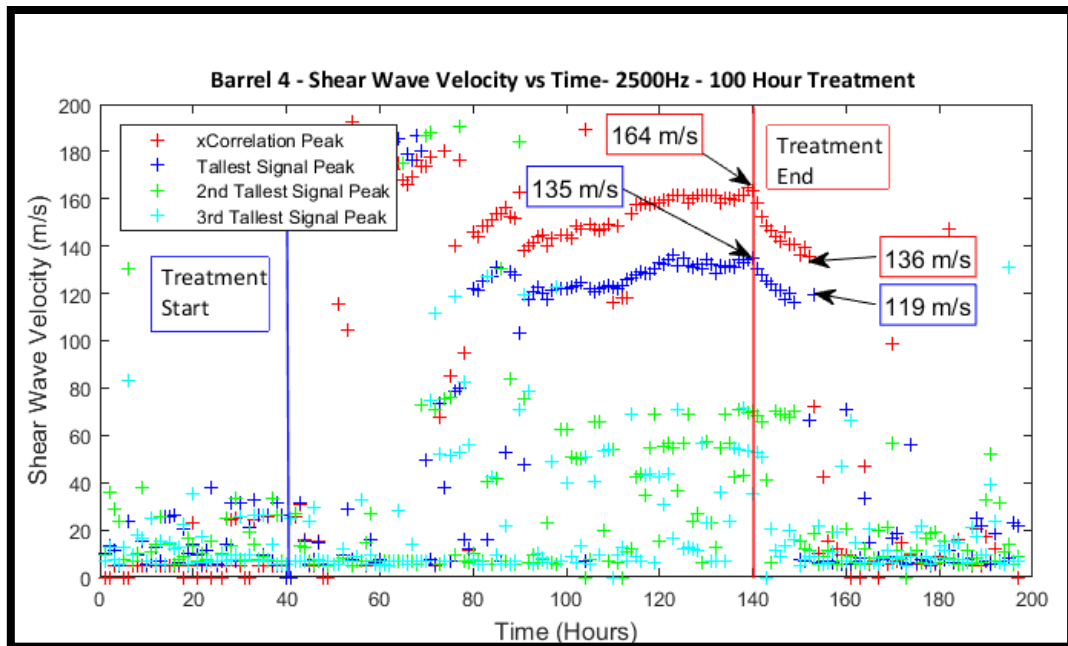


FIGURE 3.19: BARREL 4 SHEAR WAVE VELOCITY, 2500HZ OUTPUT, 100 HOURS TREATMENT

3.3. Shear Strength

Shear vane tests were performed on all four barrels 2 weeks after load tests were performed.

This was done in a circular pattern both close to the pile and close to the electrodes at points three and one in Figure 2.36 for all octants. The total results of water content vs shear strength (S_u) are summarized in Table 3.2 and Figure 3.23 through Table 3.6 and Figure 3.26. Shear vane results show that shear strength is significantly higher around the pile, and highest at depth. High shear strength around the pile is expected as not only is water content reduced significantly near the pile, but iron oxide is created and physically cements the soil to itself and to the pile, shown by the presence of bright orange streaks adjacent to the pile when soil is peeled away after the loading process, shown in Figure 3.21. If the soil is forcibly removed, large pits will be left, shown in Figure 3.20. It should be noted that when designing these electrokinetic systems, the longer the treatment is performed, the more section loss can be expected which must be accounted for in pile design. On average, there was about 1mm of total cross section lost, with pits being an average of 0.5mm deep, and at most 1.5mm deep.



FIGURE 3.20: LARGE PIT IN PILE



FIGURE 3.21: SAMPLE TAKEN ADJACENT TO TREATED PILE

Higher shear strength around the base of the pile is possibly caused by the loading process as the clay tended to form a plug. When comparing the shear vane results, take note that no significant disparity in strength is observed between treated barrels even though treatment times and load carrying capacities are significantly different. There is also no pattern as to where the improvement occurs in the results of shear vane testing, solely that it is highest at the base and lowest at the surface which could be due to higher confining pressures. This shows that although shear vane tests are less destructive, they are still inadequate to determine treatment end time, nor in estimating load carrying capacity in a predictable fashion.

3.3.1.1. Barrel 3 – Control

Shown below in Figure 3.22 and Table 3.2 are the shear vane results of the untreated barrel. Shear strength is linear with water content in the range of liquid limit which is about 25% (Table 3.7) and is consistent both near and far from the pile. This also shows that the loading of the pile has little consequence on shear strength in the lower regions.

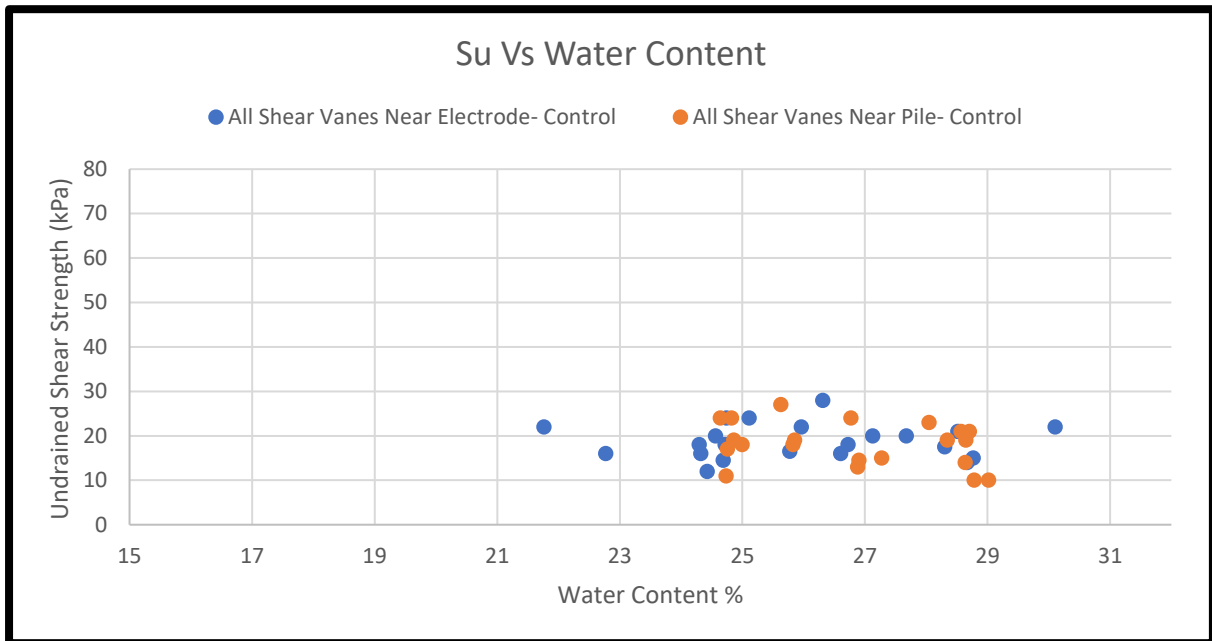


FIGURE 3.22: ALL SHEAR VANE RESULTS FOR BARREL 3 – CONTROL

TABLE 3.2: SHEAR VANE AND WATER CONTENT FOR BARREL 3- CONTROL

	Close to Electrode				Close to Pile		
	Depth in Inches	Su (kPa)	Water Content %		Depth in Inches	Su (kPa)	Water Content %
A1	3	12	24.427	A3	3	13	26.882
	8	14	28.671		8	10	29.02
	13	15	28.767		13	NA	NA
B1	3	22	21.765	B2	3	15	26.582
	8	16.5	14.394		8	19	27.273
	13	17.5	28.302		13	14.5	28.649
C1	3	18	24.719	C3	3	19	22.222
	8	24	24.742		8	19	26.904
	13	22	30.108		13	24	25.854
D1	3	24	25.112	D2	3	18	24.862
	8	18	24.299		8	23	24.643
	13	20	27.679		13	24	25.828
E1	3	16	24.324	E3	3	11	28.571
	8	28	26.316		8	21	28.346
	13	22	25.962		13	18	24.759
F1	3	16	22.772	F2	3	14	24.828
	8	16	26.608		8	24	25.628
	13	20	27.129		13	27	28.783
G1	3	18	26.728	G3	3	10	28.049
	8	14.5	24.691		8	21	26.772
	13	21	34.263		13	19	24.734
H1	3	20	24.561	H2	3	17	28.704
	8	16.5	25.778		8	24	25
	13	21	28.519		13	24	28.636

3.3.1.2. Barrel 1 Shear Vane – Treated 170 Hours

Comparing the results of barrel 1 to the control (Figure 3.23 and Table 3.3) it can be seen that shear strength in the barrel 1 is higher while water content lower, with the most change occurring close to the pile (anode). These results are typical for all barrels which were treated. The high level of variability in shear strength is attributed to the heterogenous nature of the chemical reactions. Slight differences in distance between the pile and electrodes and the asymmetrical geometry of the pile create areas with lower electrical resistance. These areas of low electrical resistance create zones with higher current density and therefore higher shear strength over the course of treatment. Shear strength along the base of the treated piles showed the greatest variability in water content and shear strength. Relationships between water content and shear strength are poorly defined compared to the control as a result.

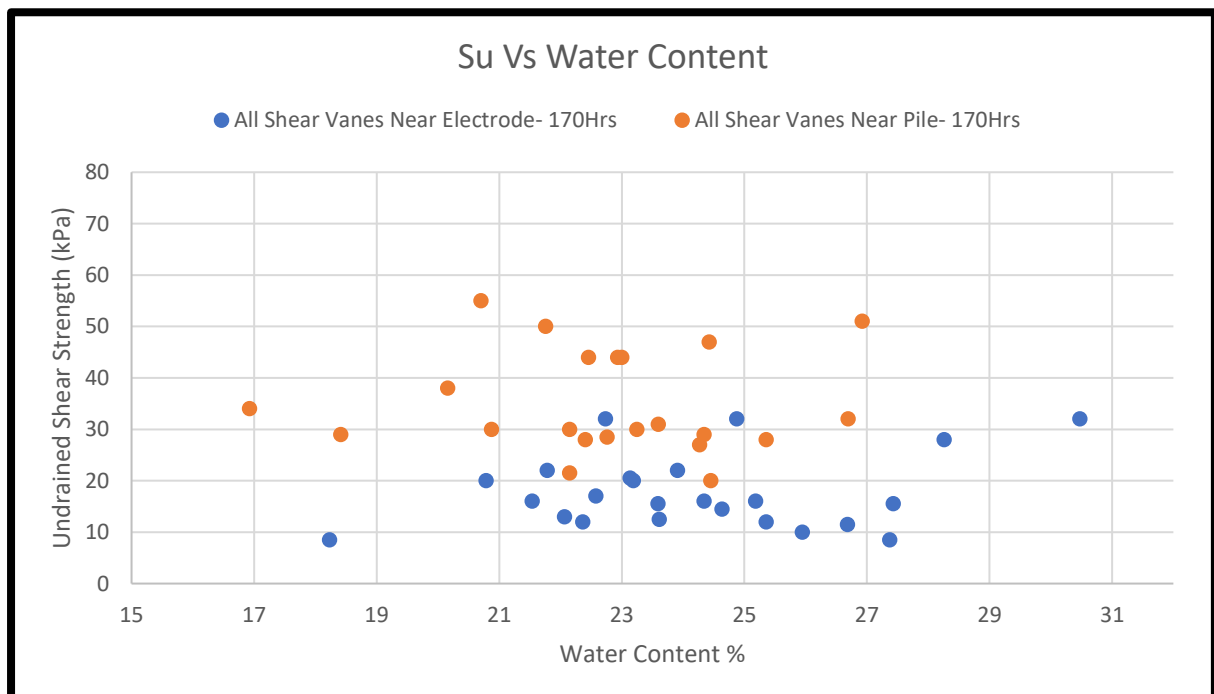


FIGURE 3.23: ALL SHEAR VANE RESULTS FOR BARREL 1

TABLE 3.3: SHEAR VANE AND WATER CONTENT FOR BARREL 1

	Close to Electrode				Close to Pile		
	Depth in Inches	Su (kPa)	Water Content %		Depth in Inches	Su (kPa)	Water Content %
A1	3	8.5	27.4	A3	3	20	24.5
	8	12.5	23.6		8	28	22.4
	13	16	21.5		13	34	16.9
B1	3	15.5	27.4	B2	3	NA	NA
	8	20.5	23.1		8	28.5	22.2
	13	16	24.3		13	29	22.8
C1	3	11.5	26.7	C3	3	NA	NA
	8	20	20.8		8	44	24.3
	13	28	28.3		13	44	25.4
D1	3	15.5	23.6	D2	3	29	23
	8	20	23.2		8	32	22.9
	13	32	24.9		13	47	18.4
E1	3	16	25.2	E3	3	31	21.8
	8	22	23.9		8	27	22.5
	13	32	22.7		13	51	23.2
F1	3	13	22.1	F2	3	30	20.2
	8	12	22.4		8	38	20.7
	13	12	25.4		13	55	22.1
G1	3	8.5	18.2	G3	3	30	26.7
	8	17	22.6		8	50	24.4
	13	32	30.5		13	44	23.6
H1	3	10	25.9	H2	3	30	24.3
	8	14.5	24.6		8	38	26.9
	13	22	21.8		13	49	20.9

3.3.1.3. Barrel 2 Shear Vane – Treated for 55 Hours

From the results in Table 3.4 and Figure 3.24, observe that even though water content changes drastically in some areas of barrel 2, the shear strength does not increase appreciably. Not only this but there are still many samples which were near the pile with shear strength and water contents that match that of the tests which were near the electrodes. This demonstrates that the treatment time was insufficient to adequately purge the soil of water and induce cementation across the entire soil profile.

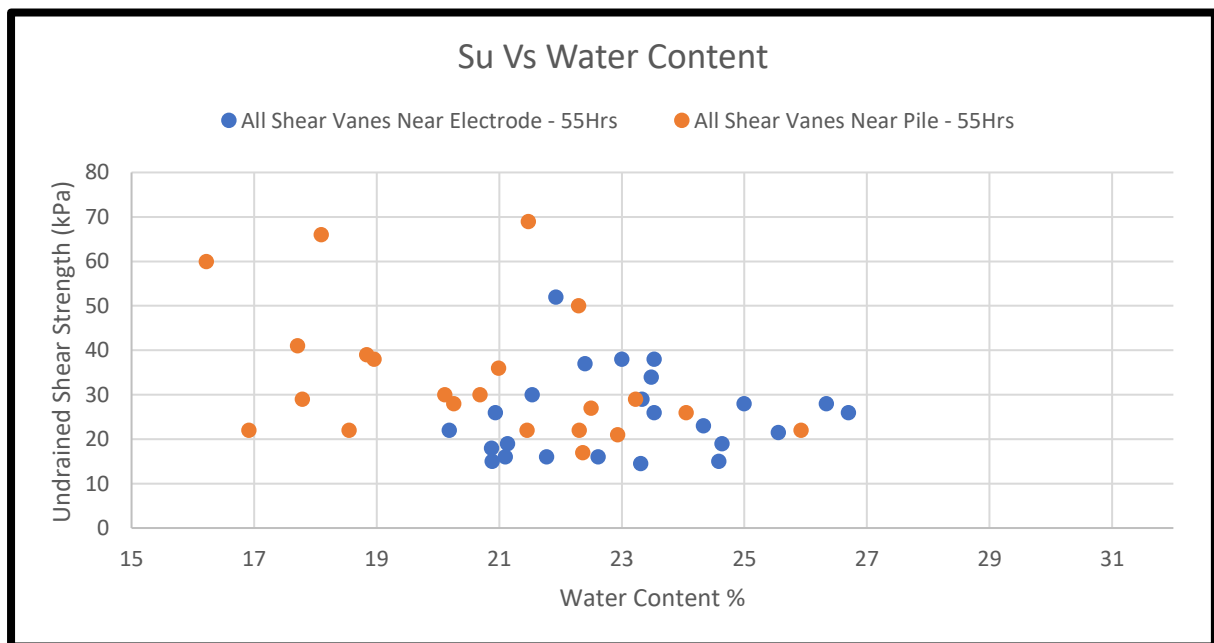


FIGURE 3.24: ALL SHEAR VANE RESULTS FOR BARREL 2

TABLE 3.4: SHEAR VANE AND WATER CONTENT FOR BARREL 2

	Close to Electrode				Close to Pile		
	Depth in Inches	Su (kPa)	Water Content %		Depth in Inches	Su (kPa)	Water Content %
A1	3	22	20.2	A3	3	41	17.7
	8	14.5	23.3		8	39	18.8
	13	21.5	25.6		13	66	18.1
B1	3	16	21.1	B2	3	22	22.0
	8	16	22.6		8	17	25.9
	13	19	21.1		13	27	22.4
C1	3	18	20.9	C3	3	22	15.5
	8	19	24.6		8	26	22.5
	13	23	24.3		13	29	21.5
D1	3	15	24.6	D2	3	21	24.1
	8	28	25.0		8	22	23.2
	13	29	23.3		13	36	22.9
E1	3	26	23.5	E3	3	22	19.0
	8	30	21.5		8	50	16.2
	13	26	26.7		13	69	20.1
F1	3	15	20.9	F2	3	22	17.8
	8	28	26.3		8	29	20.7
	13	38	23.5		13	30	20.3
G1	3	16	21.8	G3	3	28	16.9
	8	38	23.0		8	38	21.0
	13	34	23.5		13	60	18.6
H1	3	37	22.4	H2	3	30	22.3
	8	26	20.9		8	22	21.5
	13	52	21.9		13	40	22.3

3.3.1.4. Barrel 3 – Treated 115 Hours

Shear vane results for barrel 3 post-treatment are shown in Table 3.5 Figure 3.25. Drastic changes in both shear strength and water content are observed with several incidences of high shear strength in the range of 40 to 70 kPa (like barrel 1) versus the results from barrel 2. This is however contrasted against the samples which had relatively low shear strength even at low water contents which is not the case in barrel 2 which had a more even distribution of shear strength at various water contents. These instances of low shear strength at low water content are likely due to the lack of pile-soil contact which was discussed earlier (caused by poor installation of pile in soil). It is likely that load capacity of this pile after treatment would have matched that of barrel 4, especially as they have very similar load-displacement curves in the low displacement region.

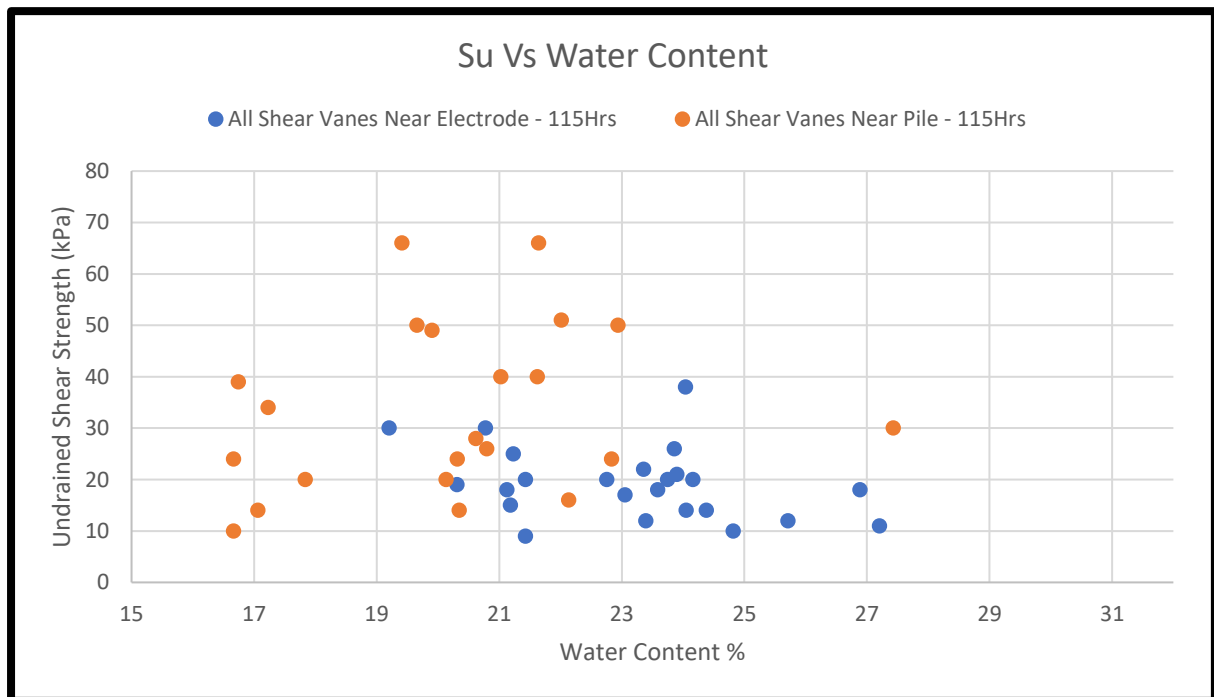


FIGURE 3.25: ALL SHEAR VANES FOR BARREL 3 – TREATED

TABLE 3.5: SHEAR VANE AND WATER CONTENT FOR BARREL 3-TREATED

	Close to Electrode				Close to Pile		
	Depth in Inches	Su (kPa)	Water Content %		Depth in Inches	Su (kPa)	Water Content %
A1	3	19	20.3	A3	3	66	19.4
	8	20	23.8		8	30	27.4
	13	18	26.9		13	40	21.6
B1	3	30	19.2	B2	3	49	19.5
	8	15	21.2		8	50	19.9
	13	12	25.7		13	24	22.9
C1	3	20	21.4	C3	3	14	23.2
	8	26	23.9		8	24	20.3
	13	25	21.2		13	39	20.3
D1	3	20	22.8	D2	3	34	16.7
	8	20	24.2		8	50	16.7
	13	14	24.1		13	16	17.2
E1	3	38	24	E3	3	40	17.8
	8	18	21.1		8	51	17.1
	13	10	24.8		13	24	16.7
F1	3	30	20.8	F2	3	66	20.8
	8	9	21.4		8	26	20.1
	13	18	23.6		13	20	20.6
G1	3	17	23.1	G3	3	28	19.7
	8	11	27.2		8	20	22.1
	13	12	23.4		13	14	21
H1	3	21	23.9	H2	3	10	22
	8	22	23.4		8	24	22.8
	13	14	24.4		13	18	21.6

3.3.1.5. Barrel 4 – Treated 100 Hours

The shear strength distribution of barrel 4, shown by Figure 3.26 and Table 3.6, demonstrates a low amount of soil drying compared to the other treated barrels. Even with this low amount of drying, a great deal of shear strength is present. If we consider that the treatment process in barrel 1 to be nearly identical to that of barrel 4, it can be concluded that the increase in load carrying capacity between the pile in barrel 1 and that in barrel 4 had occurred between hours 100 and 170. The shear strength of barrel 1 and 4 are very similar, with the main difference being water content. The conclusion here is that cementation is the main driver of increasing the load carrying of a pile in the early stages of treatment during these tests.

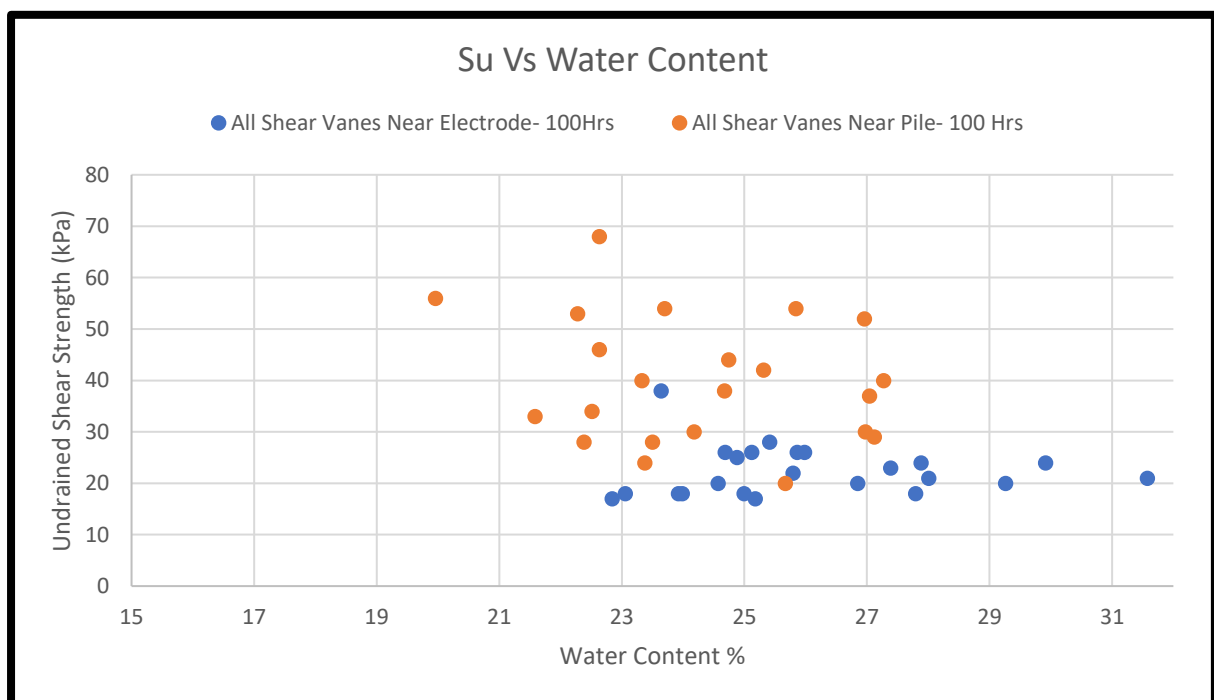


FIGURE 3.26: ALL SHEAR VANE RESULTS FOR BARREL 4

TABLE 3.6: SHEAR VANE AND WATER CONTENT FOR BARREL 4

	Close to Electrode			Close to Pile			
	Depth in Inches	Su (kPa)	Water Content %		Depth in Inches	Su (kPa)	Water Content %
A1	3	12.5	46.4	A3	3	38	24.7
	8	21	31.6		8	40	23.3
	13	22	25.8		13	54	25.8
B1	3	21	28	B2	3	29	25.0
	8	18	25		8	37	27.1
	13	26	26		13	56	27.0
C1	3	18	24	C3	3	24	21
	8	24	27.9		8	30	20
	13	20	26.9		13	40	23.4
D1	3	18	23.1	D2	3	28	27
	8	18	27.8		8	42	27.3
	13	18	23.9		13	44	22.4
E1	3	20	29.3	E3	3	33	22.3
	8	26	25.1		8	34	22.6
	13	38	23.6		13	46	25.7
F1	3	20	24.6	F2	3	30	23.7
	8	25	24.9		8	54	27
	13	23	27.4		13	52	23.5
G1	3	17	22.8	G3	3	28	25.3
	8	26	24.7		8	53	24.7
	13	26	25.9		13	68	21.6
H1	3	17	25.2	H2	3	20	22.5
	8	24	29.9		8	28	22.6
	13	28	25.4		13	38	24.2

3.4. Axial Load Capacity

A summary of treatment time, power consumed and load carrying capacity can be seen in Table 3.1. It can be seen in Figure 3.27 that the load capacities of the piles which were treated are much greater than that of the non-treated pile (control). As seen in Figure 3.27, the load capacity of the pile in barrel 1 after treatment was 550 lbs compared to 200 lbs in the control, representing an increase of 175%. The differences between the load to displacement curve of the pile in barrel 1 and barrel 4 is likely due to changes made to the soil from the introduction of higher levels of iron from the electrokinetic treatment or due to changes that occurred below the receiving bender element at the base of the pile, where shear wave velocity was not measured. The treatment of Barrel 3 was nearly a complete failure because the soil was not in direct contact with the pile and a large void was present all around the pile, except at the base. This resulted in a lack of electrical conductivity which resulted in the treatment being unsuccessful in increasing the carrying capacity of the pile to the extent of barrels 1 or 4, however still creating changes in shear strength where current had passed through the soil (at the base). The load resistance of the pile was shown to have been only at the base as very little contact was made along the sides of the pile. If the load curve of barrel 3 is compared to that of barrel 4, the loading curves are very similar. This shows that the failure behaviour in high-displacement (above 1mm) of barrel 3, which closely resembles that of the control (barrel 3 untreated) is mainly due to the absence of skin resistance, which means that a major source of load capacity increase when displacement is high is attributed to the increase in skin resistance. It is highly probable that the differences between load-carrying capacities between barrels 1 and 4 is not due to any significant difference in shear strength along the length of the pile, but instead changes that occurred at the piles base, which likely experiences shear strength improvement at a lower rate as current takes the path of least resistance which

is the sides of the pile as they offer the highest level of surface area. The load capacity of the piles was determined by drawing a line through the data both before and after the apex of the curve. The angle the lines created was halved and a line was drawn. The maximum load was regarded as the value where this line met the loading curve.

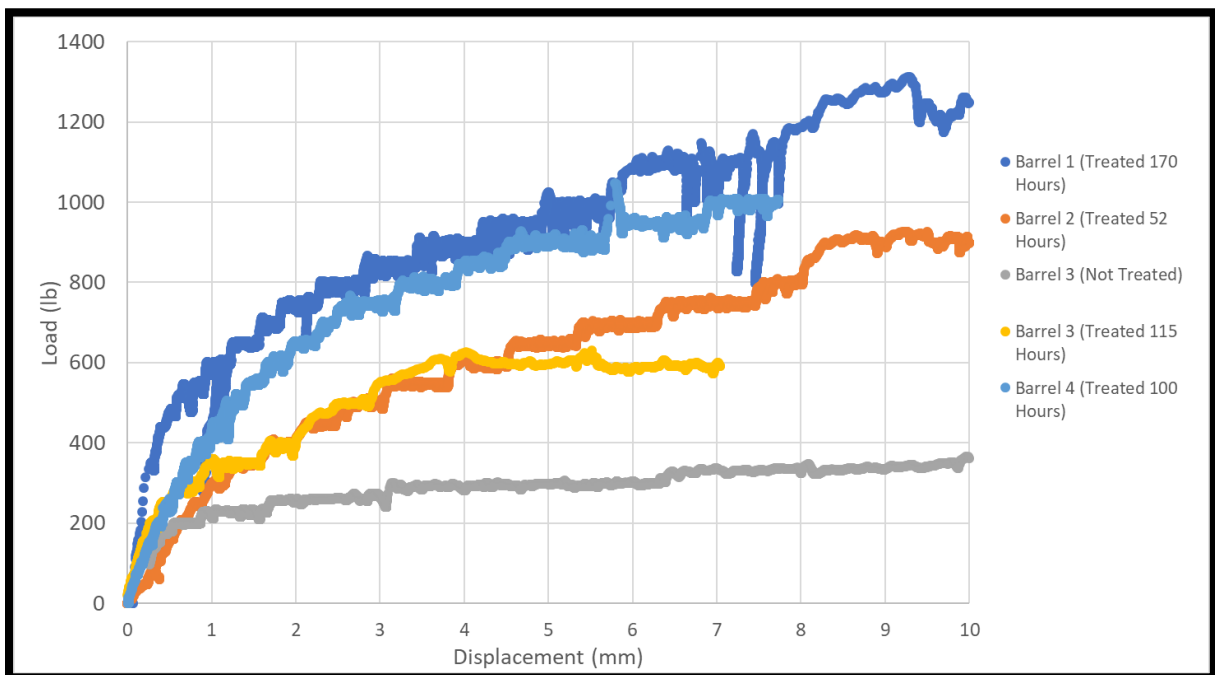


FIGURE 3.27: PILE LOAD CAPACITY OF ALL PILES

3.5. X-Ray Diffraction Spectroscopy

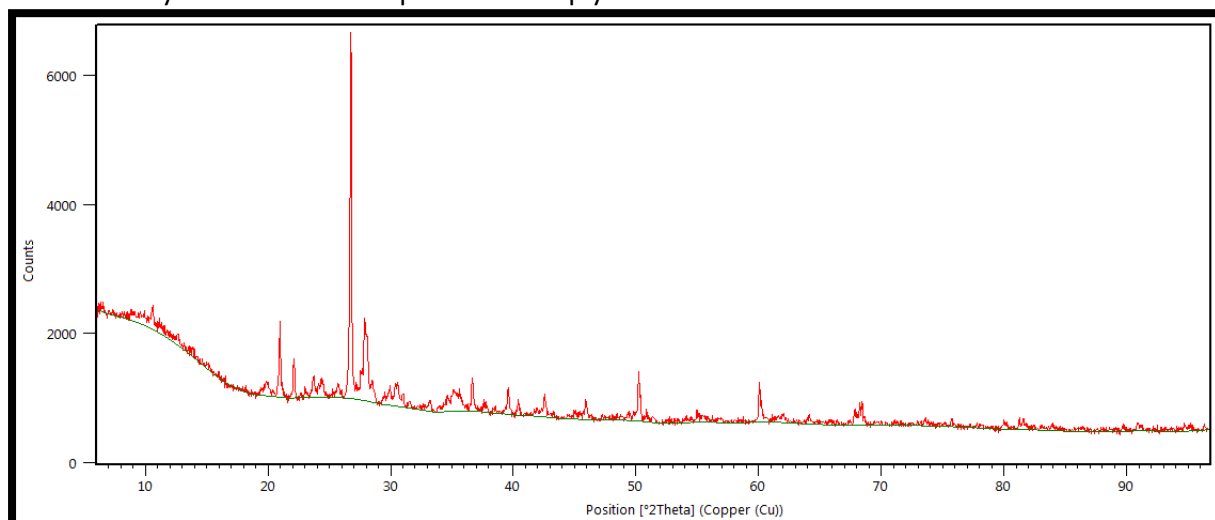


FIGURE 3.28: X-RAY DIFFRACTION RESULTS

Main constituents were Quartz [SiO_2], Albite [$\text{NaAlSi}_3\text{O}_8$] and possibly Anorthite [$\text{CaAl}_2\text{Si}_2\text{O}_8$] (very similar crystal structures) and Muscovite [$(\text{KF})_2(\text{Al}_2\text{O}_3)_3(\text{SiO}_2)_6(\text{H}_2\text{O})$] or [$\text{KAl}_2(\text{AlSi}_3\text{O}_{10})(\text{FOH})_2$]. The use of XRD spectrometry was useful in determining the constitution of the soil from a mineralogical standpoint. When both treated and untreated samples were compared it was clear that XRD would not be able to show any differences in the samples post-treatment. Since the successful use of XRD depends on the new compounds being in a specific crystal structure, and due to the high presence of other compounds within the sample, namely Quartz, it was very difficult to discern any major differences amongst samples. As muscovite was found in the samples it was targeted for further analysis using x-ray energy dispersive spectrometry using a scanning electron microscope.

3.6. Scanning Electron Microscope and X-Ray Energy Dispersive Spectrometry

Initial spectrometry tests of the clay samples showed that there was an elevated level of iron in the muscovite portion of soil close to the pile of treated barrels. Results show that in barrels that received enough treatment had a higher level of incidence of displaying higher levels of

iron, with both content of iron and number of affected particles falling with reduced treatment effectiveness, as displayed by the load carrying capacity. Although the results show only a few particles, there were some particles in barrels 1 and 4 which showed levels of iron above thirty percent. The evidence shown is not statistically relevant however in the past it has not been shown where or how iron is directly affecting the soil. The evidence provided below shows heavily weathered clays to be more susceptible to physical changes due to the presence of iron. Not only this, but the previous belief that cementation was occurring may be incorrect and rather the substitution of iron into the edges of clay particles could be causing them to cling together more tightly, which had been reported by previous research [27].

3.6.1. Control

Iron content in the control was on average below 5%. Iron content appeared stable regardless of location (edge or face of clay). This data is in good agreement with the theoretical molar mass fraction of iron in muscovite, which is 4.75% or 8.71% depending on the form of muscovite.

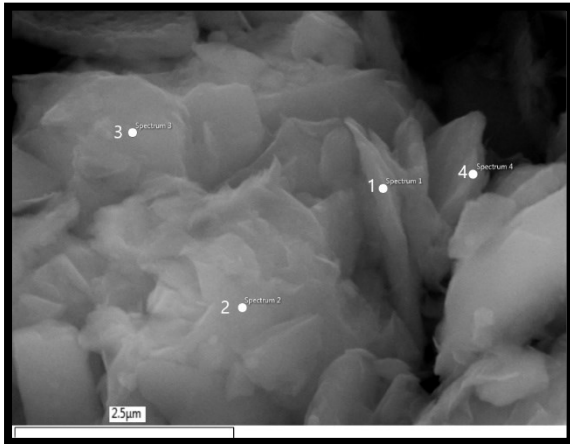


FIGURE 3.29: SEM IMAGE OF MUSCOVITE SHEETS (CONTROL, A2, 20K MAGNIFICATION)



FIGURE 3.30: SEM IMAGE OF MUSCOVITE SHEETS (CONTROL, A3, 20K MAGNIFICATION)

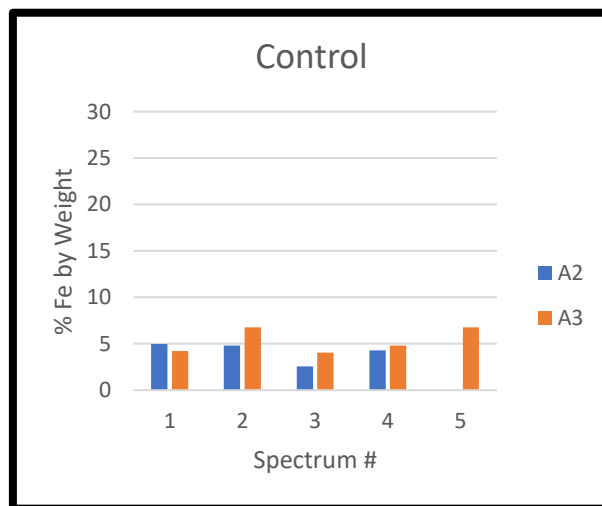


FIGURE 3.31: IRON CONTENT IN BARREL 3 (CONTROL)

3.6.2. Barrel 1

The iron content shown in Figure 3.34 shows elevated levels of iron at clay edges (spectrum 3 and 4 of sample A3), with iron levels at the faces remaining stable. It is likely that this elevated level of iron at the faces is responsible for the increase in strength and changes to Atterberg limits.

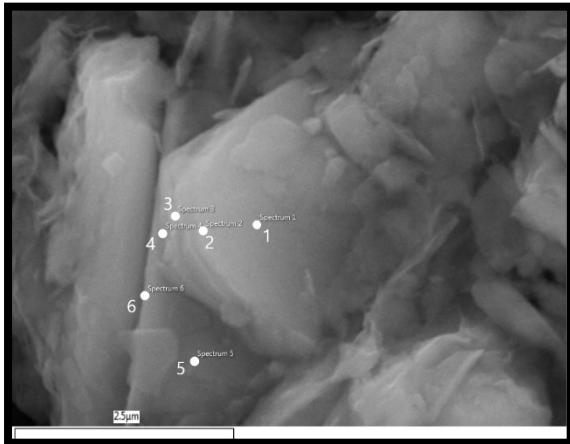


FIGURE 3.32: SEM IMAGE OF MUSCOVITE SHEETS (BARREL 1, A2, 20K MAGNIFICATION)

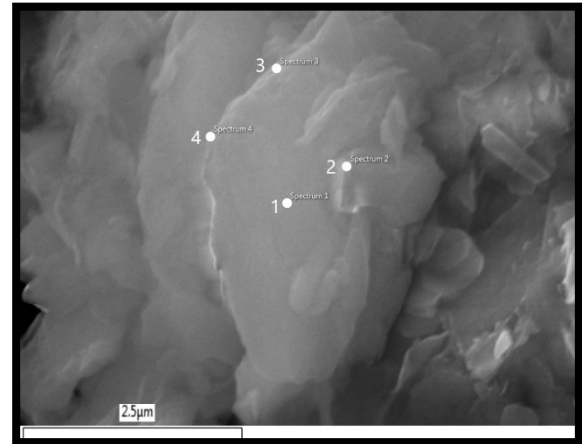


FIGURE 3.33: SEM IMAGE OF MUSCOVITE SHEETS (BARREL 1, A3, 20K MAGNIFICATION)

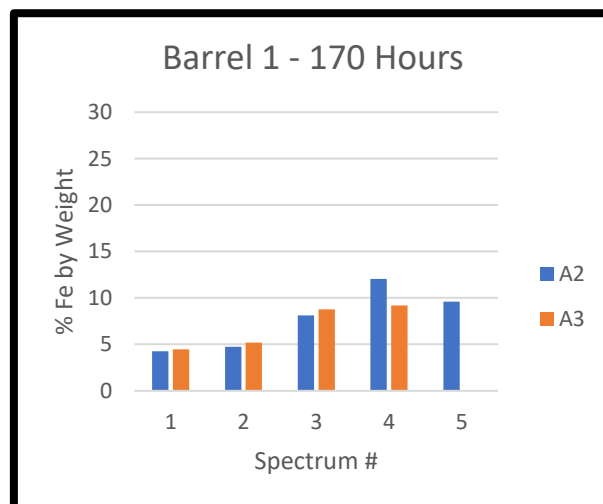


FIGURE 3.34: IRON CONTENT IN BARREL 1

3.6.3. Barrel 2

The following figures show the discrete iron content both adjacent and 3 inches from the pile in barrel 2. High iron content was observed close to the pile caused by corrosion of the pile, but discrete iron content alone was not an indicator of pile load capacity. Note that the spectrum 1, 2 and 4 were taken from the edge of the particle (bright white) shown in Figure 3.36.



FIGURE 3.35: SEM IMAGE OF MUSCOVITE SHEETS (BARREL 2, A2, 20K MAGNIFICATION)

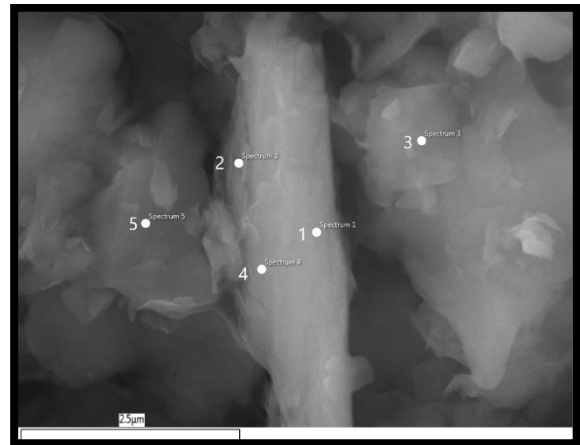


FIGURE 3.36: SEM IMAGE OF MUSCOVITE SHEETS (BARREL 2, A3, 20K MAGNIFICATION)

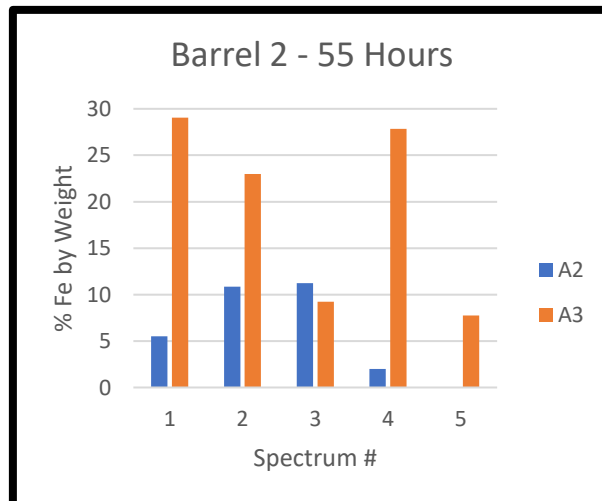


FIGURE 3.37: IRON CONTENT IN BARREL 5

3.6.4. Barrel 3

After 115 hours of treatment, elevated levels of iron were present adjacent to the pile, shown in Figure 3.40. Spectrums 1, 3 and 4 are located at the particles edge and exhibit higher levels of iron than other points.

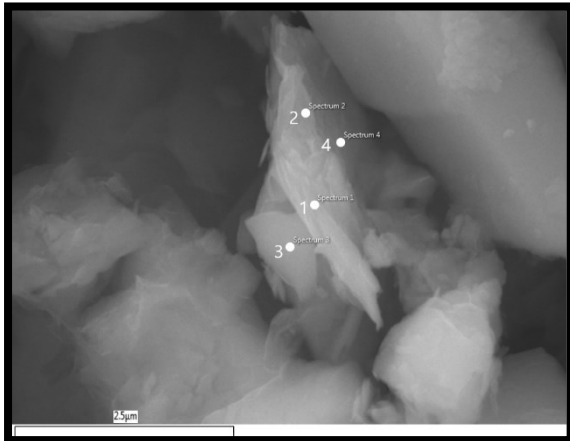


FIGURE 3.38: SEM IMAGE OF MUSCOVITE SHEETS (BARREL 3, A2, 20K MAGNIFICATION)

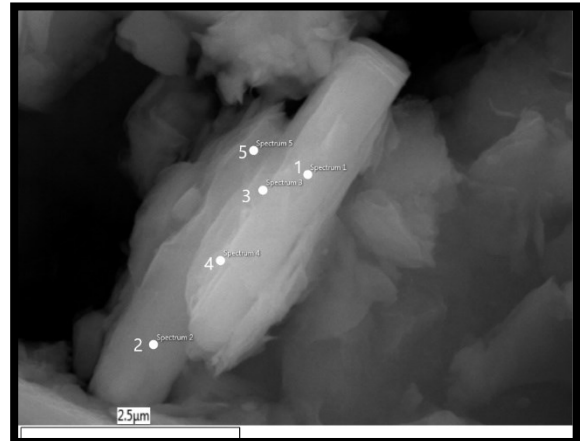


FIGURE 3.39: SEM IMAGE OF MUSCOVITE SHEETS (BARREL 3, A3, 20K MAGNIFICATION)

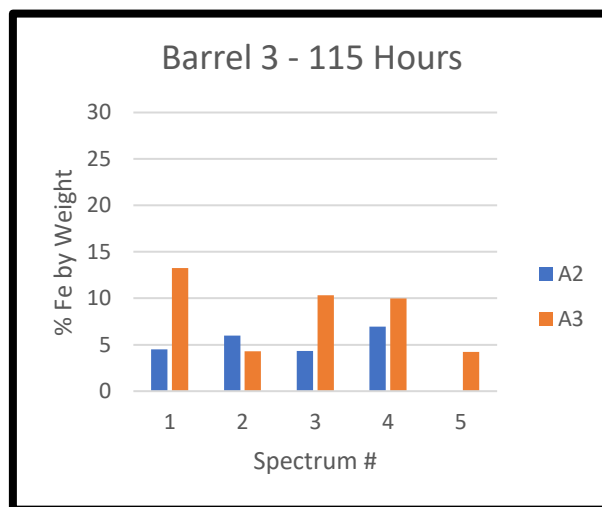


FIGURE 3.40: IRON CONTENT IN BARREL 3

3.6.5. Barrel 4

Figure 3.43 displays heightened levels of iron, with spectrums 2,3 and 4 taken from edge points. The conclusion obtained from these results is two-fold: of the soil treated, the highest levels of iron are located at clay particle edges, and also predicting iron content in the soil is difficult and depends mainly on the paths electrical current takes during treatment.

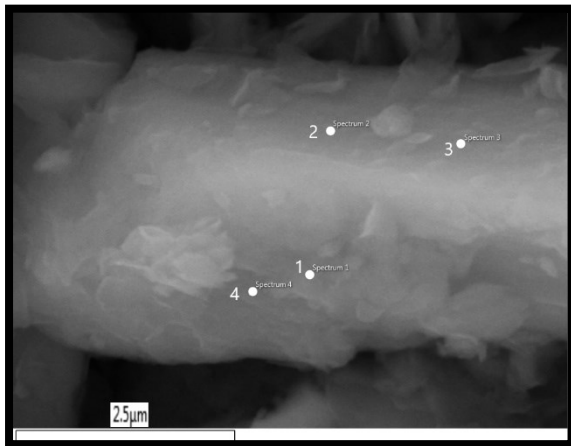


FIGURE 3.41: SEM IMAGE OF MUSCOVITE SHEETS (BARREL 4, A2, 20K MAGNIFICATION)

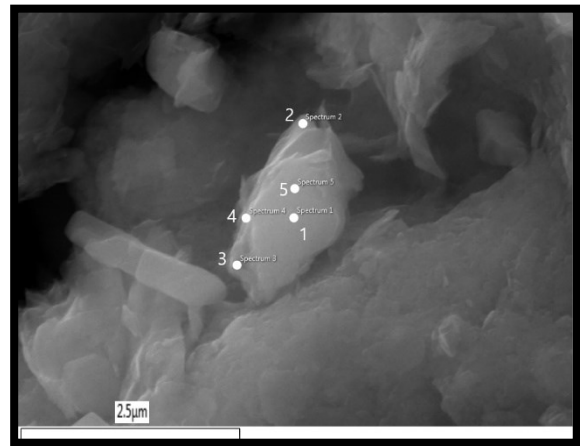


FIGURE 3.42: SEM IMAGE OF MUSCOVITE SHEETS (BARREL 4, A3, 20K MAGNIFICATION)

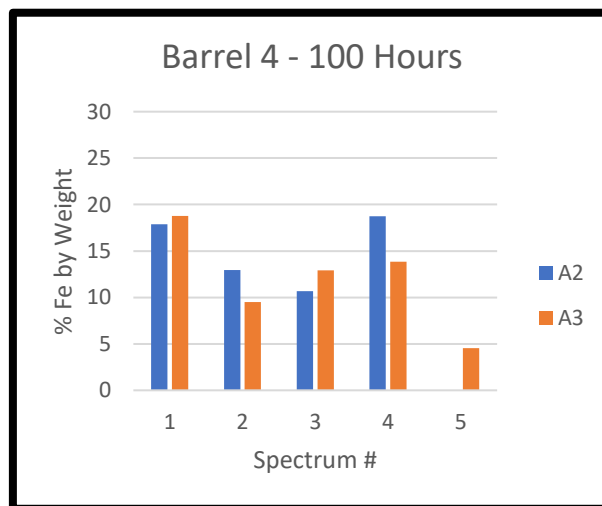


FIGURE 3.43: IRON CONTENT IN BARREL 4

3.7. pH Tests

The pH tests were performed to determine if any significant differences in pH were present in the piles which were treated longer or displayed higher load carrying capacity. Because metals tend to precipitate or dissolve depending on pH, understanding the pH trends could explain the reasons for higher iron content amongst various samples. Results showed that the pH amongst the test had very little effect on iron content or load carrying capacity as all soil tested had very similar trends in pH. This is consistent with the conclusion shown in chapter 3 regarding cementations role in shear strength increases vs that of soil drying, with the implication of similar pH being that cementation reactions begin quickly in the soil.

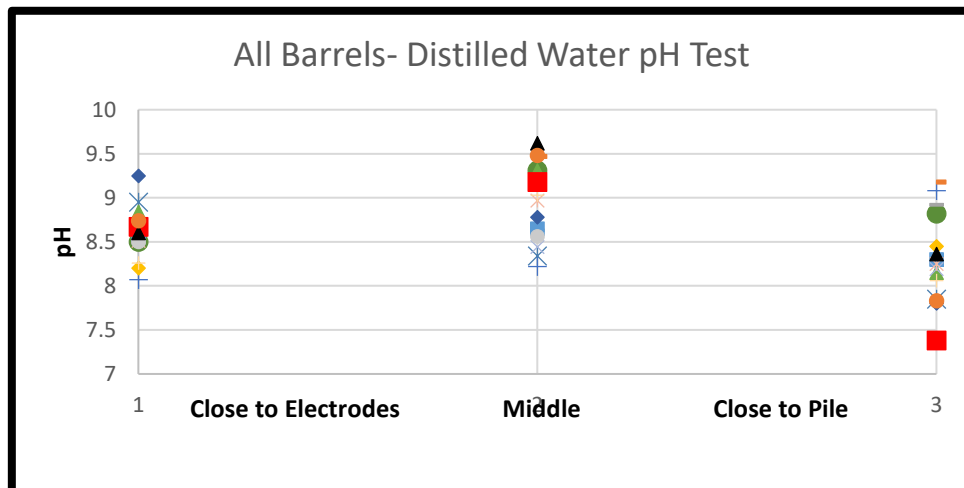


FIGURE 3.44: ALL BARRELS – DISTILLED WATER PH TEST

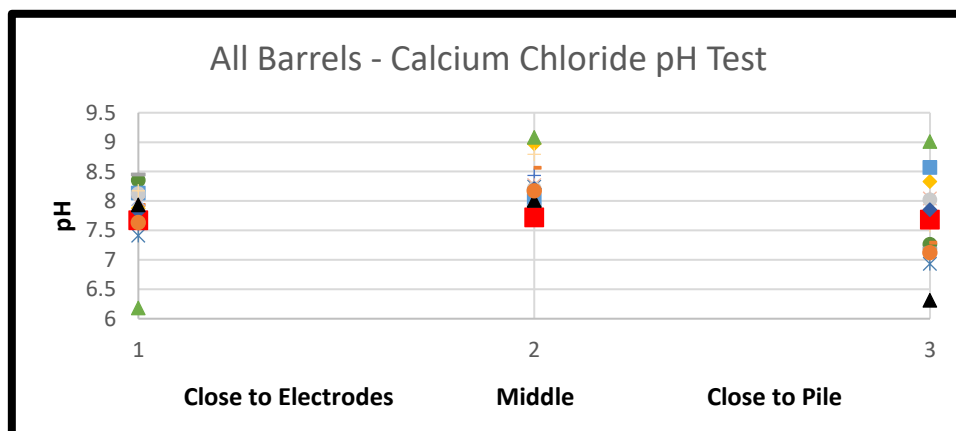


FIGURE 3.45: ALL BARRELS – CALCIUM CHLORIDE PH TEST

Mixed in Distilled Water pH: 7.0				Mixed in Calcium Chloride pH: 8.35			
Barrel 1: 170 Hours							
	1	2	3		1	2	3
Quadrant A	8.95	8.34	7.85	Quadrant A	8.45	8.18	7.19
Quadrant C	8.5	9.31	8.82	Quadrant C	7.87	8.97	8.33
Quadrant E	8.07	8.22	9.08	Quadrant E	8.13	8.01	8.57
Quadrant G	5.71	9.47	9.18	Quadrant G	6.18	9.08	9.01
Barrel 2: 55 Hours							
	1	2	3		1	2	3
Quadrant A	8.49	8.63	8.92	Quadrant A	8.03	8.04	7.9
Quadrant C	8.2	9.15	8.45	Quadrant C	7.96	8.27	8.04
Quadrant E	8.58	8.65	8.3	Quadrant E	8.12	8.21	8.02
Quadrant G	8.84	9.31	8.15	Quadrant G	8.17	8.79	7.58
Control							
	1	2	3		1	2	3
Quadrant A	8.12	7.92	7.96	Quadrant A	7.26	7.38	7.51
Quadrant C	7.65	7.88	8	Quadrant C	7.51	7.64	7.69
Quadrant E	7.76	8.05	8.08	Quadrant E	7.56	7.68	7.65
Quadrant G	7.95	7.8	7.98	Quadrant G	7.7	7.69	7.76
Barrel 3: 115 Hours							
	1	2	3		1	2	3
Quadrant A	8.59	8.44	8.19	Quadrant A	7.67	7.72	7.68
Quadrant C	8.51	8.97	8.25	Quadrant C	7.82	8.21	7.85
Quadrant E	8.5	8.56	6.61	Quadrant E	7.93	8.01	6.31
Quadrant G	8.26	9.03	8.06	Quadrant G	7.63	8.17	7.12
Barrel 4: 110 Hours							
	1	2	3		1	2	3
Quadrant A	8.67	9.18	7.38	Quadrant A	7.41	8.24	6.93
Quadrant C	9.25	8.78	7.8	Quadrant C	8.35	7.88	7.26
Quadrant E	8.6	9.62	8.36	Quadrant E	7.76	8.43	7.68
Quadrant G	8.74	9.48	7.83	Quadrant G	7.93	8.56	7.29

3.8. Atterberg Limits

The Atterberg limits of samples treated for extended periods of time exhibited higher liquid limits and these results coincided well with the increase in load carrying capacity, shown in Figure 3.46 and Figure 3.47. This increase in Atterberg limits is likely due to the increase in iron content on weathered sites of the clay particles, as was seen in x-ray energy dispersive spectroscopy tests from barrels 1 and 4.

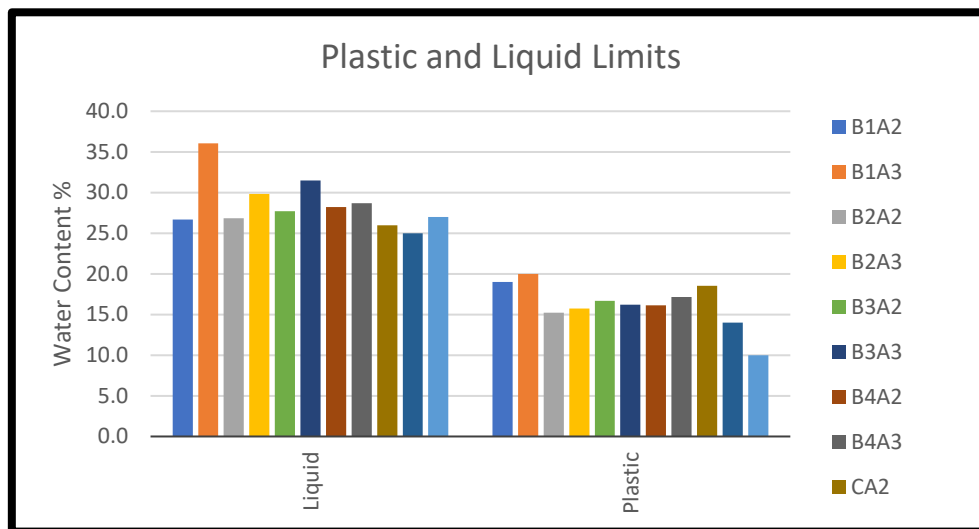


FIGURE 3.46: PLASTIC AND LIQUID LIMITS POST-TREATMENT

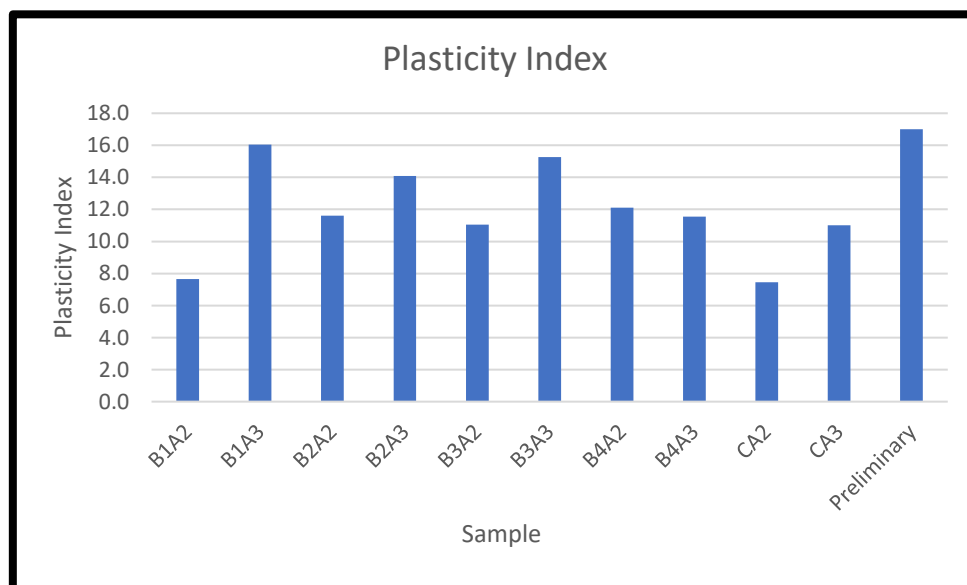


FIGURE 3.47: PLASTICITY INDEX POST-TREATMENT

TABLE 3.7: SUMMARY OF LIQUID AND PLASTIC LIMITS

	B1A2	B1A3	B2A2	B2A3	B3A2	B3A3	B4A2	B4A3	CA2	CA3	Preliminary
Liquid Limit	26.7	36	26.8	29.8	27.7	31.5	28.2	28.7	26	25	27
Plastic Limit	19	20	15.2	15.7	16.7	16.2	16.1	17.1	16.5	14	10
Plasticity Index	7.7	16	11.6	14.1	11	15.3	12.1	11.6	9.5	11	17

3.9. Sources of Error/ Variability

The delay between the signal leaving the DAQ and the one leaving the amplifier is approximately $3\mu\text{s}$. This is so minute that the difference between the actual shear wave velocity and that rendered by the DAQ for a shear wave velocity of 200 m/s would be 0.5 m/s, therefore it was ignored.

Although the piles were held as level as possible during the process of installing them, some eccentricity in the piles was present. This could cause some difference in the load observed by the strain gage at the pile head and the actual load applied along the long-axis of the pile. Because the piles were loaded using a hand powered hydraulic press, the loading rate for each pile varied considerably. This could cause some loads and strains to be higher or lower than would be experienced otherwise. Another source of error is attributed to the method in which the piles were buried. Differences in the amount of force used to pack the material down could have caused some piles to hold more load. In the instance of Barrel 3, when the pile and soil were removed following the loading of the control test the person who had buried the previous piles had an injury and could no longer perform the task of burying the pile. The individuals who buried the pile did not ensure that the area around the pile was free of voids and this caused several issues, one of which was a drastic difference in load capacity.

Treatment for barrels one and four was commenced within a day of being filled with soil and water, whereas barrels two and three had sat for multiple weeks. This created a condition where there was ample free pore-water in the soil. This is likely the cause for the drastic difference in power consumed. Barrel 3 experienced a drastic difference in power consumed as there were large sections along the web of the pile which were not in contact with the soil, leaving the pile end as the only area of contact.

During the shear vane tests performed on the untreated barrel, the presence of sand and larger gravel sized particles created less disparity amongst the shear strength. In the treated specimens with a higher shear strength this created areas where failure was not smooth and therefore more abrupt, possibly giving values that were much higher than they were.

Differences among XRD results from sample to sample would be attributed to the heterogenous nature of soil and were not found to be significant at all.

Because soils are naturally heterogenous, there will invariably be particles with drastically higher iron content than others, whether this is induced by electrokinetics or not is up for debate. Although it is not shown in the scanning electron microscope data, during the tests it was observed that the iron content in the control was invariably low and stable and that of the treated samples was either on par or much higher, exhibiting erratic results. The samples shown are single particles and therefore do not speak of the entire area but are merely used to observe where the zones with high iron content tend to occur on a particle by particle basis.

The pH tests were performed on select soil samples and any variability is directly attributed to the heterogenous nature of the chemical reactions.

Sources of error for the Atterberg liquid limits test performed include the amount of soil in the cup, the blow rate, cleanliness of cup, soil rest time in cup.

Chapter 4 – Summary and Conclusion

In this study, a steel pile foundation model was created and treated with electrokinetics.

During the treatment, bender elements were placed alongside the steel pile and shear waves were transmitted through the soil periodically to measure the shear wave velocity. After the shear wave velocity ceased to increase, the treatment was deemed to be finished and the piles were loaded two-weeks later. The first pile treated was a trial and later treatment was performed based on the information gained.

In all piles treated, the load capacity was increased, however when bender elements were used to determine the time of completion, the efficiency of the process was optimized.

- Treatment time was reduced from 170 hours to 100 hours..
- Power Consumed was also reduced from 5690 Wh to 3760 Wh.
- Load capacity was increased from 550lbs to 600 lbs, vs the control at 200 lbs.

In addition to these findings, the nature of soil cementation and changes to Atterberg limits in soils treated with electrokinetics without additives was discussed, finding that the iron oxide from the electrolysis reactions was binding directly to clay edges, possibly via isomorphic substitution.

In conclusion, using bender elements removes the uncertainties involved in using electrokinetics for increasing the load carrying capacity and has opened new avenues of research relating to the mechanisms in which load carrying capacity is increased through electrokinetics.

4.1. Future Avenues of Research and Improvements

Bridging the gap between research and application is of utmost concern for electrokinetics and is the main drive of the research. Using shear-waves it was possible to determine when

the shear wave velocity of a soil had reached its peak which dictated when treatment should be finished. Future research should focus on the following:

- Create more reliable bender elements that do not fail under the influence of an electric field.
- Create a system that does not require bender elements and piles to be buried to function.
- Understanding why shear-wave velocity drops after treatment is terminated and what factors contribute to this.
- Run tests in which water is slowly purged from a sample while measuring shear wave velocity to better understand how moisture content affects shear-wave velocity.

Bibliography

- [1] V. Milligan, "First application of electro-osmosis to improve friction pile capacity - three decades later," *ICE: Geotechnical Engineering*, vol. 113, no. 2, pp. 112-116, 1995.
- [2] U.S. Army Corps of Engineers, "Electrical Stabilization of Fine-Grained Soils," *Summary Reviews of Soil Stabilization Processes*, vol. 3, no. 122, pp. 1-29, 1961.
- [3] S. Jayasekera, "Electrokinetics to Modify Strength Characteristics of Soft Clayey Soils: A Laboratory Based Investigation," *Electrochimica Acta*, pp. 39-47, 2015.
- [4] A. Rittirong, R. S. Douglas, J. Q. Shang and E. C. Lee, "Electrokinetic improvement of soft clay using electrical vertical drains," *Geosynthetics International*, vol. 15, no. 5, pp. 369-381, 2008.
- [5] A. Alshawabkeh and T. Sheahan, "Soft soil stabilisation by ionic injection under electric fields," *Proceedings of the Institution of Civil Engineers - Ground Improvement*, vol. 7, no. 4, pp. 177-185, 2003.
- [6] A. Alshawabkeh, T. Sheahan and X. Wu, "Coupling of electrochemical and mechanical processes in soils under DC fields," *Mechanics of Materials*, vol. 36, no. 5-6, pp. 453-465, 2004.
- [7] P. Asavadirbdeja and U. Glawe, "Electrokinetic Strengthening of Soft clay using the anode depolarization method," *The Bulletin of Engineering Geology and the Environment*, pp. 237-245, 2005.

- [8] A. T. Yeung, C.-n. Hsu and R. M. Menon, "EDTA-Enhanced Electrokinetic Extraction of Lead," *Journal of Geotechnical Engineering*, pp. 666-676, 1996.
- [9] M. Malekzadeh, J. Lovisa and N. Sivakugan, "An Overview of Electrokinetic Consolidation of Soils," *Geotechnical and Geological Engineering*, vol. 34, no. 3, pp. 1-18, 2016.
- [10] E. Mohamedelhassan and J. Q. Shang, "Electrokinetics-generated pore fluid and ionic transport in an offshore calcareous soil," *Canadian Geotechnical Journal*, 2003.
- [11] J. Q. Shang, E. Mohamedelhassan and M. Ismail, "Electrochemical cementation of offshore calcareous soil," *Canadian Geotechnical Journal*, vol. 41, pp. 877-893, 2004.
- [12] E. Mohamedelhassan, "Laboratory Model Test on Improving the Properties of Soft Clay by Electrokinetics," *ISRN Civil Engineering*, pp. 1-14, 2011.
- [13] S. Micic, J. Q. Shang, K. Y. Lo and S. W. Lee, "Electrokinetic strengthening of a marine sediment," *Canadian Geotechnical Journal*, vol. 38, no. 2, pp. 287-302, 2001.
- [14] S. Bourges-Gastaud, G. Stoltz, P. Dolez, E. Blond and N. Touze-Foltz, "Laboratory device to characterize electrokinetic geocomposites for fluid fine tailings dewatering," *Canadian Geotechnical Journal*, pp. 505-514, 2015.
- [15] K.-J. Kim, D.-H. Kim, J.-C. Yoo and K. Baek, "Electrokinetic extraction of heavy metals from dredged marine sediment," *Separation and Purification Technology*, pp. 164-169, 2011.
- [16] S. Glendinning, C. Jones, J. Lamont-Black, A. Rittirong, J. Shang and E. C. Lee, "Part Two: Electrokinetic, Thermal, and Explosion-Based Techniques," in *Ground Improvement Case*

Histories: Chemical, Electrokinetic, Thermal and Bioengineering Methods, Elsevier, 2014, pp. 403-513.

[17] M. T. Ammami, F. Portet-Koltalo, A. Benamar, C. Duclairoir-Poc, H. Wang and F. Le Derf, "Application of biosurfactants and periodic voltage gradient for enhanced electrokinetic remediation of metals and PAHs in dredged marine sediments," *Chemosphere*, vol. 125, pp. 1-8, 2015.

[18] K. R. Reddy and C. Cameselle, *Electrochemical Remediation Technologies for Polluted Soils, Sediments and Groundwater*, Wiley, 2009.

[19] I. Hassan, E. Mohamedelhasan and E. Yanful, "Solar powered electrokinetic remediation of Cu polluted soil using a novel anode configuration," *Electrochimica Acta*, vol. 181, pp. 58-67, 2015.

[20] A. T. Yeung, "Fundamental aspects of prolonged electrokinetic flows in kaolinites," *Geomechanics and Geoengineering*, pp. 13-25, 2006.

[21] J. Lamont-Black, C. Jones and D. Alder, "Electrokinetic strenghtening of slopes - Case history," *Geotextiles and Geomembranes*, pp. 319-331, 2016.

[22] S. Micic, J. Q. Shang and K. Y. Lo, "Improvemnt of the load-carrying capacity of offshore skirted foundations by electrokinetics," *Canadian Geotechnical Journal*, pp. 949-963, 2003.

[23] C. Cameselle, "Enhancement of Electro-Osmotic Flow During the Elecktrokinetic Treatment Of A Contaminated Soil," *Electrochimica Acta*, pp. 31-38, 2015.

- [24] H. Keykha, B. Huat and A. Asadi, "Electro-biogrouting stabilisation of soft soil," *Environmental Geotechnics*, vol. 2, no. 5, pp. 292-300, 2015.
- [25] C.-Y. Ou, S.-C. Chien and H.-H. Chang, "Soil improvement using electroosmosis with the injection of chemical solutions:field tests," *Canadian Geotechnical Journal*, vol. 46, pp. 727-733, 2009.
- [26] K. Y. Lo, I. I. Inculet and K. S. Ho, "Electroosmotic strengthening of soft sensitive clays," *Canadian Geotechnical Journal*, vol. 28, pp. 62-73, 1991.
- [27] H. Wu and L. Hu, "Microfabric change of electro-osmotic stabilized bentonite," *Applied Clay Science*, vol. 101, pp. 503-509, 2014.
- [28] L. Zhang, N. Wang, L. Jing, C. Fang, Z. Shan and Y. Li, "Electro-Osmotic Chemical Treatment for Marine Clayey Soils: A Laboratory Experiment and A Field Study," *ASTM: Geotechnical Testing Journal*, pp. 1-12, 2016.
- [29] Y. Cai, Q. Dong, J. Wang, C. Gu and C. Xu, "Measurement of small strain shear modulus of clean and natural sands in saturated condition using bender element test," *Soil Dynamics and Earthquake Engineering*, pp. 100-110, 2015.
- [30] J. Camacho-Tauta, H. Ali, G. Cascante and A. Viana Da Fonesca, "Experimental and Numerical Observations of the Frequency-Domain Method in Bender-Element Testing," *Journal of Geotechnical and Geoenvironmental Engineering*, vol. 143, no. 2, 2017.

- [31] Y. Wang, N. Benahmed, Y. J. Cui and A. M. Tang, "A novel method for determining the small-strain shear modulus of soil using the bender elements technique," *Canadian Geotechnical Journal*, vol. 54, pp. 280-289, 2017.
- [32] P. J. Vardanega and M. D. Bolton, "Stiffness of Clays and Silts: Normalizing Shear Modulus and Shear Strain," *Journal of Geotechnical and Geoenvironmental Engineering*, 2013.
- [33] H. Xiao, K. Yao, Y. Liu, S. H. Goh and F. H. Lee, "Bender element measurement of small strain shear modulus of cement-treated marine clay - Effect of test setup and methodology," *Construction and Building Materials*, vol. 172, pp. 433-447, 2018.
- [34] APC International, "Knowledge Center: Piezo Theory," 2 December 2011. [Online]. Available: <https://www.americanpiezo.com/knowledge-center/piezo-theory/piezoelectricity.html>. [Accessed 20 December 2017].
- [35] T. Ogino, T. Kawaguchi, S. Yamashita and S. Kawajiri, "Measurement deviations for shear wave velocity of bender element test using time domain, cross-correlation, and frequency domain approaches," *Soils and Foundations*, 2015.
- [36] T. Kawaguchi, T. Ogino, S. Yamashita and S. Kawajiri, "Identification method for travel time based on the time domain technique in bender element tests on sandy and clayey soils," *Soils and Foundations*, 2016.
- [37] M. Finas, H. Ali, G. Cascante and P. Vanheeghe, "Automatic Shear Wave Velocity Estimation in Bender Element Testing," *Geotechnical Testing Journal*, vol. 39, no. 4, 2016.

- [38] J.-S. Lee and J. C. Santamarina, "Bender Elements: Performance and Signal Interpretation," *Journal of Geotechnical and Geoenvironmental Engineering*, pp. 1063-1070, 2005.
- [39] Piezo Systems, "Introduction to Piezo Transducers," Mide Technology, [Online]. Available: <http://piezo.com/tech2intropiezotrans.html>. [Accessed 10 December 2017].
- [40] R. Ingale, A. Patel and A. Mandal, "Performance analysis of piezoceramic elements in soil: A review," *Sensors and Actuators A: Physical*, pp. 46-63, 2017.
- [41] K. H. Chan, T. Boonyatee and T. Mitachi, "Effect of bender element installation in clay samples," *Geotechnique*, 2010.
- [42] A. Patel, D. N. Singh and K. K. Singh, "Performance Analysis of Piezo-Ceramic Elements in Soils," *Geotechnical Geological Engineering*, 2010.
- [43] M. Biot, "Theory of Propagation of Elastic Waves in a Fluid-Saturated Porous Solid. I. Low-Frequency Range," *The Journal of the Acoustical Society of America*, vol. 28, no. 2, pp. 168-178, 1956.
- [44] M. Biot, "Theory of Propagation of Elastic Waves in a Fluid-Saturated Porous Solid. II. Higher Frequency Range," *The Journal of the Acoustical Society of America*, vol. 28, no. 2, pp. 179-191, 1956.
- [45] X. Gu, J. Yang, M. Huang and G. Gao, "Bender element tests in dry and saturated sand: Signal interpretation and result comparison," *Soils and Foundations*, vol. 55, no. 5, pp. 951-962, 2015.

- [46] I. D. Moldovan and A. G. Correia, "Fixed point automatic interpretation of bender-based Go measurements," *Computers and Geotechnics*, vol. 89, pp. 128-142, 2017.
- [47] R. Andrus and K. Stokoe II, "Liquefaction Resistance of Soils from Shear-Wave Velocity," *Journal of Geotechnical and Geoenvironmental Engineering*, vol. 126, no. 11, 2000.
- [48] D. Lo Presti, M. Jamiolkowski, O. Pallara, A. Cavallaro and S. Pedroni, "Shear modulus and damping of soils," *Geotechnique*, vol. 47, no. 3, pp. 603-617, 1997.
- [49] Z. Cheng and E. C. Leong, "Determination of damping ratios for soils using bender element tests," *Soil Dynamics and Earthquake Engineering*, vol. 111, pp. 8-13, 2018.
- [50] T.-M. Oh, E.-S. Bang, G.-C. Cho and E.-S. Park, "Estimation of undrained shear strength for saturated clay using shear wave velocity," *Marine Geosources & Geotechnology*, 2016.
- [51] M. Karray, G. Lefebvre, Y. Ethier and A. Bigras, "Influence of particle size on the correlation between shear wave velocity and cone tip resistance," *Canadian Geotechnical Journal*, vol. 48, pp. 599-615, 2011.
- [52] M. N. Hussien and M. Karray, "Shear wave velocity as a geotechnical parameter: an overview," *Canadian Geotechnical Journal*, vol. 53, pp. 252-272, 2015.
- [53] S. Gadeikis, K. Dundulis, G. Zarzojus, S. Gadeikyte, D. Urbaitis, D. Gribulis, S. Sliupa and L. Gabrielaitis, "Correlation between shear wave velocity and cone resistance of Quaternary glacial clayey soils defined by seismic cone penetration test," *Journal of Vibroengineering*, 2013.

- [54] M. Long and S. Donohue, "Characterization of Norwegian marine clays with combined shear wave velocity and piezocone cone penetration test (CPTU) data," *Canadian Geotechnical Journal*, 2010.
- [55] I. Dyka, O. E. Srokosz and M. Bujko, "Influence of grain size distribution on dynamic shear modulus of sands," *Open Engineering*, vol. 7, no. 1, pp. 317-329, 2017.
- [56] J. Santamarina, K. Klein and M. Fam, *Soils and Waves: Particulate Materials Behaviour, Characterization and Process Monitoring*, James Wiley, 2001.
- [57] M. Vecetic and R. Dobry, "Effect of soil plasticity on cyclic response," *Journal of Geotechnical Engineering*, vol. 117, no. 1, pp. 89-107, 1991.
- [58] "ASTM D422-63(2007)e2, Standard Test Method for Particle-Size Analysis of Soils," ASTM International, [Online]. Available: www.astm.org. [Accessed 1 January 2018].
- [59] "ASTM D4318-17e1, Standard Test Methods for Liquid Limit, Plastic Limit, and Plasticity Index of Soils," ASTM International, [Online]. Available: www.astm.org. [Accessed 1 January 2018].
- [60] "ASTM D854-14 - Standard Test Methods for Specific Gravity of Soil Solids by Water Pycnometer," ASTM International, [Online]. Available: www.astm.org. [Accessed 1 January 2018].
- [61] "ASTM D2487-17, Standard Practice for Classification of Soils for Engineering Purposes (Unified Soil Classification System)," ASTM International, [Online]. Available: www.astm.org. [Accessed 1 January 2018].

- [62] "ASTM G57-06(2012), Standard Test Method for Field Measurement of Soil Resistivity Using the Wenner Four-Electrode Method," ASTM International, [Online]. Available: www.astm.org. [Accessed 1 January 2018].
- [63] "ASTM D1143-07 - Standard Test Methods for Deep Foundations Under Static Axial Compressive Load," ASTM International, 2007. [Online]. Available: www.astm.org. [Accessed 1 January 2018].
- [64] "ASTM D4648-16 - Standard Test Methods for Laboratory Miniature Vane Shear Test for Saturated Fine-Grained Clayey Soil," ASTM International, [Online]. Available: www.astm.org. [Accessed 1 January 2018].
- [65] V. Dombrovski, QuickField 5.9, Svendborg, Denmark: Tera Analysis Ltd., 2018.

4.2. Appendix

4.2.1. Arduino Code

POWER SUPPLY ON

```
#include <SPI.h>

byte address = 0x00;

int CS= 10;

void setup()
{
  pinMode (CS, OUTPUT);
  SPI.begin();
}

void loop()
{
  for (int i = 119; i <= 120; i++)
  {
    digitalPotWrite(i);
    delay(100);
  }
  delay(100000);
  for (int i = 120; i >= 119; i--)
  {
    digitalPotWrite(i);
    delay(10);
  }
}

int digitalPotWrite(int value)
{
  digitalWrite(CS, LOW);
  SPI.transfer(address);
  SPI.transfer(value);
  digitalWrite(CS, HIGH);
```

POWER SUPPLY OFF

```
#include <SPI.h>

byte address = 0x00;

int CS= 10;

void setup()
{
  pinMode (CS, OUTPUT);
  SPI.begin();
}

void loop()
{
  for (int i = 0; i <= 1; i++)
  {
    digitalPotWrite(i);
    delay(100000);
  }
  delay(10);
  for (int i = 1; i >= 0; i--)
  {
    digitalPotWrite(i);
    delay(10);
  }
}

int digitalPotWrite(int value)
{
  digitalWrite(CS, LOW);
  SPI.transfer(address);
  SPI.transfer(value);
  digitalWrite(CS, HIGH);
```

4.2.2. MATLAB Code

4.2.2.1. DT9867 DAQ

```
clc;
clear all;
close all;

%% 1. THIS MATLAB FUNCTION OUTPUTS AND COLLECTS DATA FROM BENDER
ELEMENTS AND LOGS DATA TO A .txt FILE. IT ALSO PLOTS FIGURES OF
THE DATA, SAVES THOSE FIGURES AND SAVES CC AND P-P ANALYSIS DATA
TO .CSV

%1 SETUP
d = daq.getDevices; %CHECK DEVICES

(Type daq.getDevices for device specific information)

fOut=210000; %Digital to Analog Output Rate, Hz
fIn=105000; %Analog to Digital Input Rate, Hz
Ts=1/fIn; %Time Step, Seconds
B=0; %Arbitrary B Variable
    TrialFolder='Trial2'; %Folder to Save Data In

%SET OUTPUT BROADCAST FREQUENCYS IN 20x1 ARRAY ('1' is a place
holder for sweep)
fSig=[50; 100; 150; 250; 300; 350; 400; 500; 600;...
700; 800; 900; 1000; 1250; 1500; 2000; 2500;...
3000; 4000; 5000 ;1];

Vout= 1.6; %OUTPUT VOLTAGE (Check Amplifier Input Sensitivity)
SENSORS =4; % SET NUMBER OF ACTIVE INPUTS
Row='T'; %SELECT WHICH ROW IS IN USE (Top OR Bottom)
if Row=='T'
R=7;
elseif Row=='B'
R=0;
end

T = 2; % SET DATA AQUITION WINDOW TIME
TOTALCUT=5000; % TOTALCUT specifies number of samples kept
% THIS WILL AFFECT THE DATA SIZE AND FFT RESOLUTION
%(RESOLUTION=fIn/TOTALCUT)

%%CREATE SWEEP OUTPUT DATA BEFORE STARTING LOOP
t=0:(1/fOut):1; %Divide 0-1 second into fOut steps
OutDataSweep=chirp(t,50,1,5000,'linear',-90)*Vout;
%START SWEEP AT 50Hz, STOP SWEEP AT 5kHz

%%2 RUN DATA ACQUISITION IN A LOOP
```

```

%USE FOR LOOP TO HAVE PROGRAM RUN CONSECUTIVELY THROUGH
FREQUENCIES ONE THROUGH TWENTY, THEN LASTLY SWEEP
%CREATE SIGNAL, OUTPUT SIGNAL, AQUIRE DATA, PROCESS DATA, SAVE
PROCESSED DATA AND SAVE PLOT
for f=1:21

pause(2); % PAUSE TWO SECONDS FOR DATA ACQUISITION TO FINISH

if (1<=f) && (f<=20) %RUN BLOCK FOR PULSED SIGNALS ONLY
CUTS=round(fIn/4/fSig(f,1)); %SPECIFY WHERE CUT STARTS
CUTF=round(TOTALCUT-fIn/fSig(f,1)); %WHERE START ENDS
CUTT=CUTS+CUTF;

%CREATE SINE PULSE (SINGLE WAVE) FOR OUTPUT
SinePulse = linspace(0,2*pi,(fOut/fSig(f,1)))';
SinePulse = sin(SinePulse)*Vout;
OutDataPulse = (cat(1,SinePulse, ...
                    zeros(fOut - length(SinePulse),1)));
end

%% START NEW OUTPUT SESSION
AO = daq.createSession('dt');

% SELECT OUTPUTS AND CONFIGURE RATE
Out1= addAnalogOutputChannel...
      (AO, 'DT9857-16(00)',0, 'Voltage');
% SET OUTPUT DATA RATE
AO.Rate = fOut;

%% START NEW INPUT SESSION
AI = daq.createSession('dt');

% SELECT INPUT CHANNELS (use i+R for top row on DT9857)
%INPUT COUPLING AND SET INPUT RANGES
IN=cell(1,SENSORS);

for i=1:SENSORS
IN{i} = addAnalogInputChannel...
      (AI, 'DT9857-16(00)', (i+R), 'Voltage');
      end
for i=2:SENSORS
IN{i}.Coupling = 'AC';
IN{i}.Range= [-1 1];
end

% SET INPUT AQUISTITION RATE
AI.Rate= fIn;

%% CHECK SESSION PROPERTIES
AO
AI

```

```

% CONFIGURE OUTPUT DATA AND LISTENER

if (1<=f) && (f<=20)
Output=OutDataPulse;
else
Output=OutDataSweep';
end

queueOutputData(AO,Output); % QUEUE OUTPUT DATA TO SESSION

% CREATE LISTENER FOR OUTPUT TERMINAL TO OUTPUT DATA
DataRequired = addlistener...
    (AO, 'DataRequired',@(src,event)...
    src.queueOutputData(Output));
% SET DATA OUTPUT AS CONTINUOUS OR NOT
AO.IsContinuous = false;

% CREATE LOG.BIN, AND LISTENER TO LOG DATA
fid1 = fopen('log.bin','w+');
% CREATE INPUT LISTENER
DataAvailable = addlistener...
    (AI,'DataAvailable',@(src, event)...
    logData(src, event, fid1));
AI.IsContinuous = true; % SET AQUISITION AS CONTINUOUS OR NOT

% Start INPUT then OUTPUT
AI.startBackground;
AO.startBackground;
% Allow Aquisition to run for 'T' time.
if f==21
pause(1)
else
pause(T);
end

AO.stop; %% STOP INPUT
AI.stop; %% STOP OUTPUT

fclose(fid1); % CLOSE INPUT FILE

%% OPEN DATA, TRANSFER TO ARRAY 'Data'
fid2 = fopen('log.bin','r+');
[Data,~] = fread(fid2, [(SENSORS+1),inf], 'double');
fclose(fid2);

% Row structure of Array 'Data':
%1:
%2:          Amplitude          Input          Time
%3:          Amplitude          Input          2

```

```

%N:                Amplitude                Input                'N-1'
%...

%% SAVE CUT DATA AS ShortData, PROCESS SIGNAL (FILTERS,
DETRENDING) AND SAVE AS .txt
% Create Array ShortData first to quicken execution
ShortData= zeros(SENSORS+1, (CUTF+CUTS));

% Determine Max of Output and Log that sample #
[PKOut,PKTimeOut]=max(Data(2,:));
if (1<=f) && (f<=20) %RUN BLOCK FOR PULSED SIGNALS ONLY

for i=1:SENSORS+1 %SAVE SEGMENT OF CUTF+CUTS OF ARRAY Data AS
ShortData
ShortData(i,1:(CUTF+CUTS+1))= Data(i,PKTimeOut-
CUTS:PKTimeOut+CUTF);
end
Folder=sprintf('%iHz',fSig(f,1));
else
ShortData=Data;
Folder=sprintf('Sweep');
end

%ASSIGN APPROPRIATE FILE NAME AND FOLDER AND SAVE ORIGINAL DATA
File= sprintf('%iHz-test_%s',fSig(f,1),datestr(now,'mm-dd-
yyyy-HH-MM'));
FileName= strcat(File, '.txt');
FullName=fullfile([pwd '\ ' TrialFolder '\ ' Folder '\ '
FileName]);

dlmwrite(FullName,ShortData,'delimiter','\t','precision','%.9f
')

%FILTER DATA
d1 = designfilt('bandstopiir','FilterOrder',2, ...
'HalfPowerFrequency1',105,'HalfPowerFrequency2',135, ...
'DesignMethod','butter','SampleRate',fIn);
t=(0:size(ShortData,2)-1)/fIn;

for i=3:5 %APPLY FILTER TO SHORTDATA
ShortData(i,:)=filtfilt(d1,ShortData(i,:));
end

%DETREND ShortData BY FITING TO LOW ORDER POLYLINE
N=8;
Order=3;
FrameLength=61;

if 1<=f && f<=20
for i=3:5
p=[];

```

```

        f_y=[];
        [p(i,:),S,mu(:,i)]=polyfit((1:size(ShortData,2)),ShortData
(i,:),N);
        f_y(i,:)=
polyval(p(i,:), (1:size(ShortData,2)), [], mu(:, i));
        ShortData(i,:)=ShortData(i,:) - f_y(i,:);
        ShortData(i,:)=sgolayfilt(ShortData(i,:),Order,FrameLength
);
    end
end

%Axis Text Height
ATH=8;

%% PREPARE AND PRINT PLOTS TO FIGURES

%Setup Title Headers
xLlim=0;
if f==21
    Title=sprintf('Bender Element Test Sine Sweep 50Hz to 5kHz');
    xHlim=5000;
else
    Hz=fSig(f,1);
    Title=sprintf('Bender      Element      Test      Sine      Pulse
%iHz',fSig(f,1));
    xHlim=(fSig(f,1))+1000;
end

if f==21
    ShortData=[];
    for i=3:5
        p=[];
        f_y=[];

        [p(i,:),S,mu(:,i)]=polyfit((1:size(Data,2)),Data(i,:),N)
;
        f_y(i,:)= polyval(p(i,:), (1:size(Data,2)), [], mu(:, i));
        ShortData(i,:)=Data(i,:) - f_y(i,:);
        CUTT=(size(Data,2));
    end
    ShortData(1,:)=Data(1,:);
    ShortData(2,:)=Data(2,:);
end

% Create Figure and Plot 12 Subplots in Figure

%% Plot Row 1
figure(1);
h=suptitle(Title);

```

```

set(h, 'Interpreter', 'latex', 'FontSize', 14, 'FontName', 'Times
New Roman');

subplot(4,3,1)
plot(ShortData(1,:), ShortData(2,:));

title('Output Signal', 'Interpreter', 'latex', 'FontSize', 10,
'FontName', 'Times New Roman');

ylabel('Signal Amplitude, Volts',
'Interpreter', 'latex', 'FontSize', 10, 'FontName', 'Times
New Roman')

set(gca, 'fontsize', ATH)

subplot(4,3,2)
[freq, fabs] = fftplot(Ts, ShortData((2),1:(CUTT)));
plot(freq, fabs);

title('Output FFT', 'Interpreter', 'latex', 'FontSize', 10,
'FontName', 'Times New Roman');

ylabel('Frequency Amplitude, Volts',
'Interpreter', 'latex', 'FontSize', 10, 'FontName', 'Times
New Roman')

xlim([xLlim xHlim]);
set(gca, 'fontsize', ATH)

subplot(4,3,3)
[acor, lag] = xcorr(ShortData(2,:), ShortData(2,:), 'coeff');
plot(lag, acor);
lag=lag/fIn;
title('Output XCorrelation to
Self', 'Interpreter', 'latex', 'FontSize', 10, 'FontName',
'Times New Roman');

ylabel('Normalized XCorrelation',
'Interpreter', 'latex', 'FontSize', 10, 'FontName', 'Times
New Roman')

[~, I] = max(abs(acor));
DeltaCCT= lag(I);
set(gca, 'fontsize', ATH)

%% PLOT ROW 2
subplot(4,3,4)
plot(ShortData(1,:), ShortData(3,:));
if 1<=f && f<=20

```

```

findpeaks(ShortData(3,:),ShortData(1,:), 'MinPeakHeight',0.
00001, 'MinPeakDistance',0.001, 'NPeaks',2, 'SortStr', 'descen
d');
end
set(gca, 'fontsize',ATH)
title('Barrel 1 Signal', 'Interpreter', 'latex', 'FontSize',
10, 'FontName', 'Times New Roman');

subplot(4,3,5)
[freq, fabs] = fftplot(Ts, ShortData(3,1:(CUTT)));
plot(freq, fabs);

title('Barrel 1 FFT', 'Interpreter', 'latex', 'FontSize', 10,
'FontName', 'Times New Roman');
xlim([xLlim 1500]);

set(gca, 'fontsize',ATH)

subplot(4,3,6)
[acor,lag] = xcorr(ShortData(3,:),ShortData(2,:), 'coeff');
lag=lag/fIn;
plot(lag,acor);

findpeaks(acor,lag, 'MinPeakHeight',0.1, 'MinPeakDistance',0
.001, 'NPeaks',1, 'SortStr', 'descend');

title('Barrel 1 XCorrelation to
Output', 'Interpreter', 'latex', 'FontSize', 10, 'FontName',
'Times New Roman');
[CC1,I] = max(abs(acor));
DeltaCCT1= 0.24/lag(I);
set(gca, 'fontsize',ATH)

%% PLOT LINE 3
subplot(4,3,7)
plot(ShortData(1,:), ShortData(4,:));
if 1<=f && f<=20

findpeaks(ShortData(4,:),ShortData(1,:), 'MinPeakHeight',0.
00001, 'MinPeakDistance',0.001, 'NPeaks',2, 'SortStr', 'descen
d');
end
set(gca, 'fontsize',ATH)
title('Barrel 2 Signal', 'Interpreter', 'latex', 'FontSize',
10, 'FontName', 'Times New Roman');

subplot(4,3,8)
[freq, fabs] = fftplot(Ts, ShortData(4,1:(CUTT)));
plot(freq, fabs);

```

```

title('Barrel 2 FFT','Interpreter','latex','FontSize', 10,
'FontName', 'Times New Roman');
xlim([xLlim 1500]);
set(gca,'fontsize',ATH)

subplot(4,3,9)
[acor,lag] = xcorr(ShortData(4,:),ShortData(2,),'coeff');
lag=lag/fIn;

findpeaks(acor,lag,'MinPeakHeight',0.1,'MinPeakDistance',0
.001,'NPeaks',1,'SortStr','descend');

title('Barrel 2 XCorrelation to
Output','Interpreter','latex','FontSize', 10, 'FontName',
'Times New Roman');

[CC2,I] = max(abs(acor));
DeltaCCT2=0.24/ lag(I);
set(gca,'fontsize',ATH)

%% PLOT LINE 4
subplot(4,3,10)
plot(ShortData(1,:), ShortData(5,:));
if 1<=f && f<=20

findpeaks(ShortData(5,:),ShortData(1,),'MinPeakHeight',0.
00001,'MinPeakDistance',0.001,'NPeaks',2,'SortStr','descen
d');
end
title('Barrel 3 Signal','Interpreter','latex','FontSize',
10, 'FontName', 'Times New Roman');
xlabel('Time, Seconds', 'Interpreter','latex','FontSize',
10, 'FontName', 'Times New Roman');
set(gca,'fontsize',ATH)

subplot(4,3,11)
[freq, fabs] = fftplot(Ts, ShortData(5,1:(CUTT)));
plot(freq, fabs);
title('Barrel 3 FFT','Interpreter','latex','FontSize', 10,
'FontName', 'Times New Roman');
xlabel('Frequency, Hz', 'Interpreter','latex','FontSize',
10, 'FontName', 'Times New Roman');
xlim([xLlim 1500]);

set(gca,'fontsize',ATH)

subplot(4,3,12)
[acor,lag] = xcorr(ShortData(5,:),ShortData(2,),'coeff');
lag=lag/fIn;

```

```

findpeaks(acor,lag,'MinPeakHeight',0.1,'MinPeakDistance',0
.001,'NPeaks',1,'SortStr','descend');

title('Barrel          3          XCorrelation          to
Output','Interpreter','latex','FontSize',10,'FontName',
'Times New Roman');

xlabel('Time          Lag,          Seconds',
'Interpreter','latex','FontSize',10,'FontName','Times
New Roman')

[CC3,I] = max(abs(acor));
DeltaCCT3= 0.24/lag(I);
set(gca,'fontsize',ATH)

%% SAVE FIGURE 1
FileName= strcat(File, '.fig');
FullName=fullfile([pwd '\ TrialFolder '\ Folder '\
FileName]);
savefig(gcf,FullName,'compact');
%jpeg printing function...
FileName=strcat(File, '.jpeg');
FullName=fullfile([pwd '\ Trial '\ Folder '\ FileName]);
print (gcf, '-djpeg',FullName);

%% CALCULATE TIME TO PEAK AND SAVE BOTH P-P AND CC DATA TO EXCEL
CSV FILE

if (1<=f) && (f<=20)

[V1,T1]=findpeaks(ShortData(2,:),ShortData(1,),'MinPeakDistan
ce',0.001,'NPeaks',2,'SortStr','descend');

[V2,T2]=findpeaks(ShortData(3,:),ShortData(1,),'MinPeakDistan
ce',0.001,'NPeaks',2,'SortStr','descend');

[V3,T3]=findpeaks(ShortData(4,:),ShortData(1,),'MinPeakDistan
ce',0.001,'NPeaks',2,'SortStr','descend');

[V4,T4]=findpeaks(ShortData(5,:),ShortData(1,),'MinPeakDistan
ce',0.001,'NPeaks',2,'SortStr','descend');

%0.24 m distance between elements
DeltaT1=0.24/(T2(1,1)-(T1(1,1)));
DeltaT2=0.24/(T3(1,1)-(T1(1,1)));
DeltaT3=0.24/(T4(1,1)-(T1(1,1)));
end
D=now;
T=rem(now,1);

```

```

CCVelocity= [D T CC1 DeltaCCT1 DeltaT1 CC2 DeltaCCT2 DeltaT2 CC3
DeltaCCT3 DeltaT3];

File= sprintf('%iHz',fSig(f,1));
FileName= strcat(File, '-Velocity.csv');
CCName=fullfile([pwd '\\' TrialFolder '\\' Folder '\\' FileName]);
dlmwrite(CCName,CCVelocity,'-append','precision',16);

%% PLOT Velocity Values
Array=csvread(FileName);

%FILTER OUT VALUES BELOW ZERO AND OVER 200 (NOISE)
VB1=Array(:,4:7);
VB1(VB1<0)=0;
VB1(VB1>200)=0;
VB1max=max(VB1');
if f==1
VB1Ult=VB1max
end
if VB1max>=VB1Ult
VB1Ult=VB1max
end

LoBFit1=polyfit((1:size(VB1max,1))',VB1max,4);
LoBFit1=polyval(LoBFit1,1:size(VB1max,1));

figure (2)
subplot(3,1,1)

plot(VB1(:,1),'r+');
hold on
plot(VB1(:,2),'b+');
plot(VB1(:,3),'g+');
plot(VB1(:,4),'c+');
plot (LoBFit1,'k-');

ylabel('          Barrel          1          Shear          Wave          Velocity',
'Interpreter','latex','FontSize', 10, 'FontName', 'Times New
Roman');

legend(' xCorrelation Peak',' Tallest Signal Peak',' 2nd Tallest
Signal Peak',' 3rd Tallest Signal Peak')

hold off

VB2=Array(:,9:12);
VB2(VB2<0)=0;
VB2(VB2>200)=0;
VB2max=max(VB2');
if f==1
VB2Ult=VB2max

```

```

end
if VB2max>=VB2Ult
VB2Ult=VB2max
end

LoBFit2=polyfit((1:size(VB2max,1))',VB2max,4);
LoBFit2=polyval(LoBFit2,1:size(VB2max,1));

subplot(3,1,2)

plot(VB2(:,1),'r+');
hold on
plot(VB2(:,2),'b+');
plot(VB2(:,3),'g+');
plot(VB2(:,4),'c+');
plot(LoBFit2,'k-');

ylabel('          Barrel          2          Shear          Wave          Velocity',
'Interpreter','latex','FontSize', 10, 'FontName', 'Times New
Roman');

legend(' xCorrelation Peak',' Tallest Signal Peak',' 2nd Tallest
Signal Peak',' 3rd Tallest Signal Peak')

hold off

VB3=Array(:,14:17);
VB3(VB3<0)=0;
VB3(VB3>200)=0;
VB3max=max(VB3)';
if f==1
VB3Ult=VB3max
end
if VB3max>=VB3Ult
VB3Ult=VB3max
end
LoBFit3=polyfit((1:size(VB3max,1))',VB3max,4);
LoBFit3=polyval(LoBFit3,1:size(VB3max,1));

subplot(3,1,3)
plot(VB3(:,1),'r+');
hold on
plot(VB3(:,2),'b+');
plot(VB3(:,3),'g+');
plot(VB3(:,4),'c+');
plot(LoBFit3,'k-');

ylabel('          Barrel          3          Shear          Wave          Velocity',
'Interpreter','latex','FontSize', 10, 'FontName', 'Times New
Roman');

```

```

xlabel(' Time (Hours)', 'Interpreter','latex','FontSize', 10,
'FontName', 'Times New Roman');

legend(' xCorrelation Peak',' Tallest Signal Peak',' 2nd Tallest
Signal Peak',' 3rd Tallest Signal Peak')

hold off

%% SAVE FIGURE 2
FileName= strcat(File, '_Velocity_VS_Time.fig');

FullName=fullfile([pwd  '\\' TrialFolder  '\\' Folder  '\\'
FileName]);
savefig(gcf,FullName,'compact');
%jpeg printing function...
FileName=strcat(File, '.jpeg');
FullName=fullfile([pwd  '\\' TrialFolder  '\\' Folder  '\\'
FileName]);
print (gcf, '-djpeg',FullName);

end
%% SAVE MAX SPEED VALUE
MAXVELALL = [D T VB1Ult VB2Ult VB3Ult]
dlmwrite('MaxVelocityAll',MAXVELALL, '-append', 'precision',16);
UltVel=csvread('MaxVelocityAll.csv')

figure (3);
plot(UltVel(:,3), 'r+');
hold on
plot(UltVel(:,4), 'b+');
plot(UltVel(:,5), 'g+');

legend(' Barrel 1 Ultimate Velocity',' Barrel 2 Ultimate
Velocity',' Barrel 3 Ultimate Velocity')

xlabel(' Shear Wave Velocity',
'Interpreter','latex','FontSize', 10, 'FontName', 'Times New
Roman');
hold off

%% SAVE FIGURE
File='Ultimate_Velocity'
FileName= strcat(File, '.fig');
FullName=fullfile([pwd  '\\' TrialFolder  '\\' FileName]);
savefig(gcf,FullName,'compact');
%jpeg printing function...
FileName=strcat(File, '.jpeg');
FullName=fullfile([pwd  '\\' TrialFolder  '\\' FileName]);
print (gcf, '-djpeg',FullName);
%% CLEANUP
delete (AO);

```

```

delete (AI);
delete (DataRequired);
delete (DataAvailable);

```

4.2.2.2. Timer

```

VATimer = timer;
% 'Quick'Variable Specifying Timer Period in seconds
%5 min interval
Time=300;

% Set Arbitrary Name for Timer
set(VATimer, 'Name', 'VATimer')
% Set How Timer Resets and When TimerFcn Triggers
% Options are singleShot, fixedSpacing, fixedDelay, fixedRate
set(VATimer, 'ExecutionMode', 'fixedRate');
% Set delay between calling TimerFcn
set(VATimer, 'Period', Time);
% Set Number of Times to Run before stop
%Run for 7 Days, 5 minute interval
set(VATimer, 'TasksToExecute', 2016);

set(VATimer, 'BusyMode', 'queue');

set(VATimer, 'TimerFcn', 'VoltAmp')
start(VATimer);
% delete (VATimer);

```

4.2.2.3. Timer Function

```

function VoltAmp(~)
[V]=Sequencer;
[A]=Sequencer2;
D=datenum(now);
T=rem(now,1);

VA=[D T V A];

dlmwrite('VoltAndAmpValues.csv',VA, '-append', 'precision', 16)
end

```

4.2.2.4. Voltmeter Call Function

```

function [Voltage] = MeterCheck(VRange, VResolution,)
Meter_Top = visa('agilent',
'USB0::0x0957::0x0618::TW47340039::0::INSTR');
Meter_Top.InputBufferSize = 8388608;
Meter_Top.ByteOrder = 'littleEndian';
fopen(Meter_Top);

VRange=100;
VResolution=0.001;

```

```

Voltage          =          str2double(query(Meter_Top,
sprintf(':MEASure:VOLTage:DC? %g,%g', VRange, VResolution)));
Voltage = str2double(query(Meter_Top, ':FETCh?'));
Voltage

fclose(Meter_Top);
delete(Meter_Top);
clear Meter_Top;

end

```

4.2.2.5. Ammeter Call Function

```

function [Amperage]=MeterCheck2 (ARange, AResolution)
Meter_Bottom          =          visa('agilent',
'USB0::0x0957::0x0618::TW47340036::0::INSTR');
Meter_Bottom.InputBufferSize = 8388608;
Meter_Bottom.ByteOrder = 'littleEndian';
fopen(Meter_Bottom);

ARange=10;
AResolution=0.001;
Amperage          =          str2double(query(Meter_Bottom,
sprintf(':MEASure:CURRent:DC? %g, %g' ARange,AResolution)));
Amperage = str2double(query(Meter_Bottom, ':FETCh?'));
Amperage
fclose(Meter_Bottom);
delete(Meter_Bottom);
clear Meter_Bottom;
end

```